Multi-Scale Conformal Maps and Free Boundary Problems

by

Stuart Thomas Kent

A Dissertation Submitted to the Faculty of the

Graduate Interdisciplinary Program in Applied Mathematics

In Partial Fulfillment of the Requirements
For the Degree of

Doctor of Philosophy

In the Graduate College

The University of Arizona

2 0 1 3

THE UNIVERSITY OF ARIZONA
GRADUATE COLLEGE

As members of the Dissertation Committee, we certify that we have read the dissertation prepared by Stuart Thomas Kent entitled Multi-Scale Conformal Maps and Free Boundary Problems and recommend that it be accepted as fulfilling the dissertation requirement for the Degree of Doctor of Philosophy.

_____ Date: June 28th, 2013
Shankar Venkataramani

_____ Date: June 28th, 2013
Karl Glasner

_____ Date: June 28th, 2013
Kenneth McLaughlin

_____ Date: June 28th, 2013
Kevin Lin

Final approval and acceptance of this dissertation is contingent upon the candidate's submission of the final copies of the dissertation to the Graduate College.

I hereby certify that I have read this dissertation prepared under my direction and recommend that it be accepted as fulfilling the dissertation requirement.

_____ Date: June 28th, 2013
Shankar Venkataramani

Statement by Author

This dissertation has been submitted in partial fulfillment of requirements for an advanced degree at The University of Arizona and is deposited in the University Library to be made available to borrowers under rules of the Library.

Brief quotations from this dissertation are allowable without special permission, provided that accurate acknowledgment of source is made. Requests for permission for extended quotation from or reproduction of this manuscript in whole or in part may be granted by the copyright holder.

Signed: Stuart Thomas Kent

Acknowledgments

I would like to thank Dr. Michael Tabor, head of the Interdisciplinary Program in Applied Mathematics at the University of Arizona, for his work in creating and maintaining such a well rounded and well funded program, as well as Stacey LaBorde and Anne Keyl for their help in navigating University administration.

I would especially like to thank Dr. Shankar Venkataramani for his guidance and for sharing many insights during our time working together. His inquisitiveness and intuition remain truly astounding to me still.

Dedication

This thesis is dedicated to my parents, Janet and Andrew, for all the time they spent to ensure that I received a consistently excellent education, and for their continued support of my academic endeavors many miles from home; and to my wife, Rebecca, who always provides advice when requested, encouragement when required, and love unconditionally.

Table of Contents

TABLE OF CONTENTS—*Continued*

List of Figures

List of Figures—*Continued*

List of Figures—*Continued*

List of Tables

Abstract

In this dissertation, we study free boundary problems that describe equilibrium configurations of electromechanical systems consisting of a conducting elastic sheet deflected by an external charge distribution. Such systems are non-local in nature - the electrostatic pressure experienced by any individual point on the sheet depends on the entire deflection profile (as a result of the requirement that the deflected sheet must remain an equipotential). The magnitude of the electrostatic pressure varies quadratically with the magnitude of the local electric field. Similar non-local free boundary problems arise in two-layer fluid systems forced by withdrawal flows, but the normal viscous stress experienced by the fluid-fluid interface instead varies linearly with the local velocity gradients.

The analysis presented focuses on two configurations in particular: the electromechanical system described above, forced by a point charge, and an artificially modified version of the same electromechanical system in which the induced electrostatic pressure varies linearly with the local electric field and the forcing is provided by an electric dipole. This second model is constructed as a crude approximation of the two-layer fluid flow forced by a point sink, and is primarily used to explore the influence of the forcing exponent on the bifurcation structure and solution types of the associated system.

Our main contribution is the development of new techniques for the analysis and efficient numerical computation of large-deflection profiles for the true electromechanical system. The induced charge on such profiles accumulates near the interface tip, so that the geometry there is primarily determined by a balance between elastic and electrostatic forces. Away from the tip, the electrostatic pressure is low and the interface relaxes under the influences of gravity and elasticity only. Such interfaces exhibit features on widely disparate length scales. We exploit this separation of the interface into two regions dominated by different force balances to create a separate representation of each region (in appropriately rescaled coordinates), and then match the two representations together while ensuring that the relationship between local induced stress and global interface geometry is respected. This is achieved by combining tools and results from complex analysis and the method of matched asymptotic expansions.

Chapter 1
Introduction

1.1 Electromechanical Systems

All electromechanical systems (EMS) consist of a conducting elastic interface manipulated by a forcing charge distribution. The external charge induces a charge distribution on the elastic sheet, and the resulting electric force draws the conducting sheet towards the forcing. EMS are examples of free boundary problems, systems of partial differential equations (PDEs) posed in a domain $\mathcal{D}$, a portion of whose boundary is unknown in advance. One equation in the system of PDEs typically relates properties of the free portion of the boundary $\partial\mathcal{D}$ of $\mathcal{D}$ to the dependent variables defined on the interior of $\mathcal{D}$, and solutions of the system must therefore determine both the values of the dependent variables and the geometry of $\partial\mathcal{D}$ simultaneously.

EMS are also examples of non-local free boundary problems. The instantaneous electric force experienced by any individual point on the conducting interface depends on the local electric potential ϕ, but this potential is governed by Laplace's equation $\nabla^2\phi = 0$ with Dirichlet boundary condition $\phi = \text{const.}$ on the entire free boundary $\partial\mathcal{D}$. This coupling between local electric force and *global* interface geometry is a significant hurdle to overcome when seeking system configurations that are simultaneously in electric and mechanical equilibrium.

Microelectromechanical systems (MEMS) are electromechanical devices whose physical dimensions are on the order of micrometres (10^{-6}m). They include miniaturized sensors, actuators, and capacitors, whose applications include the monitoring of patient blood pressure from within IV lines and acting as triggers for airbag deployment in vehicles. A typical model of a two-dimensional MEMS is shown in the schematic Fig. 1.1. A rigid plate is held at a fixed height $y = l$ above a conducting

elastic sheet that is pinned at $(L/2, 0)$ and $(-L/2, 0)$. A potential difference applied between the plate and the conducting sheet causes the sheet to deflect towards the plate in the manner shown.

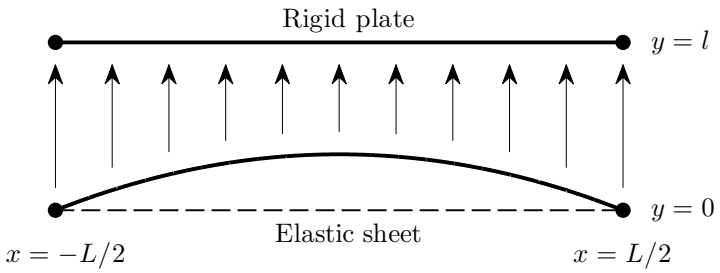

FIGURE 1.1. The canonical MEMS model. A rigid plate is held fixed above an elastic conducting sheet. An applied potential difference deflects the elastic sheet towards the plate.

Early experiments with EMS were performed by (Taylor, 1968) using a symmetric configuration in which a potential difference was applied between two elastic membranes (soap films). Taylor noted the existence of a 'pull-in' instability that occurred as the applied potential difference was increased - beyond a critical forcing strength, no stable equilibrium deflections could be supported by the system. The same instability is observed in modern MEMS, and a full understanding of the transition location and deflection profile properties is extremely important in guaranteeing the efficacy of real devices. For forcing strengths exceeding the critical forcing strength, the elastic interface is drawn toward the rigid plate until touchdown occurs and the equations governing the MEMS model cease to apply.

The canonical MEMS model describing equilibrium deflection profiles was developed in the early 2000s (Bernstein et al., 2000; Pelesko & Triolo, 2000; Pelesko, 2001, 2002; Pelesko & Chen, 2003); many variations and more history can be found in (Chuang et al., 2010). This model exploits the small dimensions and aspect ratio l/L of real devices to neglect the influence of gravity, employ the linear model of elasticity,

and approximate the electric field between the plate and sheet by a linear function of y for each fixed x. This decouples the local electric force from the global interface geometry, and allows the system of PDEs governing $h(x)$ and $\phi(x, y)$ to be reduced to a single ordinary differential equation (ODE) for $h(x)$. The resulting system contains a saddle node bifurcation in the q-$h(0)$ bifurcation diagram, consistent with the existence of a maximally-deflected stable equilibrium deflection.

Recent studies of MEMS have focused on removing the assumptions described above and analyzing the change in the system bifurcation structure. The inclusion of both geometrically nonlinear elasticity and stabilization due to gravity (or an applied pressure gradient) have yielded only small improvements in the agreement between theoretical predictions of the pull-in voltage and experimental data (Siddique et al., 2011; Brubaker & Pelesko, 2011; Brubaker et al., 2013). We outline our own work on these extensions in Chapter 2, and refer readers to (Brubaker & Pelesko, 2012; Brubaker & Lindsay, 2013) for more extensive analysis along these lines. The authors of (Brubaker et al., 2013) speculate that the approximations made concerning the electric field explain most of the discrepancy. This thesis contains analysis of an EMS in which the full electric field, and therefore, the dependence of local electric force on global deflection geometry, is retained (Chapters 3, 4 and 5). The applied forcing is significantly more condensed than in typical MEMS, so direct comparisons with experimental results are difficult. However, we hope that the methodology presented herein may be adapted to model more standard MEMS configurations in the future.

1.2 Selective Withdrawal Flows

Interplay between interface geometry and induced stresses also characterizes two-layer fluid flows in which forcing is applied to a very viscous fluid layer. The forcing can either be localized (withdrawal of fluid through a narrow tube suspended above the undeflected fluid-fluid interface) or provided by an extensional flow typically generated

by immersing rotating cylinders in the viscous layer. Interest in problems of this type is driven by a wide range of applications, including freshwater extraction from island lenses (Hocking & Forbes, 2004), analysis of the composition and stratification of magma in volcanoes (Lister, 1989), and particle coating (Cohen et al., 2001; Younes et al., 2008).

An analog of the pull-in instability (and corresponding saddle-node bifurcation) in EMS is observed in selective withdrawal flows (Berkenbusch et al., 2008). As the strength of the applied forcing is increased, the steady state interface transitions from a 'hump' (Fig. 1.2(a)) to a 'spout' (Fig. 1.2(b)) in which the interface is broken and a slender spout of the lower fluid is drawn up by the viscous upper fluid. The spout regime is considered analogous to touchdown in EMS. Both the onset of the instability (water extraction, oil extraction) and the stable steady-state interface geometries formed as the critical forcing strength is approached from below (particle coating) are important to understand for applications. Many studies have focused on ascertaining exactly how sharp such interfaces can become before transition occurs (Jeong & Moffatt, 1992; Eggers, 2001; Zhang, 2004; du Pont & Eggers, 2006; Jeong, 2007; Berkenbusch et al., 2008; Blanchette & Zhang, 2009; Eggers & du Pont, 2009; Eggers & Courrech du Pont, 2010; Blanchette & Zhang, 2010). Much of this work builds upon theory surrounding the sharp tips developed by small drops placed in straining flows (Taylor, 1934; Richardson, 1968; Buckmaster, 1972; Richardson, 1973; Youngren & Acrivos, 1976; Acrivos & Lo, 1978; Hinch, 1980; Moffatt, 1992), with a broad overview of both dynamic and parametric singularities in such problems given by (Rallison, 1984).

1.3 Governing Equation Structures and Universality

Consider the generic cross-section of Fig. 1.3. When modeling a fluid system, we assume that the upper material is a very viscous Newtonian fluid and the lower

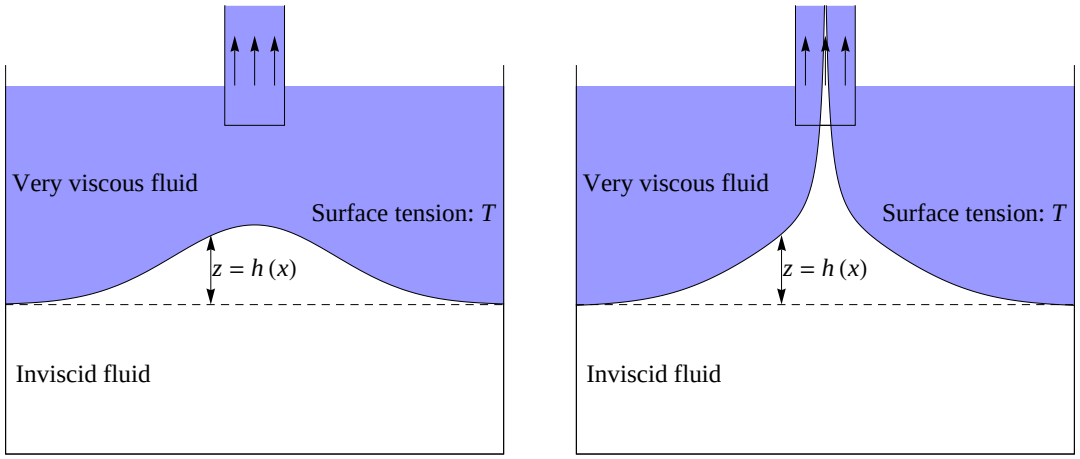

FIGURE 1.2. Schematic representations of the two steady-state regimes supported by selective withdrawal systems. (a) For low withdrawal rates, the interface forms a 'hump'. (b) For higher withdrawal rates, the interface is broken and a 'spout' forms.

material is an inviscid fluid. When modeling an EMS, we assume that the interface $y = h(x)$ represents a conducting elastic sheet. These choices allow us to write the equations governing equilibrium configurations of each system as boundary integral equations of the form

$$F(x, h(x)) + \int_{\mathbb{R}} [h(x') - \kappa(x')]^{1/r} K(x; x'; h) dA_{x'} = 0, \tag{1.3.1}$$

where κ is the curvature of the sheet, and F, K and r are defined for each system type in Table 1.1. This equation must hold for all $x \in \mathbb{R}$ for two-dimensional systems. More details on this formulation are provided in §3.1.

The parameter r describes the relationship between local field gradients and local induced stress in each system type. We conjecture that the dependence of local induced stresses on global interface geometry (and hence, the value of r) is of primary importance in systems of these types, and that free boundary problems of the form (1.3.1) may be divided into universality classes in which equilibrium solution behav-

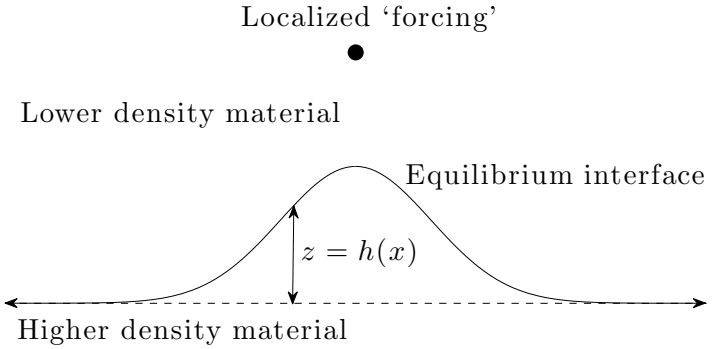

FIGURE 1.3. Generic model cross-section. For fluid systems, we assume that the upper material is a very viscous fluid and the lower material an inviscid fluid. For EMS, we take the interface to be a conducting elastic sheet.

	Fluid	Electromechanical
$F(x, h(x))$	Normal component of forcing flow at $(x, h(x))$.	Potential at $(x, h(x))$ due to forcing charge.
$K(x; x'; h)$	Normal flow at $(x, h(x))$ due to a Stokeslet of unit strength at $(x', h(x'))$.	Potential at $(x, h(x))$ due to a charge of unit strength at $(x', h(x'))$.
r	1.	2.

TABLE 1.1. Variable definitions and values for fluid and electromechanical models associated with Fig. 1.3.

ior near phase transitions depends primarily on the forcing exponent r and forcing type. A full investigation of this conjecture remains future work. Within this thesis, we consider two main system configurations inspired by the relationship between electrostatic and fluid systems:

A: a 'true' EMS corresponding to the model of Fig. 1.3 with $r = 2$, forced by a point charge of strength q located at $(0, l)$; and

B: a 'modified' EMS corresponding to the model of Fig. 1.3 but with $r = 1$, forced by a dipole of moment q located at $(0, l)$ and aligned with the y-axis.

The forcing type used in configuration B is selected based on perturbation analyses

of the modified EMS and fluid systems presented in §3.2.

1.4 Dissertation Structure

In Chapter 2, we derive the canonical MEMS model for two-dimensional systems to highlight the influences of the small scale and aspect ratio of such devices. In separate subsections, we consider the effects of vary the forcing exponent r and reintroducing gravitational and geometrically nonlinear elastic forces to the MEMS model, and derive estimates of the critical forcing strength in each of the modified systems. The pull-in instability is shown to persist in all modified system. However, the unstable solution branch in the system featuring geometrically nonlinear elastic forces splits into two separated pieces in certain subsets of parameter space, a phenomenon now known to be caused by a tendency for deflection profiles to become multi-valued (Brubaker & Lindsay, 2013).

In Chapter 3, we consider full models of configurations A and B as defined above. The governing equations are reduced to dimensionless form, with each system now controlled by two dimensionless parameters q (the strength of the applied forcing relative to elastic tension) and l (the height of the applied forcing relative to the capillary length scale). The small-forcing/small-deflection profiles of these systems are calculated, and we note that the fluid flow model forced by a point sink produces small-deflection profiles that agree with those of the EMS in configuration B. We then recast the governing equations in complex variables and appeal to properties of conformal maps (in particular, the fact that conformal maps transform harmonic functions to harmonic functions) to redefine the problem on the unit disk $\mathbb{D} \subset \mathbb{C}$ and facilitate numerical approximation of true deflection profiles in configuration A the extension to configuration B is trivial). We solve the recast problem using a collocation method to sample the residual pressure along candidate solutions using the Fast Fourier Transform (FFT), and identifying the best approximation from within

a give class of solutions by minimizing this sampled residual pressure. Solutions and system structures calculated using this method are presented and discussed. A pull-in instability exists for all forcing heights l in case A, and for all forcing heights below some threshold value of l in case B. Limitations of the method used become apparent when attempting to calculate interface deflection profiles with $l - h(0) \ll 1$. In this regime, the deflection profile features structures on widely disparate length scales (a highly curved tip, and slow relaxation towards the undeflected state) so that the problem becomes very stiff. Existing numerical methods for solving FBPs require the use of non-uniform grids in such situations - and pay the price in efficiency losses as a result. However, inspection of the force balances governing different portions of calculable deflection profiles motivates our use of matched asymptotic expansions in the next chapter.

In Chapter 4, we develop a numerical scheme for efficiently computing large-deflection profiles of the true electrostatic problem. This method does not rely on adaptively refining the grid used to represent profiles near high-curvature regions. Instead, separate conformal maps are computed to represent each portion of the full interface deflection profile in which a different force balance dominates, and these maps are then combined by requiring that both the deflection profiles and the parametrizations of the conformal maps defining each profile agree in an intermediate region. This latter condition is critical to ensuring that the solutions produced continue to (at least approximately) respect the relationship between the global profile geometry and the local induced electrostatic pressure. Proceeding without this condition by matching profiles alone would be completely physically unjustified.

In Chapter 5, we study the inverse problem for the true and modified electrostatic problems. The goal here is to calculate the forcing distribution that supports an interface shape defined as the image of the unit circle $\partial\mathbb{D}$ under a conformal map $\mathbb{F}$. The main results are presented for the modified electrostatic problem without gravity. In this case, it is possible to categorize which maps produce deflections that may be

supported by finitely many charges located within $\mathbb{D}$. This work is relevant to MEMS design and may be used to construct forcing configurations that produce deflection profiles with desired properties and forcing responses.

In Chapter 6, we highlight extensions of the work presented within this thesis and give brief descriptions of the tools and techniques to be applied in each case.

In Appendix A, sample code is given for the original and matching-based collocation methods to demonstrate their implementations.

Chapter 2
MEMS Models

We begin our study of EMS and their relationship to selective withdrawal systems by building upon existing studies of MEMS (Fig. 1.1). The now-standard mathematical model describing equilibrium interface deflections in MEMS was developed and analyzed in the early 2000s (Bernstein et al., 2000; Pelesko & Triolo, 2000; Pelesko, 2001, 2002; Pelesko & Chen, 2003) and relies on three simplifying assumptions:

(i) the device dimensions are small: l, $L \ll 1$;

(ii) the conducting sheet is thin, so that linear models of elasticity may be applied;

(iii) the device aspect ratio is small: $\varepsilon \equiv l/L \ll 1$.

Assumptions (i) and (ii) together allow the influence of gravity to be ignored. Assumption (iii) leads to two simplifications: the restorative elastic term can be represented using the linearized interface curvature, and the electric field between the charged plate and the deflected sheet may be approximated by a linear function of y alone. Crucially, this final simplification decouples the local electrostatic pressure from the global deflection geometry. This removes the most significant obstacle to the calculation of equilibrium interface deflection profiles, but also severely limits the applicability of MEMS model analyses to more general EMS (including those on larger physical scales or with localized forcing).

In this chapter, we derive the standard MEMS equation in two dimensions and present elementary analysis to introduce relevant analytic tools. We then consider extensions of the MEMS equation following two distinct themes:

(i) in §2.4.1, we vary the exponent that describes the relationship between the electric field near the deflected interface and the electrostatic pressure induced

there. In particular, we are interested in comparing the bifurcation structures generated by quadratic and linear relationships (the former represents the standard MEMS model (and is similar to configuration A, with more distributed forcing), the latter is an artificial alteration that mimics the linear relationship between velocity gradients and viscous stresses near fluid-fluid interfaces (similar to configuration B, again with more distributed forcing)).

(ii) in §2.4.2 and §2.4.3, we separately study the effects of incorporating gravity and geometrically nonlinear elasticity into the basic MEMS equation. Since the conclusion of the work presented in this thesis, more extensive analyses of similarly-modified systems have been conducted (Siddique et al., 2011; Brubaker & Pelesko, 2011, 2012; Brubaker et al., 2013; Brubaker & Lindsay, 2013). We include our results here for completeness. It is worth noting that the simultaneous inclusion of corrections for both gravity and geometrically nonlinear elasticity has so far failed to satisfactorily explain discrepancies between experimentally-observed pull-in voltages and predictions based on the standard MEMS model (Siddique et al., 2011; Brubaker et al., 2013). The need for a treatment of EMS that preserves the dependence of local electrostatic pressure on global deflection geometry (as ours does) is therefore clear.

We find that the main structural features of the standard MEMS model are preserved by all of the modifications listed. All systems continue to exhibit a saddle-node bifurcation structure, implying the existence of a critical forcing strength q_{crit} beyond which pull-in occurs. The most notable difference occurs in the case with geometrically nonlinear elasticity incorporated. Here, we find that portions of the unstable solution branch disappear in some subsets of parameter space. This phenomenon is now known to be caused by a tendency for equilibrium interface deflections of this system to contain folds, a regime not compatible with the MEMS equation as written in (2.1.5) - (Brubaker & Lindsay, 2013) provides a thorough analysis of this behavior

and a modified form of (2.1.5) that properly accommodates multi-valued solutions.

2.1 Governing Equations

Consider again the canonical MEMS configuration of Fig. 1.1. We denote the deflection of the elastic sheet by $y = h(x)$, the elastic tension per unit length in the sheet by T, and the potential difference applied between the sheet and the rigid plate by V. The electric potential $\phi(x, y)$ defined on $\{(x, y) : y \in [h(x), 1],\ x \in [-1/2, 1/2]\}$ depends both on V and (*a priori*) on the geometry of the entire *deflection profile* $\{h(x) : x \in [-1/2, 1/2]\}$. As there is no charge inside the region $\{(x, y) : y \in (h(x), 1),\ x \in (-1/2, 1/2)\}$, ϕ satisfies Laplace's equation there. The system is considered infinite and uniform in the z-direction.

For a given value of V, equilibrium deflections (if they exist) are determined by a balance between elastic and electrostatic forces at every point on the interface. In §§2.1.1-2.1.2, we compute general representations of each forcing typing in terms of h and ϕ before applying the simplifying assumptions required to obtain the equation (2.1.5) that describes equilibrium deflection profiles.

2.1.1 Elastic Force

Consider the interface segment shown in Fig. 2.1, where $\delta \ll 1$. We calculate the net downward force $F(x)$ per unit length due to elastic tension experienced by the bold portion between $x - \delta$ and $x + \delta$ (whose arclength is $2\delta + \mathcal{O}(\delta^2)$):

$$\begin{aligned} F(x) &= \frac{T}{2\delta + \mathcal{O}(\delta^2)} \left(\frac{-h_x(x+\delta)}{\sqrt{1 + h_x^2(x+\delta)}} + \frac{h_x(x-\delta)}{\sqrt{1 + h_x^2(x-\delta)}} \right), \\ &= -T \frac{d}{dx} \left(\frac{h_x(x)}{\sqrt{1 + h_x^2(x)}} \right) + \mathcal{O}(\delta), \\ &= \frac{-T h_{xx}(x)}{(1 + h_x^2(x))^{3/2}} + \mathcal{O}(\delta), \\ &= -T\kappa(x) + \mathcal{O}(\delta), \end{aligned} \tag{2.1.1}$$

where $\kappa(x)$ is the signed interface curvature at $(x, h(x))$.

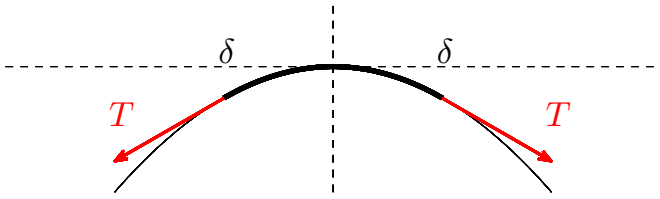

FIGURE 2.1. A schematic diagram showing the forces on a small segment of a curved interface due to uniform elastic tension T. The net force is always directed towards the center of curvature (i.e. along the normal direction).

2.1.2 Electrostatic Force

The electrostatic pressure experienced by the deflected interface can be computed in terms of ϕ by combining the following facts:

- The electric field $E = -\nabla\phi$ above the conducting interface is perpendicular to the interface at its surface (otherwise the induced charge would redistribute).
- The electric field below the interface is identically zero (the conducting sheet effectively shields the region $y < h(x)$ from the charged plate).
- Gauss' law applied to a small pillbox straddling the interface at $(x, h(x))$ gives $E^+(x) = E(x) \cdot n = \sigma(x)/\varepsilon_0$ just above the interface, where n denotes the upward unit normal, σ is the density of the charge induced on the sheet, and ε_0 is the permittivity of free space.
- The normal force $F(x)$ per unit area experienced by the surface of a conductor is given by $F(x) = \sigma(x)E^+(x)/2$.

The upward (normal) electrostatic force may therefore be neatly represented in terms of ϕ:

$$F(x) = \frac{\varepsilon_0}{2}(\nabla\phi \cdot n)^2. \tag{2.1.2}$$

2.1.3 Simplifications for MEMS

Before calculating the simplified nondimensional equations governing small aspect ratio MEMS, we write out the full dimensional force-balance equation (equating (2.1.1) and (2.1.2)) and associated governing equations and boundary conditions for ϕ and $h(x)$. These are

$$\frac{-Th_{xx}(x)}{(1+h_x^2(x))^{3/2}} = \frac{\varepsilon_0}{2}\frac{\left(-h_x(x)\phi_x(x,h)+\phi_y(x,h)\right)^2}{1+h_x^2(x)} \text{ for } x\in[-L/2,L/2], \quad (2.1.3)$$
$$h(-L/2) = 0,$$
$$h(L/2) = 0,$$
$$\phi_{xx}(x,y)+\phi_{yy}(x,y) = 0 \text{ in } \{h(x)<y<l : x\in[-L/2,L/2]\},$$
$$\phi'(x',l) = V \text{ for } x\in[-L/2,L/2],$$
$$\phi(x,h(x)) = 0 \text{ for } x\in[-L/2,L/2].$$

Rescaling $x = Lx'$, $y = ly'$, $h = lh'$, $\phi = V\phi'$ yields the equivalent dimensionless equations

$$\frac{-h'_{x'x'}(x')}{(1+\mathcal{O}(\varepsilon^2))^{3/2}} = \frac{q\left(\phi'_{y'}(x',h')+\mathcal{O}(\varepsilon^2)\right)^2}{1+\mathcal{O}(\varepsilon^2)} \text{ for } x'\in[-1/2,1/2],$$
$$h'(-1/2) = 0,$$
$$h'(1/2) = 0,$$
$$\phi'_{y'y'}(x',y')+\mathcal{O}(\varepsilon^2) = 0 \text{ in } \{h'(x')<y'<1 : x'\in[-1/2,1/2]\},$$
$$\phi'(x',1) = 1 \text{ for } x'\in[-1/2,1/2],$$
$$\phi'(x',h'(x')) = 0 \text{ for } x'\in[-1/2,1/2],$$

where $q = \varepsilon_0 V^2L^2/Tl^3 > 0$ is a dimensionless parameter that measures the strength of the electrostatic forcing relative to the restorative elastic tension. To leading order in ε, the nondimensional sheet deflection therefore satisfies

$$-h_{xx}(x) = q\phi_y^2(x,h) \text{ for } x\in[-1/2,1/2], \quad (2.1.4a)$$

$$h(-1/2) = 0, \tag{2.1.4b}$$

$$h(1/2) = 0, \tag{2.1.4c}$$

$$\phi_{yy}(x, y) = 0 \text{ in } \{h(x) < y < 1 : x \in [-1/2, 1/2]\}, \tag{2.1.4d}$$

$$\phi(x, 1) = 1 \text{ for } x \in [-1/2, 1/2], \tag{2.1.4e}$$

$$\phi(x, h(x)) = 0 \text{ for } x \in [-1/2, 1/2]. \tag{2.1.4f}$$

where primes have been dropped for convenience. (2.1.4d-2.1.4f) have exact solution $\phi(x, y) = (y - h(x))/(1 - h(x))$, so that (2.1.4a) reduces to

$$-h_{xx}(x) = \frac{q}{(1 - h(x))^2} \text{ for } x \in [-1/2, 1/2] \tag{2.1.5}$$

with boundary conditions (2.1.4b-2.1.4c). This equation is the two-dimensional version of the canonical MEMS equation as derived in (Bernstein et al., 2000), with the geometry inverted to better align our variables and plots with those of later chapters.

2.2 Solutions

(2.1.5) can be integrated once exactly, yielding

$$\frac{1}{2}h_x^2 + V[h] = E, \tag{2.2.1}$$

where $E > 0$ is the total energy in the system and the potential V is given by $V[h] = q/(1 - h)$. An example phase portrait for this system (with $q = 1$) is plotted in Fig. 2.2. We define a time-of-flight functional by

$$\tau[h] \equiv 2 \int_{V^{-1}(E)}^{0} \frac{dh}{h_x}. \tag{2.2.2}$$

The boundary conditions (2.1.4b-2.1.4c) are seen to be equivalent to the single condition $\tau = -1$. Appealing to the symmetric nature of the original model, substituting for V, and making several changes of variables yields the following compact equation implicitly defining E in terms of q:

$$2\sqrt{2}q \int_0^{\sqrt{E-q}} \frac{ds}{(E - s^2)^2} = 1. \tag{2.2.3}$$

Once E is calculated for a given q, the entire deflection profile may be obtained through direct numerical integration of (2.2.1). The maximal deflection $h(0)$ is explicitly given by $h(0) = 1 - q/E$. This reformulation allows easier calculation of bifurcation diagrams featuring multiple solution branches for a given forcing strength q, especially since we anticipate the existence of unstable solutions.

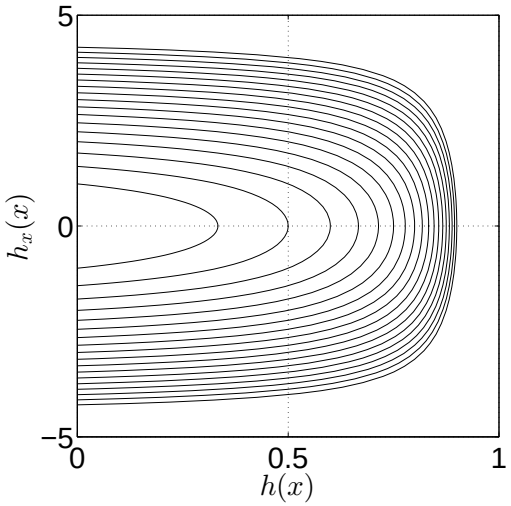

FIGURE 2.2. An example phase portrait for (2.1.5) with $q = 1$, varying $E > 0$. (2.2.3) determines which orbits correspond to profiles $h(x)$ satisfying the boundary conditions (2.1.4b-2.1.4c).

Figure 2.3(a) shows deflection profiles for a range of q-values computed using the time-of-flight formulation above. The bold curve corresponds to the maximally-deflected stable profile. The associated q-$h(0)$ bifurcation diagram (Fig. 2.3(b)) shows a saddle-node bifurcation which corresponds physically to the existence of a critical forcing strength q_{crit} beyond which pull-in occurs (i.e. no equilibrium configurations exist). The portion of the bifurcation diagram lying below the bold profile is stable: a small positive/negative perturbation in $h(0)$ for fixed q yields an underforced/overforced boundary that will relax towards the original configuration. Conversely, the portion of the bifurcation diagram lying above the bold profile is unstable: a small positive/negative perturbation in $h(0)$ for fixed q yields an overforced/underforced

boundary whose deviation from the original configuration will grow.

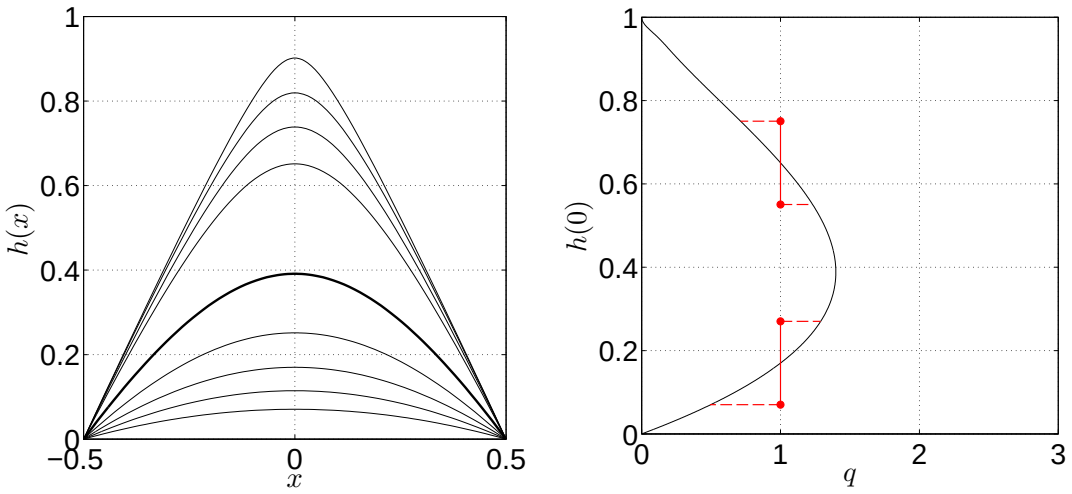

FIGURE 2.3. (a) Equilibrium deflection profiles $h(x)$ satisfying (2.1.5) for $q \in \{0.25, 0.5, 0.75, 1, 1.4\}$. The bold curve corresponds to the maximally-deflected stable profile, with $q = q_{crit} \approx 1.4$. (b) The bifurcation structure of (2.1.5), plotting tip deflection $h(0)$ against forcing strength q (black curve). For all $q < q_{crit}$, two distinct equilibrium deflections exist. For $q > q_{crit}$, no equilibrium deflections exist. Small positive/negative perturbations in $h(0)$ for fixed q (red lines) on the lower branch produce underforced/overforced interfaces that relax back to the original deflection profile. The situation is reversed for the upper branch.

Note that pull-in occurs when both $h(0)$ and the interface tip curvature are $\mathcal{O}(1)$. As $h(0) \to 1$, the interface tip sharpens and approaches a corner. The leading order deflection profile for $1 - h(0) \ll 1$ is the piecewise-linear function $h_0(x) = 1 - 2|x|$.

2.3 Estimating the Pull-In Forcing Strength

The form of the MEMS equation (2.1.5) enables us to calculate an upper bound on the critical forcing strength q_{crit} by appealing to the maximum principle for elliptic ODEs (Evans, 1998). The proof reduces to standard calculus arguments when dealing

with a single ODE. First, note that

$$h_{xx}(x) = \frac{-q}{(1-h(x))^2} \leq \frac{-27qh(x)}{4} \tag{2.3.1}$$

everywhere in $[-1/2, 1/2]$.[1] This bound is illustrated in Fig. 2.4.

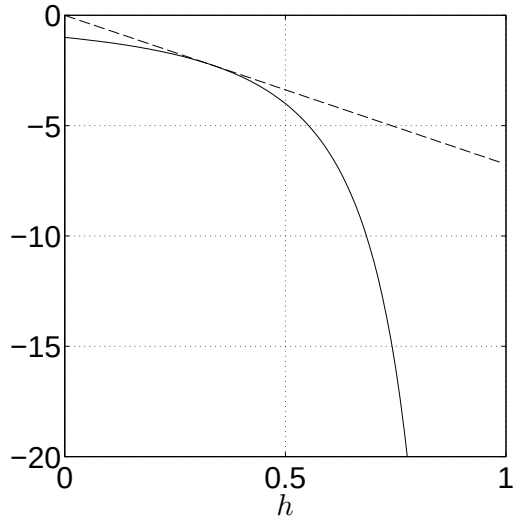

FIGURE 2.4. The forcing term $-q/(1-h)^2$ (solid curve) and the linear upper bound $-27qh/4$ (dashed curve) from (2.3.1) plotted for $h \in [0, 1)$.

We define a function $H(x)$ on $[-1/2, 1/2]$ by

$$H_{xx}(x) = \frac{-27qH(x)}{4}, \tag{2.3.2}$$

where H is subject to the same boundary conditions as h: $H(\pm 1/2) = 0$. The difference function $D(x) = (h - H)(x)$ is then superharmonic ($D_{xx}(x) \leq 0$) on $[-1/2, 1/2]$, and satisfies $D(\pm 1/2) = 0$.

Lemma 2.3.1. Let h and H be classical solutions of (2.1.5) and (2.3.2) respectively, with $h(\pm 1/2) = 0 = H(\pm 1/2)$. Then $D = (h - H) \geq 0$ on $[-1/2, 1/2]$.

[1] The linear function passing through the origin produces the tightest bound on q_{crit} with this method.

Proof of Lemma 2.3.1. Assume $\exists\ x_1 \in [-1/2, 1/2]$ such that $D(x_1) < 0$. By the Mean Value Theorem, $\exists\ x_2 \in (-1/2, x_1)$ such that $D_x(x_2) < 0$, and similarly $\exists\ x_3 \in (x_1, 1/2)$ such that $D_x(x_3) > 0$. A second application of the Mean Value Theorem implies $\exists\ x_4 \in (x_2, x_3)$ such that $D_{xx}(x_4) > 0$. But D is known to be superharmonic, so this is a contradiction. □

We have shown that $H(x)$ is a lower bound for $h(x)$ on $[-1/2, 1/2]$.

The eigenvalue problem $f_{xx}(x)+\lambda f(x) = 0$ with boundary conditions $f(\pm 1/2) = 0$ has non-trivial solutions just when $\cos(\sqrt{\lambda}/2) = 0$. The smallest positive value of λ that produces non-trivial solutions is $\lambda = \pi^2$, which corresponds to a family of eigenfunctions of arbitrarily large magnitudes (any multiple of the eigenfunction is a solution of the equation). Since H satisfies exactly this equation with $\lambda \equiv 27q/4$, we deduce that pull-in occurs for a forcing strength q_{crit} no larger than $4\pi^2/27$. This upper bound overestimates the true value of q_{crit} by 4-5%.

2.4 Extensions of the Standard MEMS Model

2.4.1 Varying the Electrostatic Pressure Exponent

In the introduction to this thesis, parallels were drawn between electrostatic and fluid free boundary problems. While these problems are similarly structured, we noted that the relationships between local field gradients and induced stresses experienced by the interfaces are different in each case. The dependence is linear in fluid problems, and quadratic in true electrostatic systems. Motivated by this distinction, in this subsection we extend results for the canonical MEMS equation (2.1.5) to the more general class of equations

$$-h_{xx}(x) = \frac{q}{(1-h(x))^r} \text{ for } x \in [-1/2, 1/2],\ r \in [1, 2]. \tag{2.4.1}$$

We will refer to this family as the rMEMS equations. In particular, we look to compare the cases $r = 2$ (canonical MEMS) and $r = 1$ (mimicking the linear relationship

between field gradients and induced stress of fluid free boundary problems) to identify any changes in bifurcation structure.

Multiplying by h_x and integrating once yields (2.2.1) again, with V now given by

$$V[h] = \begin{cases} -q\log(1-h), & r = 1, \\ \dfrac{q}{(r-1)(1-h)^{r-1}}, & r \in (1,2]. \end{cases} \tag{2.4.2}$$

We may define a time-of-flight functional and combine it with the unaltered boundary conditions to produce a compact relationship between q and $E > 0$ exactly as before, since V is invertible for all $r \in [1,2]$. Figure 2.5 shows the resulting bifurcation diagrams for (left to right) $r \in \{2, 1.5, 1\}$. The essential features of the system are qualitatively unaltered by the change in exponent - all diagrams feature a saddle-node bifurcation, indicating the existence of a pull-in instability at a critical forcing strength q_{crit}. The maximum principle still applies for all values of $r \in [1,2]$, and produces the upper bounds

$$q_r^* \leq \frac{r^r \pi^2}{(r+1)^{r+1}}. \tag{2.4.3}$$

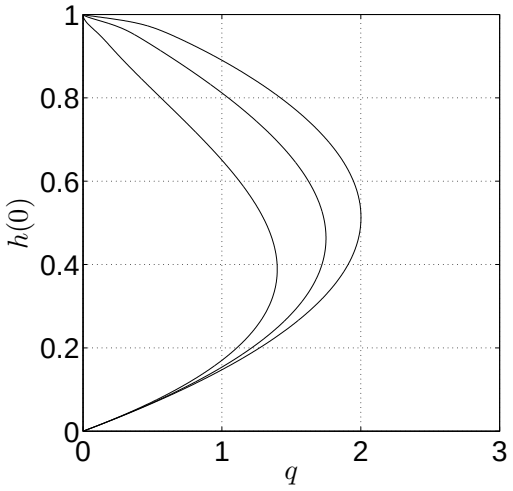

FIGURE 2.5. Bifurcation structures of (2.4.1), for (left to right) $r = 2$, 1.5, 1. All diagrams contain a saddle-node bifurcation, indicating the existence of a pull-in instability.

2.4.2 Introducing Gravity

In this subsection, we consider the effects of including a stabilizing 'gravity' term to the rMEMS equations. The new governing equation considered has the form

$$-h_{xx}(x) + mh(x) = \frac{q}{(1-h(x))^r} \text{ for } x \in [-1/2, 1/2], \tag{2.4.4}$$

where $m > 0$ is a dimensionless parameter measuring the strength of the gravitational forces relative to the elastic forces. Physically, this modification is equivalent to assuming that the material above the deflected interface is of lower density than the material below the deflected interface. We will give analytic formulae for all $r \in [1, 2]$, but restrict plots to $r = 2$ for simplicity whenever this case is representative of all those considered.

Integrating (2.4.4) yields (2.2.1) once more, with V now given by

$$V[h] = \begin{cases} -q\log(1-h) - \dfrac{1}{2}mh^2, & r = 1, \\ \dfrac{q}{(r-1)(1-h)^{r-1}} - \dfrac{1}{2}mh^2, & r \in (1, 2] \end{cases} \tag{2.4.5}$$

and

$$E \geq \begin{cases} 0, & r = 1, \\ \dfrac{q}{r-1}, & r \in (1, 2]. \end{cases}$$

Recall that the time-of-flight formulation of §2.2 relied on the time-of-flight function defined by (2.2.2). However, the potentials (2.4.5) are everywhere invertible just when $q < r^r m/(r+1)^{r+1}$, so the lower integration limit in (2.2.2) is not necessarily well-defined. To determine which solution of $V[h] = E$ should be used to define τ when multiple solutions exist, we inspect the phase portraits of the rMEMS equations.

Figure 2.6 is the analog of Fig. 2.2 with $r = 2$, $q = 1$, and $m = 10$. The energy level $E = 1.05$ (dashed curves) produces two distinct orbits, but only one intersects the line $h = 0$. The other is not able to satisfy all of the boundary conditions of the problem and must be discarded. In the time-of-flight formulation, we therefore choose

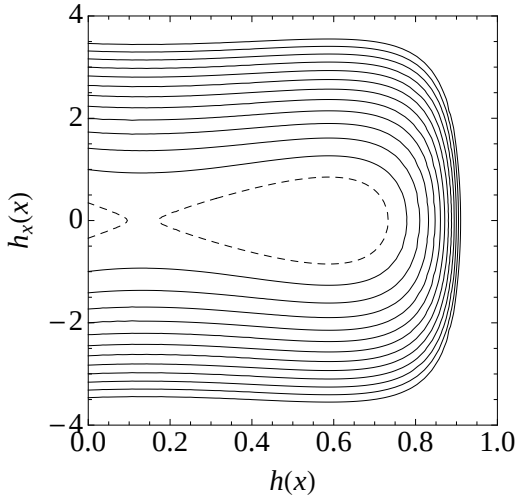

FIGURE 2.6. The phase portrait corresponding to equation (2.4.4) for $r = 2$, $q = 1$, and $m = 10$, a case where V is known not to be invertible. Various energies $E > 1$ are plotted. For E close to 1, orbits separate into two distinct pieces (dashed curves). The closed orbit cannot satisfy the boundary conditions and should be ignored when calculating $V^{-1}(E)$ in the time-of-flight functional τ. When V is invertible, this issue does not arise and the standard definition of τ applies.

to interpret $V^{-1}(E)$ as representing the smallest-magnitude solution of the equation $V[h(0)] = E$.

Following this convention produces the family of bifurcation diagrams shown in Fig. 2.7(a). The presence of the stabilizing gravity force increases the critical forcing strength q_{crit}. However, the geometry of maximally-deflected stable solutions is influenced very little by the presence of the gravitational term, even when m is large (Fig. 2.7(b)).

Finally, we note that the existing bound (2.4.3) on q_{crit} may be trivially extended to incorporate gravity:

$$q_r^* \leq \frac{r^r(\pi^2 + m)}{(r+1)^{r+1}}.$$

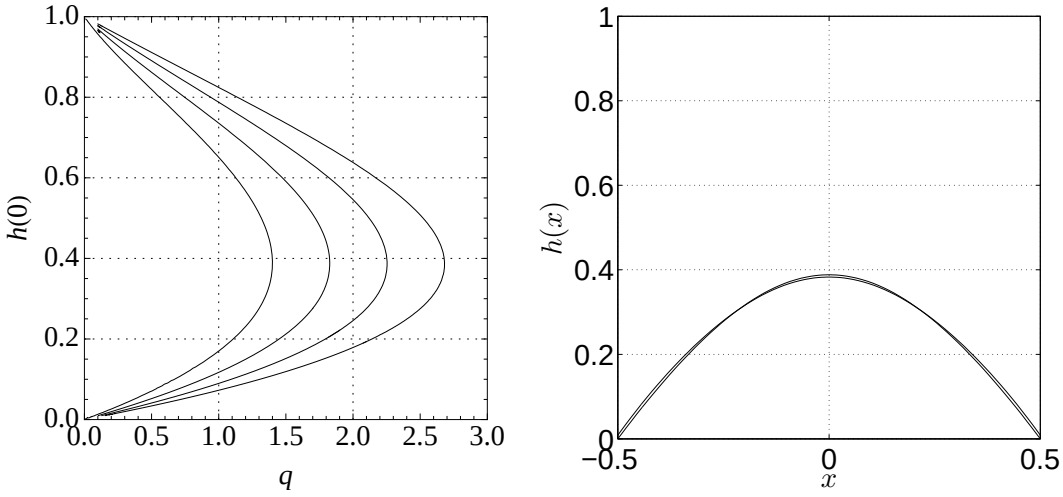

FIGURE 2.7. (a). Bifurcation structures of (2.4.4), with $r = 2$ and (left to right) $m = 0$, 3, 6, 9. All diagrams indicate pull-in behavior, and maximally deflected stable solutions with comparable heights. (b) Maximally-deflected stable solutions of (2.4.4) for $m = 0$ and $m = 9$. While the forcing strengths required to support each solution are very different, the deflection profiles appear almost identical.

2.4.3 Re-introducing Geometrically Nonlinear Elasticity

When deriving the standard MEMS equation in §2.1, the interfacial curvature was approximated by $h_{xx}(x)$ (based on the small aspect ratio approximation). In this subsection we reintroduce the full expression for the interface curvature and, as in §2.4.2, investigate how the bifurcation structure and solutions of this extended system compare to those of the canonical MEMS model. We retain the leading order approximation to the induced electrostatic pressure (even though the neglected terms in the electrostatic pressure are of the same order of magnitude as the reintroduced contributions to curvature) and are careful to bear in mind that we have not completely freed ourselves of the small aspect ratio approximation.

The governing equations considered in this subsection are

$$\frac{-h_{xx}(x)}{(1+kh_x^2(x))^{3/2}} = \frac{q}{(1-h(x))^r} \text{ for } x \in [-1/2, 1/2], \tag{2.4.6}$$

where $k > 0$ is a dimensionless parameter related to the aspect ratio of the system ($k = \varepsilon^2$). Integrating once yields

$$-\frac{1}{k\sqrt{1+kh_x^2(x)}} + V[h] = E, \tag{2.4.7}$$

where V is still given by (2.4.2) and is therefore always invertible. Solving (2.4.7) for h_x gives[2]

$$h_x(x) = \pm\sqrt{\frac{(E - V[h])^{-2} - k^2}{k^3}},$$

so that the analog of the time-of-flight formulation (2.2.3) is now

$$2k^{3/2}\int_{V^{-1}(E+1/k)}^{0} \frac{dh}{\sqrt{(E-V[h])^{-2}-k^2}} = -1.$$

Before seeking solutions, we again inspect the phase portraits associated with (2.4.7) to determine any inadmissible orbits. Figure 2.8 is the analog of Fig. 2.2 with $r = 2$, $q = 1$, and $k = 1$. We find that values of E too large produce orbits that never intersect the line $h = 0$, leading to the bounds

$$\begin{cases} -\dfrac{1}{k} \le E \le 0, & r = 1, \\ \dfrac{q}{r-1} - \dfrac{1}{k} \le E \le \dfrac{q}{r-1}, & r \in (1,2] \end{cases}$$

on admissible energies E.

The bounds on E translate to the following bounds on the interface tip deflection $h(0)$:

$$0 < h(0) \le 1 - e^{-1/(kq)} \text{ for } r = 1, \tag{2.4.8}$$

$$0 < h(0) \le 1 - \left(\frac{kq}{kq + (r-1)}\right)^{1/(r-1)} \text{ for } r \in (1,2]. \tag{2.4.9}$$

Figure 2.9(a) shows computed bifurcation diagrams for $r = 2$ and various values of $k \in [0, 2]$. The saddle-node structure is preserved in all plotted cases. Unsurprisingly, weakening the elastic forces in the system causes pull-in to occur for a lower

[2]In doing so, we square both sides of (2.4.7) and therefore expect to have introduced extraneous solutions that must be identified and removed from later diagrams.

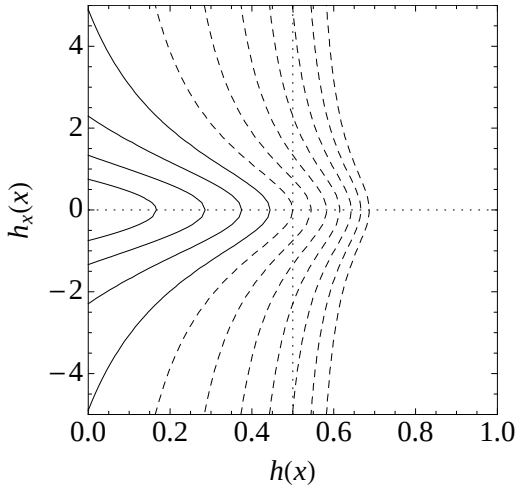

FIGURE 2.8. Phase portrait corresponding to equation (2.4.7) with $r = 2$, $q = 1$, and $k = 1$. Various energies $E > 0$ are plotted. When $E > 1$, the dashed orbits never intersect $h = 0$ and the corresponding solutions are incapable of satisfying the boundary conditions.

forcing strength. Maximally deflected stable solutions also decrease in amplitude as k increases, as in Fig. 2.9(b).

Writing (2.4.6) in the form

$$-h_{xx}(x) = \frac{q(1 + kh_x^2(x))^{3/2}}{(1 - h(x))^r} \geq \frac{q}{(1 - h(x))^r} \text{ for } x \in [-1/2, 1/2]$$

immediately demonstrates that the bounds (2.4.3) still hold (but are not necessarily tight) for all $k \geq 0$.

While all the bifurcation diagrams computed using the time-of-flight formulation shown in Fig. 2.9(a) lie entirely within the analytic bounds (2.4.8-2.4.9), this is no longer the case when $k \gtrapprox 2.06$. Figure 2.10(a) shows an example of a single computed bifurcation diagram (for $r = 2$ and $k = 3$) with the known analytic bounds overlaid (dashed curves). The analytic bounds intersect the computed unstable solution branch twice, indicating that the branch of unstable solutions disappears and reappears, shown for several examples in Fig. 2.10(b) ($r = 2$, $k = 3, 6, 9$). This phenomenon is observed for all $r \in [1, 2]$ (although the critical value of k varies with

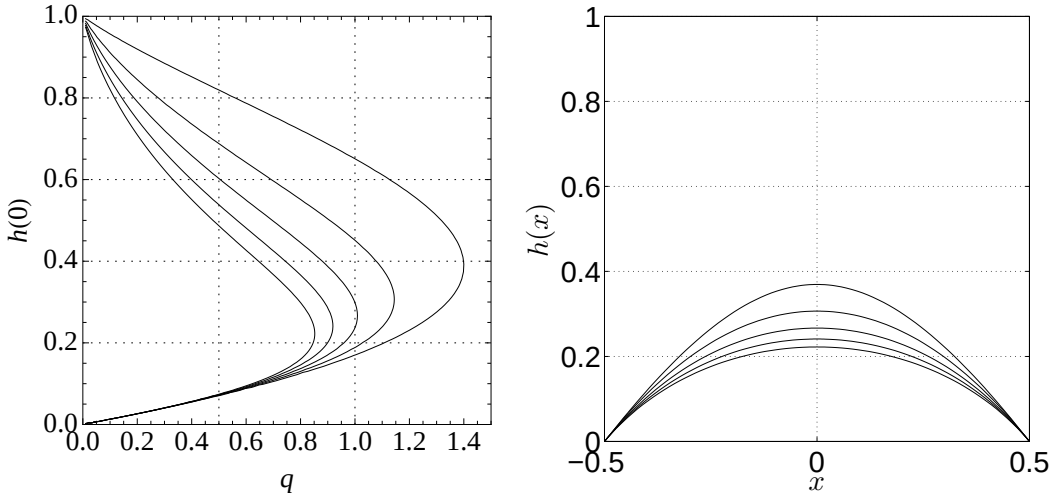

(a) (b)

FIGURE 2.9. (a) Bifurcation structures of (2.4.6), with $r = 2$ and (right to left) $k = 0$, 0.5, 1, 1.25, 2. All diagrams indicate pull-in behavior, occuring for lower forcing strengths as k increases. (b) Maximally-deflected stable solutions of (2.4.6) for (top to bottom) $k = 0$, 0.5, 1, 1.5, 2. Increasing k weakens the restorative elastic force so that pull-in occurs at lower forcing strengths and tip heights.

r).

The 'missing' branch of solutions has recently been shown to be caused by the failure of the original formulation of the MEMS equations to accommodate multi-valued solutions (Brubaker & Lindsay, 2013).

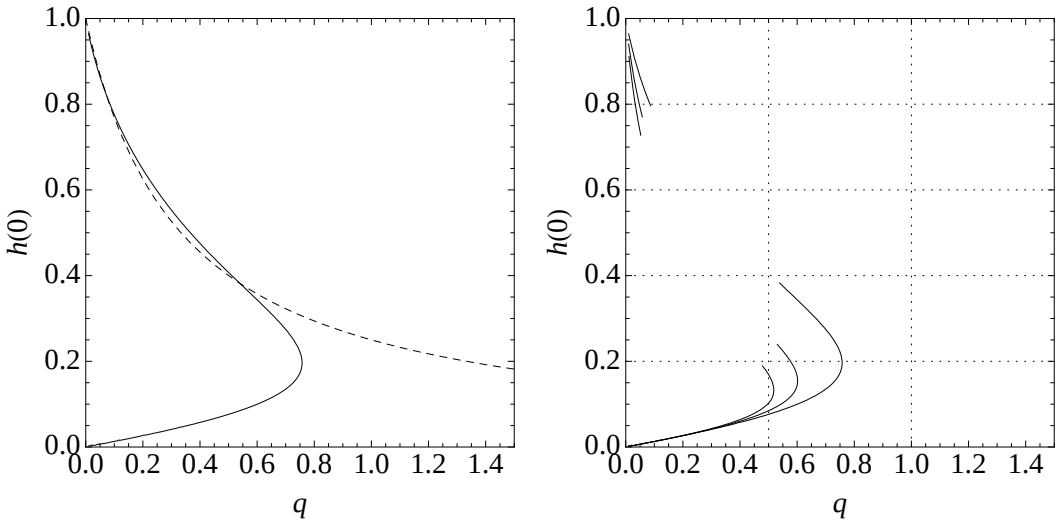

FIGURE 2.10. (a) Bifurcation structure of (2.4.6), with $r = 2$ and $k = 3$. The analytic bounds (2.4.9) are overlaid (dashed curve). (b) Bifurcation structures of (2.4.6), with $r = 2$ and (right to left) $k = 3$, 6, 9, all showing disappearance and reappearance of the unstable branch of solutions.

Chapter 3

Full Electrostatic Models: The Forward Problem

In this chapter we study EMS freed of the simplifying assumptions employed in the MEMS models of Chapter 2. In particular, we focus on systems whose equilibrium configurations are determined by a balance between elastic, electrostatic, and gravitational forces. In the forward problem, we specify properties of the forcing applied to the system - typically the forcing location relative to the undisturbed interface and the type and strength of the forcing - and seek the corresponding equilibrium deflection profiles. Based on the MEMS analysis of Chapter 2, we anticipate the existence of a saddle-node bifurcation in the q-$h(0)$ bifurcation diagram.

We investigate the two main configurations described in the introduction to this thesis (both in the present chapter and those that follow). We recall them here:

A: the true EMS in which the induced electrostatic pressure varies as the square of the electric field near the conducting interface, and the forcing is provided by a point charge fixed above the undeflected interface. This is the base case used to demonstrate the matching technique of Chapter 4.; and

B: a 'modified' EMS in which the induced electrostatic pressure varies linearly with the electric field near the conducting interface, and the forcing is provided by a dipole fixed above the undeflected interface.

The schematic diagram of Fig. 1.3 should be used to visualize both examples. The consideration of configuration B is inspired by the comparison between electromechanical and fluid system structures outlined in the introduction to this thesis - a more detailed comparison is made in §3.1.

In §3.1, dimensionless equations governing each system type are derived. All systems are described by two nondimensional parameters: the forcing strength q and the forcing height l are natural choices. We give formulations in terms of both PDEs and boundary integrals. The numerical method of §3.4 focuses on solving the PDEs directly, but the boundary integral formulation allows for the similar structure underlying the electromechanical and two-layer fluid flow models to be more easily identified.

Small-q deflection profiles for each system type are calculated and compared in §3.2. We find that the perturbative profiles in the two-layer fluid flow model forced by a point sink agree with those of the modified EMS forced by an electric dipole. This identification clarifies the decision to include dipole forcing in configuration B above.

In §3.3, the equations describing configuration A are recast in complex variables. This allows the coupled PDEs governing the equilibrium deflection profile $h(x)$ and the electric potential ϕ above the deflected interface to be reduced to a single ODE for a conformal map $\mathbb{F}$ defined on the closed unit disc $\overline{\mathbb{D}} \subset \mathbb{C}$. $\mathbb{F}$ uniquely determines both h and ϕ. The ODE governing $\mathbb{F}$ is local with respect to the angle θ used to parametrize the unit circle $\partial\mathbb{D}$, and the non-local coupling of the original system of equations is instead absorbed in the 'boundary conditions' applied to $\mathbb{F}$.

The collocation method detailed in §3.4 provides an efficient algorithm for calculating approximate equilibrium deflection profiles of configuration A (and, with minimal adaptation, of configuration B). We define finite dimensional families of conformal maps that produce candidate deflection profiles, and determine the best approximate profile by minimizing the residual pressure experienced by the deflected interfaces within each family. The maps in these families are constructed from finitely many values $\{h_0, \ldots, h_M\}$ representing interface heights at the images of evenly spaced nodes in the preimage plane.

Example profiles computed using the collocation method are shown and discussed

in §3.5. The outlined method fails to produce equilibrium profiles if the deflection is large relative to the forcing height l, a result of the extremely sharp interface geometry exhibited by such deflection profiles and the accumulation of charge that this sharp geometry is necessarily associated with. While problematic for the numerical method described in the present chapter, this accumulation of charge motivates the separate considerations of low-curvature and high-curvature portions of deflection interfaces and underpins the numerical matching method presented in Chapter 4.

3.1 Governing Equations

3.1.1 Point Charge Forcing

The elastic and electrostatic components of the governing equations to be studied in the present chapter were introduced in Chapter 2. We now modify the dimensional equation (2.1.3) to incorporate the stabilizing effect of gravity, and reformulate the boundary conditions appropriately. The elastic interface is assumed to separate two materials of different densities, with the lower material more dense than the upper material by an amount labeled ρ. The pressure balance along the deflected interface $y = h(x)$ then becomes

$$\frac{-Th_{xx}(x)}{(1+h_x^2(x))^{3/2}} + \rho g h(x) = \frac{\varepsilon_0}{2}\frac{\left(-h_x(x)\phi_x(x,h) + \phi_y(x,h)\right)^2}{1+h_x^2(x)} \text{ for } x \in (-\infty,\infty).$$

When forced by a point charge, the system is closed by the equations

$$\begin{aligned} &\nabla^2\phi(x,y) = -\frac{q}{\varepsilon_0}\delta(x,y-l) \text{ in } \{h(x) < y : x \in (-\infty,\infty)\}, \\ &\phi(x,h(x)) = 0 \text{ for } x \in (-\infty,\infty). \end{aligned}$$

Note that there is no explicit equation pinning the interface deflection at an arbitrary length scale L. The combined influences of elasticity and gravity will ensure that $h(x) \to 0$ as $|x| \to 0$.

Rescaling the problem variables: $x = \sqrt{T/\rho g}x'$, $y = \sqrt{T/\rho g}y'$, $h = \sqrt{T/\rho g}h'$ and $\phi = \sqrt{2T^{3/2}/(\rho g)^{1/2}\varepsilon_0}\phi'$ yields the nondimensional equations

$$\frac{-h'_{x'x'}(x')}{(1+h'^2_{x'}(x'))^{3/2}} + h'(x') = \frac{\left(-h'_{x'}(x')\phi'_{x'}(x',h') + \phi'_{y'}(x',h')\right)^2}{1+h'^2_{x'}(x')} \text{ for } x' \in (-\infty,\infty),$$
$$\nabla'^2\phi'(x',y') = -q'\delta(x',y'-l') \text{ in } \{h'(x') < y' : x' \in (-\infty,\infty)\},$$
$$\phi'(x',h'(x')) = 0 \text{ for } x' \in (-\infty,\infty)$$

for q' the dimensionless strength of the forcing charge, and l' the dimensionless height at which the forcing charge is fixed. These are the only two parameters that remain in the problem. We will drop all primes for convenience from this point forward. The equivalent formulation

$$\frac{-h_{xx}(x)}{(1+h_x^2(x))^{3/2}} + h(x) = (\nabla\phi(x,h)\cdot n(x))^2 \text{ for } x \in (-\infty,\infty), \tag{3.1.2a}$$
$$\nabla^2\phi(x,y) = -q\delta(x,y-l) \text{ in } \{h(x) < y : x \in (-\infty,\infty)\}, \tag{3.1.2b}$$
$$\phi(x,h(x)) = 0 \text{ for } x \in (-\infty,\infty) \tag{3.1.2c}$$

where $n = n(x)$ is the unit (upward) normal to the deflected interface at $(x,h(x))$ makes comparison with the governing equation of §3.1.2 easier. The scale $\sqrt{T/\rho g}$ is the capillary length scale, and represents the distance at which gravitational effects begin to dominate elastic tension as a stabilizing influence. Note that all nondimensional lengths are proportions of this scale.

We now rewrite the nondimensional governing equations (3.1.2) in boundary integral form to provide support for the claim that the electromechanical and fluid withdrawal systems share significant structure (see (1.3.1), Table 1.1, and surrounding discussions). We recast each governing equation in terms of the charge density $\sigma(x)$ at each point on the deflected interface, and then treat h and σ (as opposed to h and ϕ) as the (coupled) dependent variables to be determined.

The condition that the interface be in electrostatic equilibrium (3.1.2c) can be

written

$$\underbrace{-\frac{q}{2\pi}\log(x^2+(h(x)-l)^2)}_{\text{potential due to the forcing charge}}+\underbrace{\int_{\mathbb{R}}\sigma(x)K(x;x',h)dA_{x'}}_{\substack{\text{potential due to continuous charge}\\ \text{distribution along deflected interface}}}=0$$

for $x \in (-\infty, \infty)$. The first term in this equation represents the known contribution to the electric potential at $(x, h(x))$ due to the forcing point charge. The second term represents the contribution to the electric potential at $(x, h(x))$ due to a continuous charge distribution with (*a priori* unknown) density σ distributed over the deflected interface. (3.1.2b) is automatically satisfied by this arrangement of charges, by the superposition principle. (3.1.2a) may be written

$$\frac{-h_{xx}(x)}{(1+h_x^2(x))^{3/2}}+h(x)=\sigma^2(x) \text{ for } x\in(-\infty,\infty)$$

using the relationship between the electric field $-\nabla\phi$ and the charge density σ near the surface of conductors discussed in §2.1.2. Combining these two equations yields a single governing equation of the form (1.3.1) with $r = 2$,

$$F(x,h(x))=-\frac{q}{2\pi}\log(x^2+(h(x)-l)^2), \text{ and} \tag{3.1.3a}$$

$$K(x,x';h)=-\frac{1}{2\pi}\log((x-x')^2+(h(x)-h(x'))^2). \tag{3.1.3b}$$

Solutions $h(x)$ of this single integral equation will simultaneously be in both electic and mechanical equilibrium.

3.1.2 Dipole Forcing

The components of the pressure balance equation (3.1.2a) all feature in the modified systems forced by a dipole. The electrostatic pressure term is artificially altered to depend linearly on the electric field at the interface yielding the following governing

equations:

$$\frac{-h_{xx}(x)}{(1+h_x^2(x))^{3/2}} + h(x) = (\nabla\phi(x,h)\cdot n(x)) \text{ for } x \in (-\infty,\infty), \tag{3.1.4a}$$

$$\nabla^2\phi(x,y) = -q\delta_y(x,y-l) \text{ in } \{h(x) < y : x \in (-\infty,\infty)\}, \tag{3.1.4b}$$

$$\phi(x,h(x)) = 0 \text{ for } x \in (-\infty,\infty). \tag{3.1.4c}$$

One side effect of this modification is that the sign of the electrostatic pressure near the tip depends on the sign of q. We therefore pick whichever sign of q produces a positive upward electrostatic force at the interface tip. The total charge induced on the interface must sum to zero (as the forcing charge configuration has zero net charge), and this fact in combination with the linear dependence of induced electrostatic pressure on the induced charge density will necessarily produce electrostatic pressures that act to attract and repel different portions of the interface (in contrast to the true electrostatic problem in the previous section, in which the interface is always drawn towards the point charge by the electrostatic pressure).

3.1.3 Quadrupole Forcing

Although we will not present extensive analysis of the modified EMS forced by a quadrupole, we include the governing equations here to aid later discussion. The singularity term is the only one altered from (3.1.4):

$$\frac{-h_{xx}(x)}{(1+h_x^2(x))^{3/2}} + h(x) = (\nabla\phi(x,h)\cdot n(x)) \text{ for } x \in (-\infty,\infty),$$

$$\nabla^2\phi(x,y) = -q\delta_{yy}(x,y-l) \text{ in } \{h(x) < y : x \in (-\infty,\infty)\},$$

$$\phi(x,h(x)) = 0 \text{ for } x \in (-\infty,\infty).$$

3.1.4 Fluid Sink

In this subsection, we formulate the dimensionless governing equations for selective withdrawal flows modeled by the presence of a fixed sink in the upper fluid layer. This

exercise will elucidate the reasoning behind the modification made to the electrostatic pressure term in (3.1.4). The choice of dipole forcing for the modified electrostatic case is justified in §3.2.3.

We assume that a sink of strength q is located a distance l above the undisturbed interface between two immiscible fluid layers. The upper fluid is very viscous, and the lower fluid inviscid. The lower fluid is the denser of the two layers, and we denote the density difference by ρ. The equations governing the upper fluid flow $\mathbf{u}(x,y) = (u(x,y), v(x,y))$, modified pressure field $P(x,y)$ and the interface deflection $h(x)$ are

$$\frac{-Th_{xx}(x)}{(1+h_x^2(x))^{-3/2}} + \rho g h(x) = n(x)\cdot\tau(x,h(x))\cdot n(x) \text{ for } x\in(-\infty,\infty), \tag{3.1.6a}$$

$$n(x)\cdot\tau(x,h(x))\cdot t = 0 \text{ for } x\in(-\infty,\infty) \tag{3.1.6b}$$

$$\mu\nabla^2\mathbf{u}(x,y) = \nabla P(x,y) \text{ in } \{h(x) < y : x\in(-\infty,\infty)\}, \tag{3.1.6c}$$

$$\nabla\cdot\mathbf{u}(x,y) = 0 \text{ in } \{h(x) < y : x\in(-\infty,\infty)\}, \tag{3.1.6d}$$

$$\mathbf{u}(x,y) \sim -\frac{q}{2\pi}\frac{(x,y-l)}{(x^2+(y-l)^2)} \text{ as } (x,y)\to(0,l),$$

$$\mathbf{u}(x,y)\cdot n(x) = 0 \text{ for } x\in(-\infty,\infty), \tag{3.1.6e}$$

where T and $n(x)$ are defined as for the electrostatic problem, $t(x)$ is the unit vector tangent to the interface at $(x,h(x))$, μ is the viscosity of the upper fluid, and $\tau(x,y)$ is the stress tensor in the upper fluid defined by

$$\tau_{ij}(x,y) = P\delta_{ij} + \mu\left(\frac{\partial u_i}{\partial x_j} + \frac{\partial u_j}{\partial x_i}\right).$$

These equations mimic those governing the electrostatic problems but also include the supplemental requirement that the tangential stress vanish at the fluid-fluid interface (a result of the assumption that the lower fluid is inviscid). Note the linear dependence of the viscous stresses on the velocity gradients $\partial u_i/\partial x_j$ and $\partial u_j/\partial x_i$ in (3.1.6a).

Suitable scalings reduce the system (3.1.6) to

$$\frac{-h_{xx}(x)}{(1+h_x^2(x))^{-3/2}} + h(x) = n(x)\cdot\tau(x,h(x))\cdot n(x) \text{ for } x\in(-\infty,\infty), \tag{3.1.7a}$$

$$n(x)\cdot\tau(x,h(x))\cdot t = 0 \text{ for } x\in(-\infty,\infty) \tag{3.1.7b}$$

$$\nabla^2\mathbf{u}(x,y) = \nabla P(x,y) \text{ in } \{h(x)<y : x\in(-\infty,\infty)\}, \tag{3.1.7c}$$

$$\nabla\cdot\mathbf{u}(x,y) = 0 \text{ in } \{h(x)<y : x\in(-\infty,\infty)\}, \tag{3.1.7d}$$

$$\mathbf{u}(x,y) \sim -\frac{q}{2\pi}\frac{(x,y-l)}{(x^2+(y-l)^2)} \text{ as } (x,y)\to(0,l), \tag{3.1.7e}$$

$$\mathbf{u}(x,y)\cdot n(x) = 0 \text{ for } x\in(-\infty,\infty), \tag{3.1.7f}$$

where all variables are now assumed to be dimensionless and the dimensionless form of τ is given by

$$\tau_{ij}(x,y) = P\delta_{ij} + \left(\frac{\partial u_i}{\partial x_j} + \frac{\partial u_j}{\partial x_i}\right).$$

As before, two parameters q and l remain in the system, and control the nondimensional forcing strength and height (relative to the capillary length scale).

As for the EMS of §3.1.1, we now rewrite the governing equations (3.1.7) in boundary integral form (see (1.3.1), Table 1.1, and surrounding discussions). We recast each governing equation in terms of the Stokeslet density $\sigma(x)$ (a vector quantity) at each point on the deflected interface, and then treat h and σ (as opposed to h and $\mathbf{u}$) as the (coupled) dependent variables to be determined.

The condition that the interface be a streamline of the flow (3.1.7f) can be written

$$\underbrace{-\frac{q}{2\pi}\frac{(x,(h(x)-l)\cdot n}{x^2+(h(x)-l)^2)}}_{\substack{\text{flow due to the}\\ \text{forcing sink}}} + \underbrace{\int_{\mathbb{R}}\sigma(x)K(x;x',h)dA_{x'}}_{\substack{\text{normal flow due to continuous Stokeslet}\\ \text{distribution along deflected interface}}} = 0$$

for $x\in(-\infty,\infty)$. The first term in this equation represents the known contribution to the normal flow field at $(x,h(x))$ due to the forcing sink. The second term represents the contribution to the flow field at $(x,h(x))$ due to a continuous Stokeslet (point force) distribution with (*a priori* unknown) density σ distributed over the deflected

interface and aligned with $n(x)$. (3.1.7e) is automatically satisfied by this arrangement of Stokeslets, by the superposition principle. (3.1.7a) may be written

$$\frac{-h_{xx}(x)}{(1+h_x^2(x))^{3/2}} + h(x) = \sigma(x) \text{ for } x \in (-\infty, \infty)$$

using the relationship between the the stress tensor τ (related to velocity gradients) and the Stokeslet density σ near the fluid-fluid interface. Combining these two equations again yields a single governing equation of the form (1.3.1), this time with $r = 1$. The structural similarity of the electromechanical and fluid systems apart from this change in the value of r is what motivates the consideration of the modified EMS as an approximate model of the two-fluid system.

3.2 Perturbation Solutions

Before considering full numerical solutions of the governing equations in §3.1, we compute small-deflection profiles induced by weak forcing ($|q| \ll 1$).

3.2.1 Electrostatic Point Charge

We posit expansions for $\phi(x, y)$ and $h(x)$ of the forms

$$\phi(x, y) = \sum_{j=1}^{\infty} q^j \phi_j(x, y), \tag{3.2.1a}$$

$$h(x) = \sum_{j=1}^{\infty} q^j h_j(x), \tag{3.2.1b}$$

(since we do not anticipate an $\mathcal{O}(1)$ response to $\mathcal{O}(q)$ forcing) and substitute in (3.1.2). To order q,

$$\begin{aligned} -h_{1,xx}(x) + h_1(x) &= 0, \\ \nabla^2 \phi_1(x, y) &= -\delta(x, y - l), \\ \phi_1(x, 0) &= 0. \end{aligned}$$

The equations for ϕ_1 and h_1 are decoupled. Solving first for h_1, we see that the fundamental solutions $e^{\pm x}$ blow up for large/small x and are therefore non-physical (we require that $h \to 0$ as $|x| \to 0$), so h_1 must be identically zero. ϕ_1 can be determined by applying the standard method of images to the single point charge located at $(0, l)$, yielding

$$\phi_1 = \frac{(-\log(x^2 + (y-l)^2) + \log(x^2 + (y+l)^2))}{4\pi}.$$

At order q^2, the governing equations give

$$\begin{aligned} -h_{2,xx}(x) + h_2(x) &= \left(\frac{\partial \phi_1}{\partial y}(x, 0)\right)^2, \\ \nabla^2 \phi_2(x, y) &= 0, \\ \phi_2(x, 0) &= 0. \end{aligned}$$

Again, the equations governing ϕ_2 and h_2 are decoupled, and we may immediately deduce that ϕ_2 is identically zero. h_2 is determined by the equation

$$h_{2,xx}(x) - h_2(x) = -\frac{l^2}{\pi^2 (x^2 + l^2)^2}$$

with boundary conditions $h \to 0$ as $|x| \to \infty$. This has solution

$$h_2(x) = \frac{l^2}{2\pi^2} \int_{-\infty}^{\infty} \frac{e^{-|x-\xi|}}{\left(\xi^2 + l^2\right)^2} d\xi,$$

so

$$h(x) = \frac{q^2 l^2}{2\pi^2} \int_{-\infty}^{\infty} \frac{e^{-|x-\xi|}}{\left(\xi^2 + l^2\right)^2} d\xi + \mathcal{O}(q^3)$$

for $q \ll 1$. Note that the leading order sheet deflection is positive for all $x \in \mathbb{R}$, regardless of the sign of q. A graphical comparison of both the perturbative solutions computed in this section is provided by Fig. 3.1 on page 51.

3.2.2 Electrostatic Dipole

The procedure we follow for the modified EMS forced by a dipole with moment $q > 0$ at fixed height $l > 0$ is exactly the same as in §3.2.1. After applying the ansätze

(3.2.1) to the governing equations (3.1.4), the leading order equations are

$$\begin{aligned} -h_{1,xx}(x) + h_1(x) &= \frac{\partial \phi_1}{\partial y}(x,0), \\ \nabla^2 \phi_1(x,y) &= -\delta_y(x, y-l), \\ \phi_1(x,0) &= 0. \end{aligned}$$

We may solve this system for ϕ_1 first, followed by h_1. The solution for ϕ_1 comes from the standard method of images, so that

$$\phi_1 = -\frac{1}{2\pi}\left(\frac{y-l}{x^2+(y-l)^2} + \frac{y+l}{x^2+(y+l)^2}\right).$$

The equation governing h_1 becomes

$$h_{1,xx}(x) - h_1(x) = \frac{(x^2-l^2)}{\pi(x^2+l^2)^2}, \tag{3.2.4}$$

from which we calculate

$$h(x) = \frac{q}{2\pi}\int_{-\infty}^{\infty} \frac{(l^2-\xi^2)e^{-|x-\xi|}}{\left(\xi^2+l^2\right)^2} d\xi + \mathcal{O}(q^2).$$

As we identified in §3.1.2, the forcing term $(x^2-l^2)/\pi(x^2+l^2)^2$ changes sign at $x = l$. The boundary is attracted towards the dipole for all $|x| < l$, and is repelled by the dipole for all $|x| > l$.

The normalized small-deflection solutions for each forcing type (and electric field-electrostatic pressure relationship) are compared in Fig. 3.1.

3.2.3 Fluid Sink

For $q \ll 1$, the ansätze

$$\begin{aligned} \mathbf{u}(x,y) &= \sum_{j=1}^{\infty} q^j \mathbf{u}_j(x,y), \\ h(x) &= \sum_{j=1}^{\infty} q^j h_j(x), \\ P(x,y) &= \sum_{j=1}^{\infty} q^j P_j(x,y) \end{aligned}$$

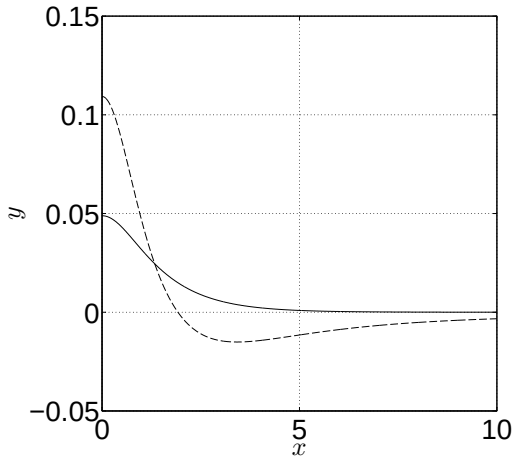

FIGURE 3.1. Leading order small-deflection profiles with point charge ($h_2(x)$, solid line) and dipole ($h_1(x)$, dashed line) forcings ($l = 1$). The dipole profile dips below the undeflected height $y = 0$ - this is possible because the induced electrostatic pressure can vary in sign in the modified electrostatic case.

applied to (3.1.7) produce the leading order system

$$\begin{aligned}
-h_{1,xx}(x) + h(x) &= -P_1(x,0) + 2\frac{\partial v_1}{\partial y}(x,0) \text{ for } x \in (-\infty,\infty),\\
\frac{\partial u_1}{\partial y}(x,0) + \frac{\partial v_1}{\partial x}(x,0) &= 0 \text{ for } x \in (-\infty,\infty),\\
\nabla^2 \mathbf{u}_1(x,y) &= \nabla P_1(x,y) \text{ in } \{h(x) < y : x \in (-\infty,\infty)\},\\
\nabla \cdot \mathbf{u}_1(x,y) &= 0 \text{ in } \{h(x) < y : x \in (-\infty,\infty)\},\\
\mathbf{u}_1 &\sim -\frac{1}{2\pi}\frac{(x,y-l)}{(x^2+(y-l)^2)} \text{ as } (x,y) \to (0,l),\\
v_1(x,0) &= 0.
\end{aligned}$$

This system is solved by $P_1 = 0$ and

$$\mathbf{u}(x,y) = -\frac{1}{2\pi}\frac{(x,y-l)}{(x^2+(y-l)^2)} - \frac{1}{2\pi}\frac{(x,y+l)}{(x^2+(y+l)^2)},$$

(from the method of images), leaving $h_1(x)$ defined by the equation

$$h_{1,xx}(x) - h_1(x) = \frac{2(x^2-l^2)}{\pi(x^2+l^2)^2}.$$

This equation has almost exactly the same form as equation (3.2.4), which governs the deflection profiles of the modified EMS forced by a dipole![1] The perturbation solutions for the modified EMS forced by a pure quadrupole and the fluid system forced by a dipole also agree.

3.3 Recasting in Complex Variables

The governing equations (3.1.2) and (3.1.4) of the true and modified EMS both feature local electrostatic pressures that depend on the geometry of the entire deflection profile $h(x)$ through the boundary condition applied to the electrostatic potential ϕ. This non-local coupling prevents the calculation of closed-form deflection profiles for general q and l, and a numerical treatment is therefore required.

We elect to recast the governing equations in a complex-variable framework and to represent interface deflection profiles as images of the unit circle $\partial\mathbb{D}\backslash\{-1\} = \{w = e^{i\theta} : \theta \in (-\pi, \pi)\}$ under conformal maps $\mathbb{F} : w \mapsto z$. We give two equivalent characterizations of conformal maps below before describing their relationship with harmonic functions (solutions of Laplace's equation). This relationship allows the non-local coupling between electrostatic pressure and deflection profile geometry to be wholly incorporated into the boundary conditions of the reformulated problem rather than appearing explicitly in recast versions of the force balance equations (3.1.2a) and (3.1.4a). The resulting system of equations for $\mathbb{F}$ may be approximately solved using the collocation method described in §3.4 (in particular, the non-local boundary condition is straightforward to satisfy with this approach).

Definition 3.3.1. A map $\mathbb{F}(w)$ defined on $\mathcal{D} \subset \mathbb{C}$ is called *conformal* if it preserves angles.

Theorem 3.3.2. A map $\mathbb{F} : w \mapsto z$ defined on a domain $\mathcal{D} \subset \mathbb{C}$ is conformal if and

[1] The extra factor of two could be absorbed in the rescaling steps to make the equations identical.

only if the function $f(w)$ is analytic and has non-vanishing derivative ($f'(w) \neq 0$) everywhere in $\mathcal{D}$.

We will exploit the latter characterization in §3.4 when our aim is to construct families of conformal maps with finitely many degrees of freedom.

Theorem 3.3.3. Let $\widehat{\phi}$ be harmonic in $\mathcal{D} \subset \mathbb{C}$, and let $f : \mathcal{D} \to \mathcal{D}_0$ defined by $z = f(w) = x(u,v) + iy(u,v)$ be conformal in $\mathcal{D}$. Then the pushed forward function ϕ defined by $\phi(x,y) = \widehat{\phi}(u,v)$ is harmonic in $\mathcal{D}_0$.

Proof of Theorem 3.3.3. The chain rule and Cauchy-Riemann equations together give that $\nabla^2_{x,y}\phi(x,y) = \nabla^2_{u,v}\widehat{\phi}(u,v)/|f'(w)|^2$. Since f' must be non-zero in $\mathcal{D}$ and $\nabla^2_{u,v}\widehat{\phi}(u,v) = 0$ everywhere in $\mathcal{D}$, ϕ is harmonic in $\mathcal{D}_0$. □

When mapping from $\partial\mathbb{D}$ to a candidate deflection profile, the unit disc $\mathbb{D}$ is mapped to the more complicated domain $\{y > h(x)\}$. Since the electric potential corresponding to a point charge located within a circle may be computed exactly, we will use this push-forward theorem to avoid having to solve the coupled equations (3.3.4) for ϕ explicitly. The potential in the image plane obtained in this manner is guaranteed to be unique:

Theorem 3.3.4. Laplace's equation $\nabla^2\phi = 0$ defined on a domain $\mathcal{D} \subset \mathbb{R}^2$ with $\phi = \phi_0$ on $\partial\mathcal{D}$ has a unique solution if ϕ_0 is continuous and $\partial\mathcal{D}$ is sufficiently regular.

For sufficiently smooth boundaries $\partial\mathcal{D}$, uniqueness may be proven using the maximum principle:

Theorem 3.3.5 (Maximum Principle for Harmonic Functions)**.** Let ϕ be a harmonic function defined on a domain $\mathcal{D} \subset \mathbb{R}^2$. If ϕ has a local maximum in $\mathcal{D}$, i.e. if $\exists\ w_0 \in \mathcal{D}$ s.t. $\phi(w) \leq \phi(w_0)$ for all w in a neighborhood of w_0, then ϕ must be constant on $\mathcal{D}$.

In the following subsections we give the details of our reformulation for the true EMS including point charge forcing, and indicate the appropriate modifications for the modified system with dipole and quadrupole forcing.

3.3.1 Electrostatic Point Charge

Let $\mathbb{F}$ be any conformal map defined on the unit disc $\mathbb{D}$ satisfying the conditions

$$\mathbb{F}(\overline{w}) = \overline{\mathbb{F}(w)}, \tag{3.3.1a}$$

$$\mathbb{F}(e^{i\theta}) \to \pm i\infty \text{ as } \theta \to \mp\pi. \tag{3.3.1b}$$

The deflection profile h defined by

$$h(\mathrm{Re}(i\mathbb{F}(e^{i\theta}))) = \mathrm{Im}(i\mathbb{F}(e^{i\theta})) = \mathrm{Re}(\mathbb{F}(e^{i\theta})) \text{ for } \theta \in (-\pi, \pi) \tag{3.3.2}$$

is then a 'viable' candidate solution of system (3.1.2) (i.e. it satisfies the appropriate symmetry and decay conditions, see Fig.s 3.2(a) and 3.2(b)). Any sufficiently regular smooth interface can be represented in this way, according to Theorem 3.4.3.

(3.3.2) expresses the gravitational term in (3.1.2a) in terms of $\mathbb{F}$. The elastic term may be written

$$\kappa(\mathrm{Re}(i\mathbb{F}(e^{i\theta}))) = \frac{\mathrm{Im}(\mathbb{F}_{\theta\theta}(e^{i\theta})\overline{\mathbb{F}_\theta}(e^{i\theta}))}{|\mathbb{F}(e^{i\theta})|^3} \text{ for } \theta \in (-\pi, \pi).$$

To see this, write $\mathbb{F}(e^{i\theta}) = x(\theta) + iy(\theta)$ for $\theta \in (-\pi, \pi)$. Then

$$\begin{aligned}\frac{\mathrm{Im}(\mathbb{F}_{\theta\theta}(e^{i\theta})\overline{\mathbb{F}_\theta}(e^{i\theta}))}{|\mathbb{F}(e^{i\theta})|^3} &= \frac{\mathrm{Im}((x_{\theta\theta} + iy_{\theta\theta})(x_\theta - iy_\theta))}{(x_\theta^2 + y_\theta^2)^{3/2}}, \\ &= \frac{x_\theta y_{\theta\theta} - y_\theta x_{\theta\theta}}{(x_\theta^2 + y_\theta^2)^{3/2}},\end{aligned}$$

which is the standard definition of the signed curvature along a parametrized curve in $\mathbb{R}^2$.

To complete the reformulation, we must compute a representation of the electrostatic pressure term in (3.1.2a) in terms of $\mathbb{F}$.

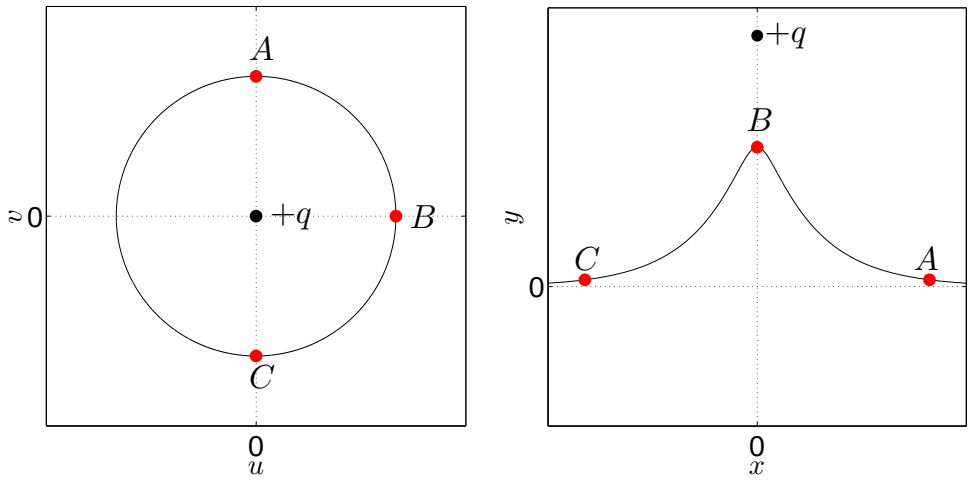

(a) (b)

FIGURE 3.2. (a) Unit circle in the preimage ($w = u + iv$) plane. (b) Example candidate deflection profile $z = x + iy = \{i\mathbb{F}(e^{i\theta}) : \theta \in (-\pi, \pi)\}$ satisfying (3.3.1). The deflection is symmetric about $x = 0$ and decays towards $y = 0$ as $\theta \to \pm\pi$. $\mathbb{F}$ is multiplied by i to align profiles with physical coordinates.

Let $\mathbb{F}(0) = l$ in addition to the conditions given above.[2] The preimage plane potential $\widehat{\phi}$ then solves the equations

$$\nabla^2\widehat{\phi}(u,v) = -q\delta(u,v) \text{ in } \mathbb{D}, \tag{3.3.3a}$$

$$\widehat{\phi}(u,v) = 0 \text{ on } \partial\mathbb{D} \tag{3.3.3b}$$

and may be pushed forward to give the unique solution ϕ of (3.1.2b)-(3.1.2c) by applying Theorems 3.3.3 and 3.3.4. Implicit in this statement is the claim that the preimage plane forcing required to produce a point charge of strength q in the image plane is a point charge of strength q located at $0 = \mathbb{F}^{-1}(l)$. We verify this before proceeding any further.

ϕ and $\widehat{\phi}$ are related by the equation $\phi(i\mathbb{F}(w)) = \widehat{\phi}(w)$.[3] Near $z = il$ (the location

[2]This choice is made without loss of generality, although we will later see that the scaling of $\mathbb{F}$ with respect to the argument θ is influenced by where we choose to locate the preimage plane forcing.

[3]We abuse notation here slightly by writing $\phi(u,v) = \phi(w)$ where $w = u + iv$, and similarly for

of the image plane forcing charge), the electric potential satisfies

$$\phi(z) \sim -\frac{q}{2\pi}\log|z-il| \sim -\frac{q}{4\pi}\log((z-il)(\overline{z}+il)).$$

Similarly, near $w=0$,

$$\begin{aligned}\widehat{\phi}(w) &\sim -\frac{q}{4\pi}\log\left((iw\mathbb{F}_w(0)+\mathcal{O}(w^2))(\overline{iw\mathbb{F}_w(0)}+\mathcal{O}(w^2))\right),\\ &\sim -\frac{q}{2\pi}\left(\log|w|+\log|\mathbb{F}_w(0)|\right)+\mathcal{O}(w).\end{aligned}$$

The constant and $\mathcal{O}(w)$ terms do not affect the singularity type, so we see that a point charge of strength q located at the origin of the w-plane is indeed the appropriate singularity for producing a point charge of strength q at $z=il$ in the z-plane.

The simplified domain geometry of equations (3.3.3) allows their solution to be trivially identified as

$$\widehat{\phi}(w) = -\frac{q}{2\pi}\log|w|.$$

The (normal, inward) electrostatic pressure experienced by $\partial\mathbb{D}$ in the w-plane has magnitude $(q/2\pi)^2$ everywhere. Recalling that the electrostatic pressure in this case varies as the square of the electric field magnitude at the conducting surface, and in turn that the electric field is defined as the gradient of the electric potential, we determine that the (normal, upward) electrostatic pressure experienced by the image interface at $i\mathbb{F}(e^{i\theta})$ has magnitude $(q/2\pi|\mathbb{F}_w(e^{i\theta})|)^2 = (q/2\pi|\mathbb{F}_\theta(e^{i\theta})|)^2$ for all $\theta\in(-\pi,\pi)$. This may be understood intuitively by noting that $|\mathbb{F}_\theta|$ is the multiplicative factor by which equipotentials of $\widehat{\phi}$ are separated when mapping to the image plane, and that increased separation of equipotentials corresponds to a decrease in the electric field strength.

In summary, solving the system of equations (3.1.2) for the deflection profile $h(x)$ and electric potential $\phi(x,y)$ simultaneously may instead be accomplished by identifying the conformal map $\mathbb{F}$ defined on $\overline{\mathbb{D}}$ satisfying $\mathbb{F}(0)=l$ and the conditions (3.3.1)

$\widehat{\phi}$. The interpretation should always be clear.

that solves the single equation

$$-\frac{\mathrm{Im}(\mathbb{F}_{\theta\theta}(e^{i\theta})\overline{\mathbb{F}_{\theta}}(e^{i\theta}))}{|\mathbb{F}_{\theta}(e^{i\theta})|^3}+\mathrm{Re}(\mathbb{F}(e^{i\theta}))=\frac{q^2}{4\pi^2|\mathbb{F}_{\theta}(e^{i\theta})|^2}\text{ for }\theta\in[-\pi,\pi). \tag{3.3.4}$$

We refer to maps solving this equation simply as *solutions* (distinguishing them from the associated deflection profiles). This equation is local in θ, but the corresponding 'boundary condition' $\mathbb{F}(0)=l$ is not. To see this, we use the analyticity of $\mathbb{F}$ in $\mathbb{D}$ to rewrite the condition as an integral constraint in terms of the values of $\mathbb{F}$ on $\partial\mathbb{D}$ only:

$$\mathbb{F}(0)=\frac{1}{2\pi i}\oint_{\partial\mathbb{D}}\frac{\mathbb{F}(w)}{w}dw=\frac{1}{2\pi}\int_{-\pi}^{\pi}\mathbb{F}(e^{i\theta})d\theta=l. \tag{3.3.5}$$

Nevertheless, it is still easier to analyze this recast form of the original governing equations (3.1.2).

3.3.2 Electrostatic Dipole

The foundations of the argument presented in the previous subsection remain the same for the modified electrostatic problem forced by a dipole. The major differences are that the preimage and image dipole strengths are no longer equal, and a little more work is required to find the induced electrostatic pressure in the preimage plane.

Consider an image plane in which charges of strengths q_c and $-q_c$ are located at $z=il$ and $z=i(l+\delta)$ respectively. The potential ϕ of this configuration is given by

$$\phi=-\frac{q_c}{4\pi}\left(\log(x^2+(y-l)^2)-\log(x^2+(y-l-\delta)^2)\right).$$

If we define the charge strength $q_c=q_c(\delta)$ so that $q_c\delta=q$ is a fixed constant, then as $\delta\to 0$,

$$\phi\to-\frac{q}{2\pi}\left(\frac{(y-l)}{x^2+(y-l)^2}\right)=-\frac{q}{2\pi}\left(\frac{\mathrm{Im}(z-il)}{|z-il|^2}\right)=\frac{iq}{4\pi}\left(\frac{(z-il)-(\overline{z}+il)}{(z-il)(\overline{z}+il)}\right).$$

This potential corresponds to that of an ideal dipole of strength q located at $z=il$ and oriented along the imaginary axis.

With $\widehat{\phi}$, ϕ and $\mathbb{F}$ defined as above[4], we note that near $w = 0$,

$$\begin{aligned}
\widehat{\phi}(w) &\sim \frac{iq}{4\pi}\left(\frac{iw\mathbb{F}_w(0) + i\overline{w}\mathbb{F}_w(0) + \mathcal{O}(w^2, \overline{w}^2)}{(iw\mathbb{F}_w(0) + \mathcal{O}(w^2))(-i\overline{w}\mathbb{F}_w(0) + \mathcal{O}(\overline{w}^2))}\right), \\
&\sim -\frac{q}{4\pi}\left(\frac{(w+\overline{w})\mathbb{F}_w(0) + \mathcal{O}(w^2, \overline{w}^2)}{|w|^2\mathbb{F}_w^2(0)}\right)(1 + \mathcal{O}(w, \overline{w})), \\
&\sim -\frac{q}{4\pi}\left(\frac{w+\overline{w}}{|w|^2\mathbb{F}_w(0)}\right) + \mathcal{O}(1), \\
&\sim -\frac{(q/\mathbb{F}_w(0))}{2\pi}\left(\frac{\mathrm{Re}(w)}{|w|^2}\right) + \mathcal{O}(1). \qquad (3.3.6)
\end{aligned}$$

Thus, to produce a dipole of strength q oriented along the imaginary axis in the image plane, we must place a dipole of strength $\widehat{q} = q/\mathbb{F}_w(0)$ oriented along the real axis in the preimage plane.

To compute the electrostatic pressure experienced by $\partial\mathbb{D}$ in the preimage plane, we consider point charges of strengths $-\widehat{q}_c$, $\widehat{q}_c$ and $-\widehat{q}_c$ located at $w = 0$, $w = -\widehat{\delta}$, and $w = -1/\widehat{\delta}$ respectively. Let $\widehat{q}_c(\widehat{\delta})\widehat{\delta} = \widehat{q}$ for all $\widehat{\delta} > 0$. $|w| = \sqrt{u^2 + v^2} = 1$ is an equipotential for all $\widehat{\delta}$:

$$\widehat{\phi_{\widehat{\delta}}} = -\frac{\widehat{q}_c}{4\pi}\Big(-\log\left(u^2+v^2\right) + \log\left((u+\widehat{\delta})^2 + v^2\right) - \log\left(\left(u + \frac{1}{\widehat{\delta}}\right)^2 + v^2\right) - \log(\widehat{\delta}^2)\Big), \qquad (3.3.7)$$

$$\begin{aligned}
&= -\frac{\widehat{q}_c}{4\pi}\left(\log\left(1 + 2u\widehat{\delta} + \widehat{\delta}^2\right) - \log\left(1 + \frac{2u}{\widehat{\delta}} + \frac{1}{\widehat{\delta}^2}\right) - \log(\widehat{\delta}^2)\right), \\
&= -\frac{\widehat{q}_c}{4\pi}\left(\log\left(1 + 2u\widehat{\delta} + \widehat{\delta}^2\right) - \log\left(1 + 2u\widehat{\delta} + \widehat{\delta}^2\right)\right), \\
&= 0,
\end{aligned}$$

where the last term in equation (3.3.7) is chosen to ensure in particular that $\widehat{\phi_{\widehat{\delta}}} = 0$ on $|w| = 1$ without loss of generality. It is straightforward to check that $\widehat{\phi_{\widehat{\delta}}}$ matches the leading order behavior of (3.3.6) with $\widehat{q} = q/\mathbb{F}_w(0)$.

The electric field $\widehat{E}$ is given by $\widehat{E} = -\nabla\widehat{\phi_{\widehat{\delta}}}$ on $|w| = 1$. With the above definition,

[4]Note that $\mathbb{F}_w(0) \in \mathbb{R}$ by symmetry.

we find

$$-\nabla\widehat{\phi}_{\widehat{\delta}} = \frac{\widehat{q}_c\widehat{\delta}}{2\pi}\left(\frac{\frac{(u+\widehat{\delta},v)}{(u+\widehat{\delta})^2+v^2} - \frac{(u,v)}{u^2+v^2}}{\widehat{\delta}} - \frac{\left(u+\frac{1}{\widehat{\delta}},v\right)}{\widehat{\delta}\left(\left(u+\frac{1}{\widehat{\delta}}\right)^2+v^2\right)}\right).$$

For $\widehat{\delta} \ll 1$,

$$\begin{aligned}-\nabla\widehat{\phi}_{\widehat{\delta}} &= \frac{\widehat{q}}{2\pi}\left(\frac{\partial}{\partial u}\left(\frac{(u,v)}{u^2+v^2}\right) - (1,0) + \mathcal{O}(\widehat{\delta})\right), \\ &= \frac{\widehat{q}}{2\pi}\left(\frac{v^2-u^2}{(u^2+v^2)^2} - 1, \frac{-2uv}{(u^2+v^2)^2}\right) + \mathcal{O}(\widehat{\delta}).\end{aligned}$$

On $u^2+v^2=1$, then,

$$-\nabla\widehat{\phi}_{\widehat{\delta}} = \frac{\widehat{q}}{2\pi}\left(v^2-u^2-1, -2uv\right) + \mathcal{O}(\widehat{\delta})$$

Taking n to be the *inward* normal[5], we can compute the normal and tangential components of the electric field at the cylinder surface:

$$\begin{aligned}\widehat{E}\cdot n &= -\nabla\widehat{\phi}_{\widehat{\delta}}\cdot(-u,-v) = \frac{\widehat{q}u}{\pi} + \mathcal{O}(\widehat{\delta}) = \frac{\widehat{q}\cos\theta}{\pi} + \mathcal{O}(\widehat{\delta}) \\ \widehat{E}\cdot t &= -\nabla\widehat{\phi}_{\widehat{\delta}}\cdot(-v,u) = \ldots = 0\end{aligned}$$

(There are no order $\widehat{\delta}$ corrections in the final expressions for $\widehat{E}\cdot t$, since the cylinder is an equipotential for all $\widehat{\delta}$).

In the limit $\widehat{\delta}\to 0$, the induced charge density at $w=e^{i\theta}$ is given by $\widehat{q}\cos(\theta)/\pi$. The reformulated equation governing conformal maps in the modified electrostatic model forced by a dipole is therefore

$$-\frac{\mathrm{Im}(\mathbb{F}_{\theta\theta}(e^{i\theta})\overline{\mathbb{F}_\theta}(e^{i\theta}))}{|\mathbb{F}_\theta(e^{i\theta})|^3} + \mathrm{Re}(\mathbb{F}(e^{i\theta})) = \frac{(q/\mathbb{F}_w(0))\cos(\theta)}{\pi|\mathbb{F}_\theta(e^{i\theta})|} \text{ for } \theta\in[-\pi,\pi), \qquad (3.3.8)$$

where the sign of q is chosen so that $q/\mathbb{F}_w(0)>0$.

[5]This will correspond to the 'upward' normal, i.e. the normal directed toward the forcing dipole, in the image plane.

3.3.3 Electrostatic Quadrupole

The preimage plane forcing required to produce a pure quadrupole in the image plane is not itself a pure quadrupole. We calculate the required preimage plane forcing using the Taylor series expansion as before.

Consider an image plane in which the imaginary axis is a flat conducting sheet, and charges of strengths $-2q_c$, q_c, and q_c are located at $z = il$, $z = i(l+\delta)$, and $z = i(l-\delta)$ respectively.

The potential ϕ of this configuration is given by

$$\phi = -\frac{q_c}{4\pi}\left(-2\log(x^2+(y-l)^2) + \log(x^2+(y-l-\delta)^2) + \log(x^2+(y-l+\delta)^2)\right).$$

If we define the charge strength $q_c = q_c(\delta)$ so that $q_c\delta^2 = q$ is a fixed constant, then as $\delta \to 0$,

$$\begin{aligned}
\phi &\to -\frac{q}{2\pi}\left(\frac{x^2-(y-l)^2}{(x^2+(y-l)^2)^2}\right), \\
&= -\frac{q}{2\pi}\left(\frac{\mathrm{Re}[(z-il)^2]}{|z-il|^4}\right), \\
&= -\frac{q}{4\pi}\left(\frac{(z-il)^2+(\overline{z}+il)^2}{(z-il)^2(\overline{z}+il)^2}\right).
\end{aligned}$$

This potential corresponds to that of an ideal linear quadrupole of strength q located at $z = il$ and oriented along the imaginary axis.

With $\widehat{\phi}$, ϕ and $\mathbb{F}$ defined as above, we note that near $w = 0$,

$$\widehat{\phi}(w) \sim -\frac{(q/\mathbb{F}_w^2(0))}{2\pi}\left(-\frac{\mathrm{Re}(w^2)}{|w|^4}\right) - \frac{(q\mathbb{F}_{ww}(0)/\mathbb{F}_w^3(0))}{2\pi}\left(\frac{\mathrm{Re}(w)}{|w|^2}\right) + \mathcal{O}(1). \quad (3.3.9)$$

The asymptotic behavior (3.3.9) of the potential $\widehat{\phi}$ is that of a quadrupole of strength $\widehat{q}_1 \equiv q/\mathbb{F}_w^2(0)$ *and* a dipole of strength $\widehat{q}_2 \equiv q\mathbb{F}_{ww}(0)/\mathbb{F}_w^3(0)$ superimposed at the origin in the w-plane. Since the induced charge density depends linearly on the electric potential, we may compute the induced electrostatic pressure on $\partial\mathbb{D}$ due to the combined singularities (3.3.9) by adding the known density induced by a dipole

of strength $\widehat{q}_2$ fixed at $w = 0$ (see §3.3.2) to the charge density induced by a pure quadrupole of strength $\widehat{q}_1$ fixed at $w = 0$. We calculate the latter density now, following the same path as in §3.3.2.

Consider the preimage plane with point charges of strengths $-2\widehat{q}_c$, $\widehat{q}_c$, $\widehat{q}_c$, $-\widehat{q}_c$, and $-\widehat{q}_c$ located at $w = 0$, $w = \widehat{\delta}$, $w = -\widehat{\delta}$, $w = 1/\widehat{\delta}$, and $w = -1/\widehat{\delta}$ respectively. Let $\widehat{q}_c(\widehat{\delta})\widehat{\delta}^2 = \widehat{q}$ for all $\widehat{\delta} > 0$.

We first check that $|w| = \sqrt{u^2 + v^2} = 1$ is an equipotential for all δ.

$$\begin{aligned}
\widehat{\phi}_{\widehat{\delta}} &= -\frac{\widehat{q}_c}{4\pi}\left(-2\log\left(u^2+v^2\right) + \log\left((u+\widehat{\delta})^2+v^2\right) + \log\left((u-\widehat{\delta})^2+v^2\right)\right. \\
&\quad \left. - \log\left(\left(u+\frac{1}{\widehat{\delta}}\right)^2+v^2\right) - \log\left(\left(u-\frac{1}{\widehat{\delta}}\right)^2+v^2\right) - 2\log\left(\widehat{\delta}^2\right)\right), \qquad (3.3.10) \\
&= -\frac{\widehat{q}_c}{4\pi}\left(\log\left(1+2u\widehat{\delta}+\widehat{\delta}^2\right) + \log\left(1-2u\widehat{\delta}+\widehat{\delta}^2\right) - \log\left(1+\frac{2u}{\widehat{\delta}}+\frac{1}{\widehat{\delta}^2}\right)\right. \\
&\quad \left. - \log\left(1-\frac{2u}{\widehat{\delta}}+\frac{1}{\widehat{\delta}^2}\right) - 2\log\left(\widehat{\delta}^2\right)\right), \\
&= 0,
\end{aligned}$$

where the last term in equation (3.3.10) is chosen to ensure in particular that $\widehat{\phi}_{\widehat{\delta}} = 0$ on $|w| = 1$ without loss of generality. It is straightforward to check that $\widehat{\phi}_{\widehat{\delta}}$ matches the leading order behavior of (3.3.9) with $\widehat{q} = q/\mathbb{F}_w^2(0)$.

The electric field $\widehat{E}$ is given by $\widehat{E} = -\nabla\widehat{\phi}_{\widehat{\delta}}$ on $|w| = 1$. With the above definition, we find that

$$\begin{aligned}
-\nabla\widehat{\phi}_{\widehat{\delta}} &= \frac{\widehat{q}}{2\pi}\left(\frac{\partial^2}{\partial u^2}\left(\frac{(u,v)}{u^2+v^2}\right) - 2(-u,v) + \mathcal{O}(\widehat{\delta})\right), \\
&= \frac{\widehat{q}}{\pi}\left(\frac{u(u^2-3v^2)}{(u^2+v^2)^3} + u, -\frac{v(v^2-3u^2)}{(u^2+v^2)^3} - v\right) + \mathcal{O}(\widehat{\delta})
\end{aligned}$$

for $\widehat{\delta} \ll 1$. On $u^2 + v^2 = 1$, then,

$$-\nabla\psi_{\widehat{\delta}} = \frac{\widehat{q}}{\pi}\left(u(1+u^2-3v^2), -v(1+v^2-3u^2)\right) + \mathcal{O}(\widehat{\delta}).$$

Taking n to be the inward normal as before, we can compute the normal and tangential

components of the electric field at the cylinder surface:

$$E \cdot n = -\nabla\psi_{\widehat{\delta}} \cdot (-u, -v) = \ldots = \frac{2\widehat{q}(v^2 - u^2)}{\pi} + \mathcal{O}(\widehat{\delta}) = -\frac{2\widehat{q}\cos(2\theta)}{\pi} + \mathcal{O}(\widehat{\delta}),$$
$$E \cdot t = -\nabla\psi_{\widehat{\delta}} \cdot (-v, u) = \ldots = 0.$$

In the limit $\widehat{\delta} \to 0$, the induced charge density at $w = e^{i\theta}$ due to the preimage plane quadrupole alone is given by $-2\widehat{q}\cos(2\theta)/\pi$. Combining with the induced charge density due to the preimage plane dipole, we find that the reformulated equation governing conformal maps in the modified electrostatic model forced by a quadrupole is therefore

$$-\frac{\mathrm{Im}(\mathbb{F}_{\theta\theta}(e^{i\theta})\overline{\mathbb{F}_\theta}(e^{i\theta}))}{|\mathbb{F}_\theta(e^{i\theta})|^3} + \mathrm{Re}(\mathbb{F}(e^{i\theta})) = \frac{-2(q/\mathbb{F}_w^2(0))\cos(2\theta)}{\pi|\mathbb{F}_\theta(e^{i\theta})|} + \frac{(q\mathbb{F}_{ww}(0)/\mathbb{F}_w^3(0))\cos(\theta)}{\pi|\mathbb{F}_\theta(e^{i\theta})|} \text{ for } \theta \in [-\pi, \pi),$$

where the sign of q is chosen so that $-2q/\mathbb{F}_w^2(0) + q\mathbb{F}_{ww}(0)/\mathbb{F}_w^3(0) > 0$.

3.4 Collocation Method

In this subsection, we describe a collocation method for calculating approximate solutions of (3.3.4) which also extends easily to (3.3.8). It may seem most natural to specify the 'physical' parameters l and q that appear in the formulations (3.1.2) and (3.1.4) and to aim to compute the corresponding equilibrium interface deflection $h(x)$ directly. However, we anticipate a saddle node bifurcation structure in which a single forcing strength q can produce both a (small-deflection) stable and a (large-deflection) unstable equilibrium profile, so the problem is better posed if we instead specify l and $h(0)$ as inputs to the system and allow q to be determined as part of the numerical solution.

As stated in the introduction to this chapter, our method is based on seeking the 'best' approximate solution of (3.3.4) from within finite-dimensional families of

candidate solutions (conformal maps). For a candidate map $\mathbb{F}$, the residual pressure experienced by the corresponding deflected interface at $i\mathbb{F}(e^{i\theta})$ is equal to

$$-\frac{\mathrm{Im}(\mathbb{F}_{\theta\theta}(e^{i\theta})\overline{\mathbb{F}_{\theta}}(e^{i\theta}))}{|\mathbb{F}_{\theta}(e^{i\theta})|^3}+\mathrm{Re}(\mathbb{F}(e^{i\theta}))-\frac{q^2}{4\pi^2|\mathbb{F}_{\theta}(e^{i\theta})|^2}. \tag{3.4.1}$$

By definition, the residual pressure is zero everywhere if $\mathbb{F}$ solves (3.3.4) exactly. We therefore identify the best approximate solution of (3.3.4) within any given family of candidate solutions as the map that minimizes the residual pressure along the corresponding deflected interface.

All members of the one dimensional family of functions

$$\mathbb{G}(w)=\mathbb{A}\left(\frac{1-w}{1+w}\right),\ \mathbb{A}\in\mathbb{R}$$

map $\partial\mathbb{D}\backslash\{-1\}=\{w=e^{i\theta}:\theta\in(-\pi,\pi)\}$ to a flat interface:

$$i\mathbb{G}(e^{i\theta})=i\mathbb{A}\left(\frac{1-e^{i\theta}}{1+e^{i\theta}}\right)=\mathbb{A}\tan(\theta/2).$$

A natural way to extend this one dimensional family of maps to finite dimensional families capable of describing symmetrically deflected interfaces is to add a truncated Taylor series with real-valued coefficients $\mathbb{B}_0,\ldots,\mathbb{B}_M$ centered at $w=0$:

$$\mathbb{G}(w)=\mathbb{A}\left(\frac{1-w}{1+w}\right)+\sum_{n=0}^{M}\mathbb{B}_n w^n. \tag{3.4.2}$$

Functions of this form are clearly analytic everywhere in $\mathbb{D}$. The conditions

$$\mathbb{G}(1)=\mathbb{A}+\mathbb{B}_0=l, \tag{3.4.3a}$$

$$\mathbb{G}(0)=\sum_{n=0}^{M}\mathbb{B}_n=h(0), \tag{3.4.3b}$$

$$\lim_{\theta\to\pm\pi}\mathrm{Re}\left(\mathbb{G}(e^{i\theta})\right)=\sum_{n=0}^{M}\mathbb{B}_n(-1)^n=0, \tag{3.4.3c}$$

$$\mathbb{G}_w(w)=\frac{-2\mathbb{A}}{(1+w)^2}+\sum_{n=1}^{M}n\mathbb{B}_n w^{n-1}\neq 0 \text{ for any } w\in\overline{\mathbb{D}}-\{-1\}, \tag{3.4.3d}$$

collectively guarantee that $\mathbb{G}$ is a feasible candidate solution of (3.3.4) (i.e. the corresponding interface satisfies all of the required boundary and symmetry conditions). (3.4.3a) and (3.4.3b) fix the charge and interface tip heights respectively, (3.4.3c) forces the asymptotic interface deflection to be zero without loss of generality, and (3.4.3d) ensures that $\mathbb{G}$ is conformal in $\overline{\mathbb{D}}\backslash\{-1\}$. A necessary condition for a function of the form (3.4.2) mapping $\mathbb{D}$ to $\mathbb{C}$ to be injective (and therefore conformal everywhere in $\mathbb{D}$) is provided by de Brange's theorem:

Theorem 3.4.1 (de Brange's Theorem)**.** If a function of the form

$$f(w) = w + \sum_{n=2}^{\infty} f_n w^n \tag{3.4.4}$$

mapping $\mathbb{D}$ to $\mathbb{C}$ is injective (and therefore conformal everywhere in $\mathbb{D}$), the coefficients f_n must satisfy

$$|f_n| \leq n \text{ for all } n \geq 2.$$

Rewriting

$$\begin{aligned}
\mathbb{G}(w) &= \mathbb{A}\left(\frac{1-w}{1+w}\right) + \sum_{n=0}^{M} \mathbb{B}_n w^n, \\
&= \mathbb{A}(1-w)(1+w)^{-1} + \sum_{n=0}^{M} \mathbb{B}_n w^n, \\
&= \mathbb{A}(1-w)\sum_{n=0}^{\infty}(-w)^n + \sum_{n=0}^{M} \mathbb{B}_n w^n, \\
&= \mathbb{A} + \sum_{n=1}^{\infty} 2\mathbb{A}(-1)^n w^n + \sum_{n=0}^{M} \mathbb{B}_n w^n, \\
&= (\mathbb{A} + \mathbb{B}_0) + \sum_{n=1}^{M}(2\mathbb{A}(-1)^n + \mathbb{B}_n)w^n + \sum_{n=M+1}^{\infty} 2\mathbb{A}(-1)^n w^n,
\end{aligned}$$

(an expansion that is valid for $|w| < 1$, i.e. in all of $\mathbb{D}$), we see that the function $(\mathbb{G}(w) - (\mathbb{A} + \mathbb{B}_0))/(-2\mathbb{A} + \mathbb{B}_1)$ is of the form (3.4.4). Theorem 3.4.1 may therefore

be used as a quick check of condition (3.4.3d) for candidate solutions of (3.3.4).[6]

$\mathbb{G}(e^{i\theta})$ and the derivatives $\mathbb{G}_\theta(e^{i\theta})$ and $\mathbb{G}_{\theta\theta}(e^{i\theta})$ may all be represented in terms of the coefficients $\{\mathbb{A}, \mathbb{B}_0, \ldots, \mathbb{B}_M\}$:

$$\mathbb{G}(e^{i\theta}) = -i\mathbb{A}\tan(\theta/2) + \sum_{n=0}^{M} \mathbb{B}_n e^{in\theta}, \tag{3.4.5a}$$

$$\mathbb{G}_\theta(e^{i\theta}) = -\frac{i\mathbb{A}\sec^2(\theta/2)}{2} + \sum_{n=0}^{M} in\mathbb{B}_n e^{in\theta}, \tag{3.4.5b}$$

$$\mathbb{G}_{\theta\theta}(e^{i\theta}) = -\frac{i\mathbb{A}\sec^2(\theta/2)\tan(\theta/2)}{2} - \sum_{n=0}^{M} n^2\mathbb{B}_n e^{in\theta}. \tag{3.4.5c}$$

For any $N > M$ a power of two, the trivially extended functions

$$\mathbb{G}(e^{i\theta}) = -i\mathbb{A}\tan(\theta/2) + \sum_{n=-N+1}^{N} \mathbb{B}'_n e^{in\theta}, \tag{3.4.6a}$$

$$\mathbb{G}_\theta(e^{i\theta}) = -\frac{i\mathbb{A}\sec^2(\theta/2)}{2} + \sum_{n=-N+1}^{N} in\mathbb{B}'_n e^{in\theta}, \tag{3.4.6b}$$

$$\mathbb{G}_{\theta\theta}(e^{i\theta}) = -\frac{i\mathbb{A}\sec^2(\theta/2)\tan(\theta/2)}{2} - \sum_{n=-N+1}^{N} n^2\mathbb{B}'_n e^{in\theta}, \tag{3.4.6c}$$

with coefficients

$$\mathbb{B}'_n = \begin{cases} \mathbb{B}_n, & n = 0, \ldots, M, \\ 0, & \text{otherwise} \end{cases}$$

may be efficiently evaluated at the evenly-spaced nodes $\{e^{ij\theta/N} : j = -N+1, \ldots, N\}$ using the Fast Fourier Transform (FFT). Suitable combinations of the resulting values yield a vector containing samples of the full residual pressure (3.4.1).

Direct minimization of the norm of the sampled residual pressure vectors with respect to the stretching coefficient $\mathbb{A}$ and Taylor series coefficients $\{\mathbb{B}_0, \ldots, \mathbb{B}_M\}$ would be straightforward to implement (using built-in MATLAB routines) at this stage. However, the response of the residual pressure to changes in individual coefficients

[6]This check is imperfect since non-analytic functions may also satisfy (3.4.1), but can be implemented in code with very little computational cost.

is not localized (each coefficient affects the residual pressure at every point on the corresponding interface) and the resulting minimization problem is therefore poorly conditioned. To combat this, we will now reparametrize our existing families of candidate maps (3.4.2) in terms of the original stretching coefficient $\mathbb{A}$ and a new set of real values $\{h_0, \ldots, h_M\}$ representing the candidate interface height (i.e., the real part of the corresponding conformal map) at the nodes $\{e^{ij\pi/M} : j = 0, \ldots, M\}$ that replace the Taylor series coefficients $\{\mathbb{B}_0, \ldots, \mathbb{B}_M\}$ as parametrizing variables.

Our reformulation is based on the following general result:

Lemma 3.4.2. Let $f(w)$ be any analytic function defined on the upper half plane $\mathcal{U}$. Write $\mathcal{H}$ for the Hilbert Transform, the linear operator defined by

$$\mathcal{H}[f](z) = \frac{1}{\pi}\mathrm{PV}\int_{-\infty}^{\infty}\frac{f(x)}{x-z}dx. \tag{3.4.7}$$

Then the real and imaginary parts of f satisfy the relationships

$$\mathrm{Re}(f(w)) = -\mathrm{Im}(\mathcal{H}[f](w)), \tag{3.4.8a}$$

$$\mathrm{Im}(f(w)) = \mathrm{Re}(\mathcal{H}[f](w)), \tag{3.4.8b}$$

for all $w \in \mathbb{R}$ $(= \partial\mathcal{U})$, i.e. specifying the real (resp. imaginary) part of the boundary values of a function analytic in the upper half plane completely determines the corresponding imaginary (resp. real) part of the boundary values.

An analogous relationship must exist for analytic functions defined on $\mathbb{D}$ (precisely the type of functions appearing in the reformulation (3.3.4)) as a result of the Riemann Mapping Theorem:

Theorem 3.4.3 (Riemann Mapping Theorem)**.** If $\mathcal{D}$ is a non-empty simply-connected proper open subset of $\mathbb{C}$, then there exists a bijective analytic function f from $\mathcal{D}$ onto the unit disc $\mathbb{D} \equiv \{w : |w| < 1\}$.

We will first leverage the analog of Lemma 3.4.2 in the domain $\mathbb{D}$ to construct analytic maps of the form

$$\mathbb{F}(w) = \sum_{n=0}^{\infty} \mathbb{B}_n w^n \tag{3.4.9}$$

from a given real-valued boundary value function $\mathbb{U}(e^{i\theta}) = \mathrm{Re}(\mathbb{F}(e^{i\theta}))$ defined on all of $\partial\mathbb{D}$, and then determine the appropriate adaptations required to construct analytic maps of the form (3.4.2) from a finite sample of real boundary values $\{h_j = \mathrm{Re}(\mathbb{F}(e^{ij\pi/M})) : j = 0, \ldots, M\}$.

Let $\mathbb{U}(e^{i\theta})$ be any real-valued function defined on $\partial\mathbb{D}$ satisfying the symmetry condition $\mathbb{U}(e^{i\theta}) = \mathbb{U}(e^{-i\theta})$. We can always expand $\mathbb{U}$ in a Fourier series:

$$\begin{aligned}\mathbb{U}(e^{i\theta}) &= \sum_{n=-\infty}^{\infty} \mathbb{U}_n e^{in\theta}, \\ &= \mathbb{U}_0 + \sum_{n=1}^{\infty} (\mathbb{U}_n + \mathbb{U}_{-n})\cos(n\theta) + i(\mathbb{U}_n - \mathbb{U}_{-n})\sin(n\theta)\end{aligned}$$

with coefficients satisfying $\overline{\mathbb{U}_n} = \mathbb{U}_{-n}$ (since $\mathbb{U}(e^{i\theta})$ is real-valued) and $\mathbb{U}_n = \mathbb{U}_{-n}$ (since $\mathbb{U}(e^{i\theta}) = \mathbb{U}(e^{-i\theta})$) for all $n \geq 0$. Together these conditions imply that $\mathbb{U}_n \in \mathbb{R}$ for all n, and therefore that

$$\mathbb{U}(e^{i\theta}) = \mathbb{U}_0 + \sum_{n=1}^{\infty} 2\mathbb{U}_n \cos(n\theta).$$

$\mathbb{U}(e^{i\theta})$ is easily seen to be the restriction of the function $\sum_{n=-\infty}^{\infty} \mathbb{U}_n w^n$ (defined on $\overline{\mathbb{D}}$) to the unit circle $\partial\mathbb{D}$. Unsurprisingly, this extended function is not analytic everywhere in $\mathbb{D}$ - the imaginary part of the boundary value function was set equal to zero without regard for the relationships given in Lemma 3.4.2. However, we may exploit the Fourier series representation of $\mathbb{U}(e^{i\theta})$ to easily construct a new complex-valued boundary value function $\mathbb{V}(e^{i\theta})$ such that $\mathrm{Re}(\mathbb{V}(e^{i\theta})) = \mathbb{U}(e^{i\theta})$ for all $\theta \in (-\pi, \pi)$ and whose extension to $\overline{\mathbb{D}}$ *is* analytic everywhere in $\mathbb{D}$. We define

$$\mathbb{V}(e^{i\theta}) = \sum_{n=0}^{\infty} \mathbb{V}_n e^{in\theta}$$

with coefficients

$$\mathbb{V}_n = \begin{cases} \mathbb{U}_0, & n = 0, \\ \mathbb{U}_n + \mathbb{U}_{-n} = 2\mathbb{U}_n, & n \geq 1. \end{cases} \tag{3.4.10}$$

The extension $\sum_{n=0}^{\infty} \mathbb{V}_n w^n$ of $\mathbb{V}(e^{i\theta})$ to $\overline{\mathbb{D}}$ contains no negative powers of w and is therefore analytic in $\mathbb{D}$ as desired.

If we begin with a finite sample of real boundary values $\{h_j = \mathrm{Re}(\mathbb{G}(e^{ij\pi/M})) : j = 0, \ldots, M\}$ rather than a function $\mathbb{U}$ defined on all of $\partial\mathbb{D}$, we may use the FFT to compute the (unique) set of coefficients $\{\mathbb{B}_n^*\}$ such that

$$\sum_{n=-M+1}^{M} \mathbb{B}_n^* \left(e^{ij\pi/M}\right)^n = [h_{M-1}, h_{M-2}, \ldots, h_1, h_0, h_1, \ldots, h_{M-1}, h_M]_{j+M},$$

for $j = -M+1, \ldots, M$. Since $(e^{ij\pi/M})^n = (e^{ij\pi/M})^{n+2M}$ for all $j \in \{-M+1, \ldots, M\}$, we have made a *choice* in selecting exponents n that lie between $-M+1$ and M for this representation. This particular range ensures that the extension $\sum_{-M+1}^{M} \mathbb{B}_n^* w^n$ of (3.4) to $\overline{\mathbb{D}}$ contains negative powers of w - a desired outcome that preserves the importance of the relationships between real and imaginary parts of boundary values of analytic functions as described by Lemma 3.4.2.

Defining $\mathbb{U}(e^{i\theta})$ on $\partial\mathbb{D}$ by[7]

$$\mathbb{U}(e^{i\theta}) = \sum_{n=-M+1}^{M} \mathbb{B}_n^* e^{in\theta} = \mathbb{B}_0 + \mathbb{B}_M e^{iM\theta} + \sum_{n=1}^{M-1} 2\mathbb{B}_n^* \cos(n\theta),$$

we immediately see that the complex-valued boundary function

$$\mathbb{V}(e^{i\theta}) = \sum_{n=0}^{M} \mathbb{B}_n e^{in\theta}$$

with coefficients

$$\mathbb{B}_n = \begin{cases} \mathbb{B}_n^*, & n = 0, M, \\ \mathbb{B}_n^* + \mathbb{B}_{-n}^* = 2\mathbb{B}_n^*, & n = 1, \ldots, M-1, \end{cases} \tag{3.4.11}$$

[7]Because $\mathbb{B}_M^* e^{iM\theta}$ is not 'paired' with any other term, $\mathbb{U}$ is complex-valued on $\partial\mathbb{D}$ except at the nodes $\{e^{ij\pi/M} : j = -M+1, \ldots, M\}$.

satisfies $\mathrm{Re}(\mathbb{V}(e^{ij\pi/M})) = \mathbb{U}(e^{ij\pi/M}))$ for $j = -M+1, \ldots, M$ and has analytic extension $\sum_{n=0}^{M} \mathbb{B}_n w^n$ to $\mathbb{D}$. This extended function exactly matches the deflection term in (3.4.2), so once the coefficients $\{\mathbb{B}_0, \ldots, \mathbb{B}_M\}$ are computed in terms of the interface heights $\{h_0, \ldots, h_M\}$ all sampling and subsequent minimization of the residual pressure may be performed using padded expressions of the forms (3.4.6) and the FFT.

Sample code demonstrating this implementation can be found in Appendix A.

3.5 Numerical Solutions

3.5.1 Point Charge Forcing

We begin by calculating interface deflections and the corresponding bifurcation diagrams with 'intermediate'[8] values of l for the true electrostatic problem forced by a point charge. Figure 3.3(a) shows computed profiles for $l = 1$, $M = N = 256$, and various tip heights $0 < h(0) \leq 0.96$. (We will typically set $N = M$ unless otherwise noted.) Deflection profiles are computed sequentially beginning with a small-deflection profile (for which reasonably accurate initial values of the parameters $\{h_0, \ldots, h_M\}$ may be estimated using the perturbation solutions of §3.2.1). At the k^{th} step of the sequence, the final values of the parameters $\{h_0^{(k-1)}, \ldots, h_M^{(k-1)}\}$ corresponding to the computed profile with tip height $h^{(k-1)}(0)$ are rescaled by $h^{(k)}(0)/h^{(k-1)}(0)$ to provide a starting point for the minimization algorithm that produces a profile with tip height $h^{(k)}(0)$ (the sample code provided in Appendix A demonstrates this implementation). Even with this incremental approach, the minimization code fails to converge for $h(0) > 0.96$ due to poor conditioning of the objective function. The interface tips sharpen as $h(0) \to l$. Figure 3.3(b) shows bifurcation diagrams plotting $h(0)$ against q for forcing heights $l \in \{0.25, 0.5, 0.75, 1\}$, so that the dimensional forcing height is of the same order of magnitude as the capillary length scale. The

[8] This notion will be clarified in §4.1.1.

final accurate solution found is marked with a solid dot in each case. All diagrams appear to be approaching the limiting case $(q, h(0)) = (0, l)$ (also marked with a solid dot) before the sequential collocation method breaks down. A failure of this type is seen for all $l < \sqrt{2}$. Additionally, every diagram features a saddle-node bifurcation corresponding to the existence of a critical forcing strength q_c beyond which no equilibrium deflection exists (i.e. pull-in occurs), as expected. The smaller-deflection branch of solutions is always stable; the larger-deflection branch is always unstable.

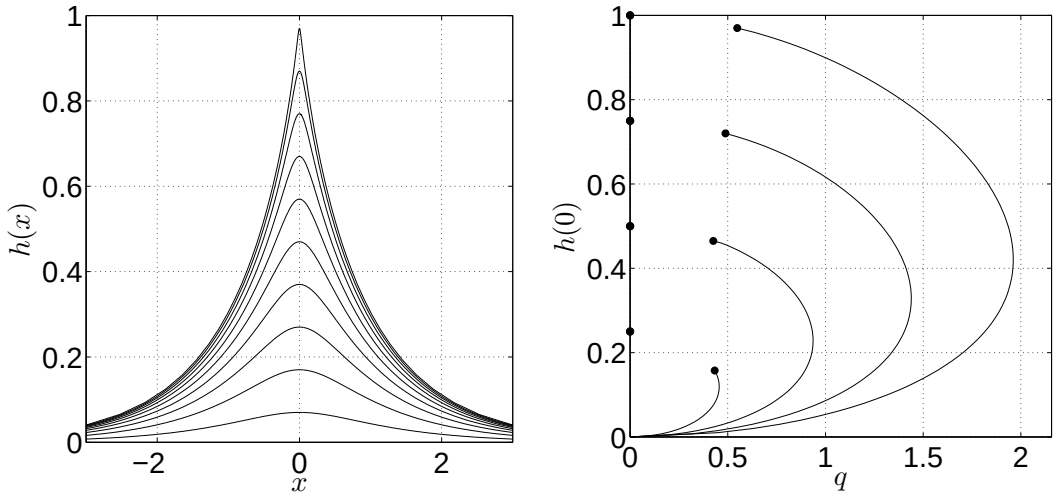

FIGURE 3.3. (a) Computed deflection profiles for $l = 1$, $M = N = 256$, various tip heights. The collocation method of §3.4 fails to produce profiles for any $h(0) > 0.96$. (b) Bifurcation diagrams showing tip height $h(0)$ plotted against computed forcing strength q, $l \in \{0.25, 0.5, 0.75, 1\}$. Each diagram shows a saddle node bifurcation, implying the existence of a critical forcing strength q_c beyond which pull-in occurs. The unstable solution branches all appear to approach $(q, h(0)) = (0, l)$, but the collocation method fails before this point is reached in each diagram.

The breakdown of the collocation method is due to the poor conditioning of the applied algorithm, particularly for solutions with $h(0)$ close to l (our initial guess is therefore not good enough, even when using the sequential scheme). Though the objective function responds in a localized manner to changes in individual h_j values as hoped (Fig. 3.4(a)), the range of sensitivities to perturbations in the interface

heights $\{h_0, \ldots, h_M\}$ exhibited by the sampled residual pressure increases rapidly as $h(0)$ approaches l (Fig.s 3.4(a) and 3.4(b)).

Another potential pitfall when computing profiles with $h(0)$ close to l may be identified by returning to the pressure balance equation (3.3.4). The gravitational term is always $\mathcal{O}(l)$, so equilibrium profiles featuring relatively high tip curvature (which include the profiles of Fig. 3.3(a) with $h(0)$ close to l) are necessarily supported by high electrostatic pressure concentrated near the interface tip. In our conformal mapping-based representation of deflection profiles, the relative density of the images $\{i\mathbb{F}(e^{in\pi/M}) : n = 0, \ldots, M-1\}$ of the evenly spaced nodes $\{e^{in\pi/M} : n = 0, \ldots, M-1\}$ acts a proxy for the induced charge density on the deflected interface - this is most easily observed by studying the dependence of the electrostatic pressure term in (3.3.4) on $\mathbb{F}_\theta$. Image nodes for profiles with high tip curvature therefore tend to accumulate near the interface tip, which leaves the deflection profile far from the tip extremely poorly resolved (see Fig.s 3.6(a) and 3.6(b)). Increasing N can avoid this problem, but at significant computational cost (the FFT is performed many times in evaluating residuals for candidate solutions, and the FFT itself is of order $N \log(N)$).

Finally, we note that M must be chosen large enough to resolve the desired deflection profile (and in particular, the high-curvature interface tip). Figure 3.5 explores the effect of varying M on the accuracy of computed profiles. The moderately-deflected test profile $l = 1$, $h(0) = 0.25$ is used for illustration. All deflections were computed with $N = 512$ to guarantee that the profile is well-resolved for large x. The maximum values of the sampled residual pressures along the computed solutions are plotted against M. Unsurprisingly, families of candidate solutions with fewer degrees of freedom are unable to approximate true deflection profiles as well as families with many degrees of freedom. (This graph should in fact be monotone decreasing - the final increase at $M = 512$ is likely a result of the minimization algorithm terminating before reaching the true minimum due to poor conditioning.)

Figures 3.7(a) and 3.7(b) show the magnitude of each term in (3.3.4) for the

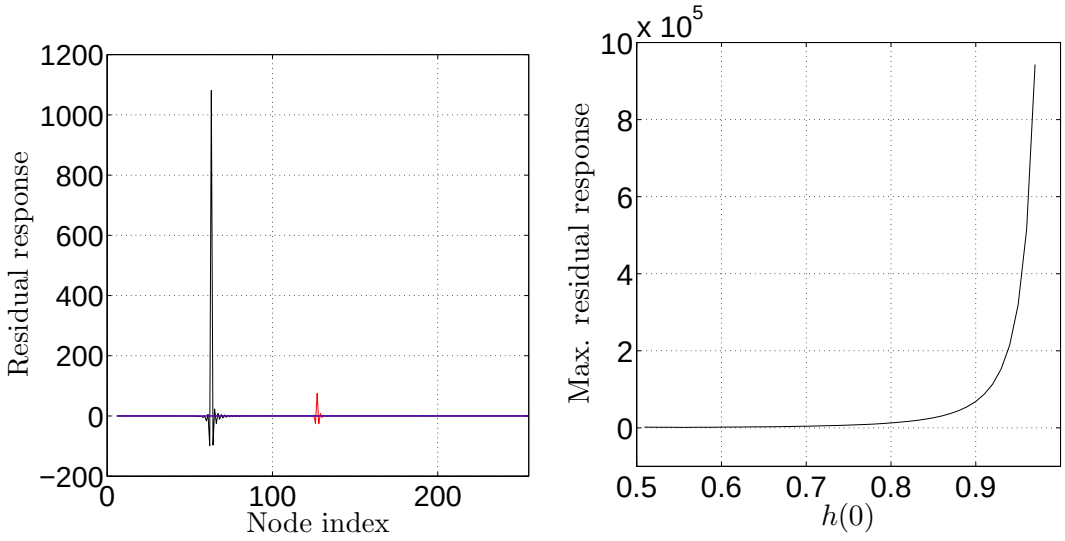

FIGURE 3.4. (a) The change in the sampled residual pressure at each image node induced by 1% perturbations to the values of the parameters h_{64} (black), h_{128} (red) and h_{192} (blue) describing the computed profile for $l = 1$ and $h(0) = 0.21$. The responses to each change are fairly localized, but the sizes span several orders of magnitude. (b) For $l = 1$ and tip heights $h(0)$ between 0.5 and 0.96, we plot the maximum change in the sampled residual pressure over all image nodes induced by 1% perturbations to the values of $\{h_0, \ldots, h_M\}$. This maximum increases as $h(0) \to l$, supporting our claim that the conditioning of the problem worsens as $h(0)$ approaches l.

maximally deflected interface of Fig. 3.3(a). Figure 3.7(a) confirms that the pressure balance near the tip (the 'inner' region, in which x is $\mathcal{O}(l - h(0))$) is between the elastic and electrostatic terms. Inspecting the same balance for $\mathcal{O}(1)$ x-values (the 'outer' region) shows that the interface relaxation is due to a balance between the restorative gravitational and elastic forces. Although not demonstrated by these plots, we predict the existence a third region ($x \gg 1$) in which electrostatic forces balance gravitational forces. This is based on the deduction that, for h small, a profile produced by a balance between the elastic and gravitational terms of (3.1.2a) will satisfy the approximate equation $-h_{xx}(x)+h(x) = 0$. The solution of this system

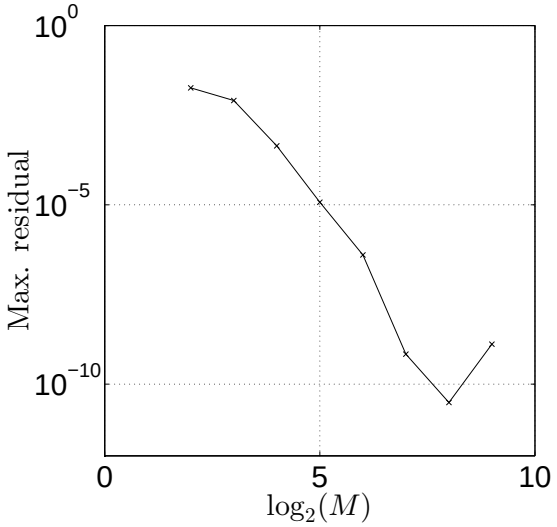

FIGURE 3.5. Plots of the maximum residual pressure along computed profiles with $l = 1$, $h(0) = 0.25$, $N = 512$, as a function of the number of Taylor series coefficients M used to represent the interface deflection. Since N is large, the interface is well represented for all values of x. If M is too small, the best fit solution is still poor (the residual is relatively large). Increasing M should produce monotonically decreasing maximum residual - the increase observed at the final plotted value of M is a result system conditioning causing early termination of the minimization algorithm.

(with the appropriate decay for large x) is $h = h(0)e^{-x}$, so that both gravitational and elastic terms will become exponentially small if this balance persists. This is faster decay than the induced electrostatic pressure will exhibit, so the electrostatic pressure necessarily becomes important again for large enough x.

Figures 3.8(a) and 3.8(b) show the same force balances as Fig.s 3.7(a) and 3.7(b) but for an interface of intermediate deflection $h(0) = 0.46$ relative to the forcing height $l = q$ (see Fig. 3.3(a)). Figure 3.8(a) illustrates that the electrostatic and elastic terms still dominate (but much less definitively so) near the interface tip, and that the slower decay of the electrostatic pressure that results from this less-concentrated induced charge distribution delays the onset of the outer region in which the interface relaxes due to elasticity and gravity. This reduced concentration also allows the 'outer outer' region described above, in which the electrostatic pressure

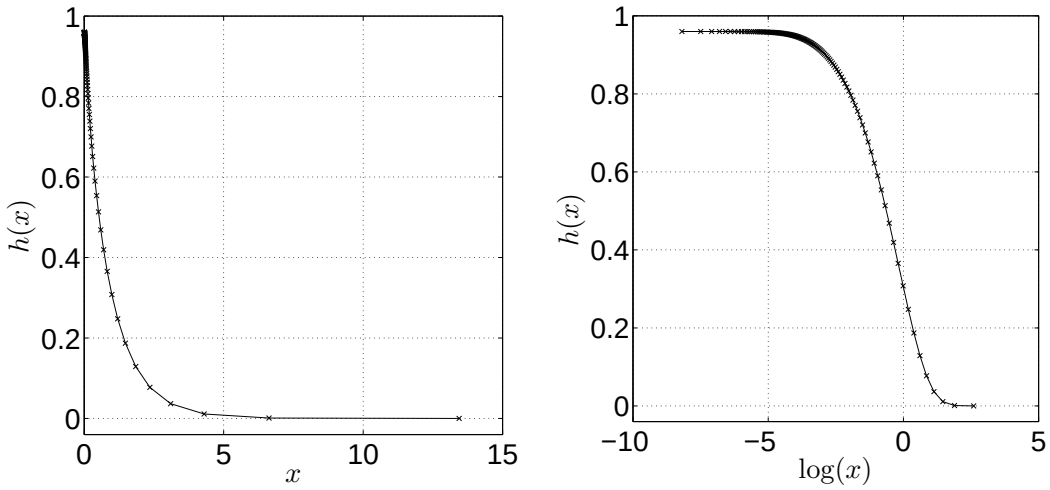

FIGURE 3.6. Deflection profile computed with $l = 1$, $h(0) = 0.96$, $M = N = 256$. (a) The density of the image nodes $\{\mathbb{F}(e^{ij\pi/2M}) : j = 0, \ldots, M-1\}$ decreases rapidly away from the interface tip. This leaves the decaying portion of the interface poorly resolved. (b) A semi-log plot of the same interface confirms that the near-tip region is extremely well-resolved.

balances gravity for all large enough x, to be identified. The interface deflection at the transition between the outer and 'outer outer' regions is five orders of magnitude smaller than the tip deflection $h(0)$, and this ratio should be expected to increase as $h(0)$ increases towards l. We therefore ignore this region in the matching algorithm of §4.1 under the assumption that the error introduced in doing so is many orders of magnitude smaller than the error induced by the matching itself.

The tendency for image nodes to accumulate near regions of relatively high interface curvature, known as *crowding*, is ubiquitous when using conformal maps defined on $\mathbb{D}$ to represent interfaces that feature very disparate length scales (Wegmann, 2005; Porter, 2005). This is not a peculiarity of the conformal mapping based method: alternative methods that we could have applied, including boundary element methods based on the boundary integral formulations given earlier, or direct minimization of the total system energy, must all be adapted to deal with the disparate length scales

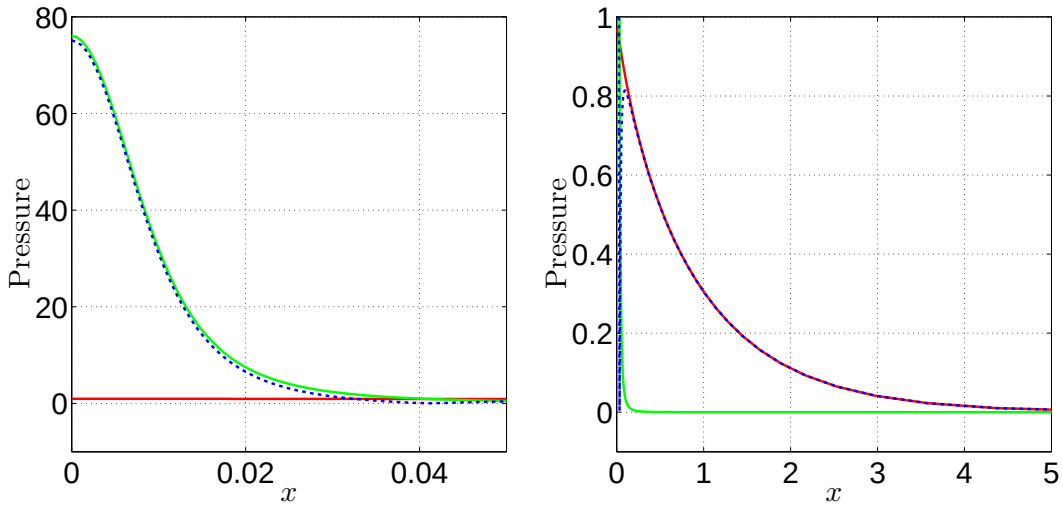

FIGURE 3.7. The magnitude of the electrostatic (green), elastic (blue) and gravitational (red) terms in (3.3.4) for the computed equilibrium deflection profile with $l = 1$ and $h(0) = 0.96$. (a) The balance near the interface tip is between elastic and electrostatic forces as claimed. (b) Away from the high-curvature tip, the interface relaxes under the influences of gravitational and elastic forces.

that characterize stiff problems. (Wilkening, 2011) adapts a collocation method similar to our own by allowing preimage plane node density to respond to the curvature of the image interface - the penalty we would pay for doing this in our formulation would be an increase in computational expense when implementing the Hilbert transformation.

Rather than rapidly increasing the number of computed residual pressures or adaptively alter the spacing of our preimage nodes to accommodate the crowding of image nodes near sharp tips (and giving up the efficiency of the FFT in the process), we will instead leverage the separation of the interface behavior into clearly-defined regions featuring different primary pressure balances to construct the matching algorithm of §4.1. This algorithm allows for solutions with $h(0)$ very close to l to be calculated accurately and efficiently. More discussion is given in the introduction to Chapter 4.

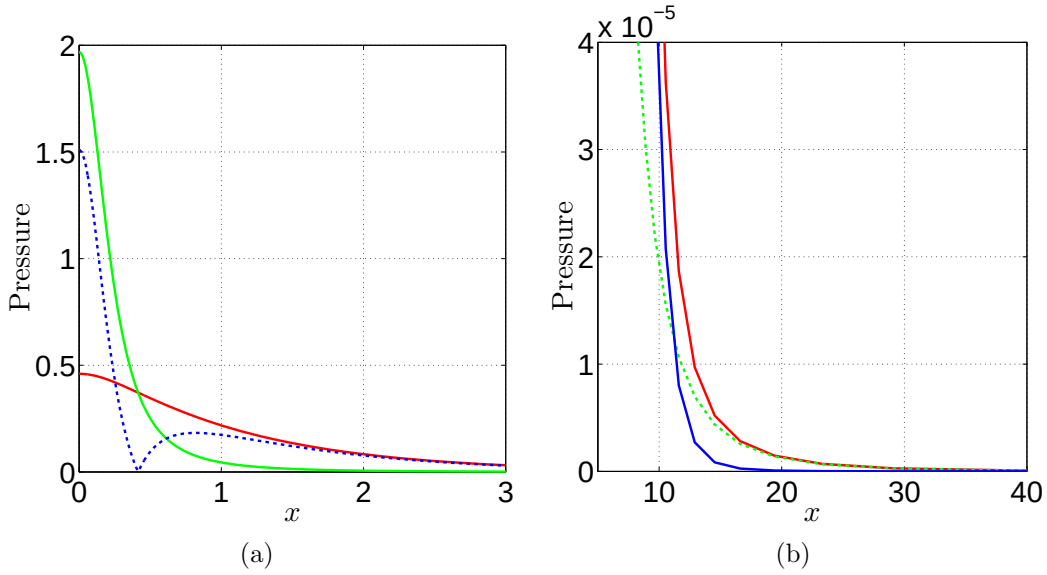

FIGURE 3.8. The magnitude of the electrostatic (green), elastic (blue) and gravitational (red) terms in (3.3.4) for the computed equilibrium deflection profile with $l = 1$ and $h(0) = 0.46$. (a) Elastic and electrostatic terms still dominate near the interface tip, but the gravitational term is of the same order of magnitude. The electrostatic pressure decays much more slowly than in Fig. 3.7(b). (b) The slower decay allows us to confirm the existence of a third region for $x \gg 1$ in which electrostatic pressure balances the gravitational term.

We now inspect solutions and bifurcation diagrams computed with $l > \sqrt{2}$.[9] Figure 3.9(a) shows bifurcation diagrams computed for $l \in \{1, 2, 3, 4, 5\}$ (left to right). Structurally, these bifurcation diagrams match those calculated with values of $l < 1$: all exhibit a saddle node bifurcation which implies the existence of a pull-in instability. However, the branches of unstable solutions no longer appear to approach the points $(0, l)$, and the tip deflections of maximally-deflected stable solutions vary little as l increases from two to five. The magnitude of the tip curvature of maximally-deflected stable solutions decreases as l increases, while the critical forcing strength q_c at which pull-in occurs increases approximately linearly with l.

In Fig. 3.3(b), the bifurcation diagrams all terminate when the collocation method

[9]The dichotomy that exists around $l = \sqrt{2}$ is uncovered in §4.1.1.

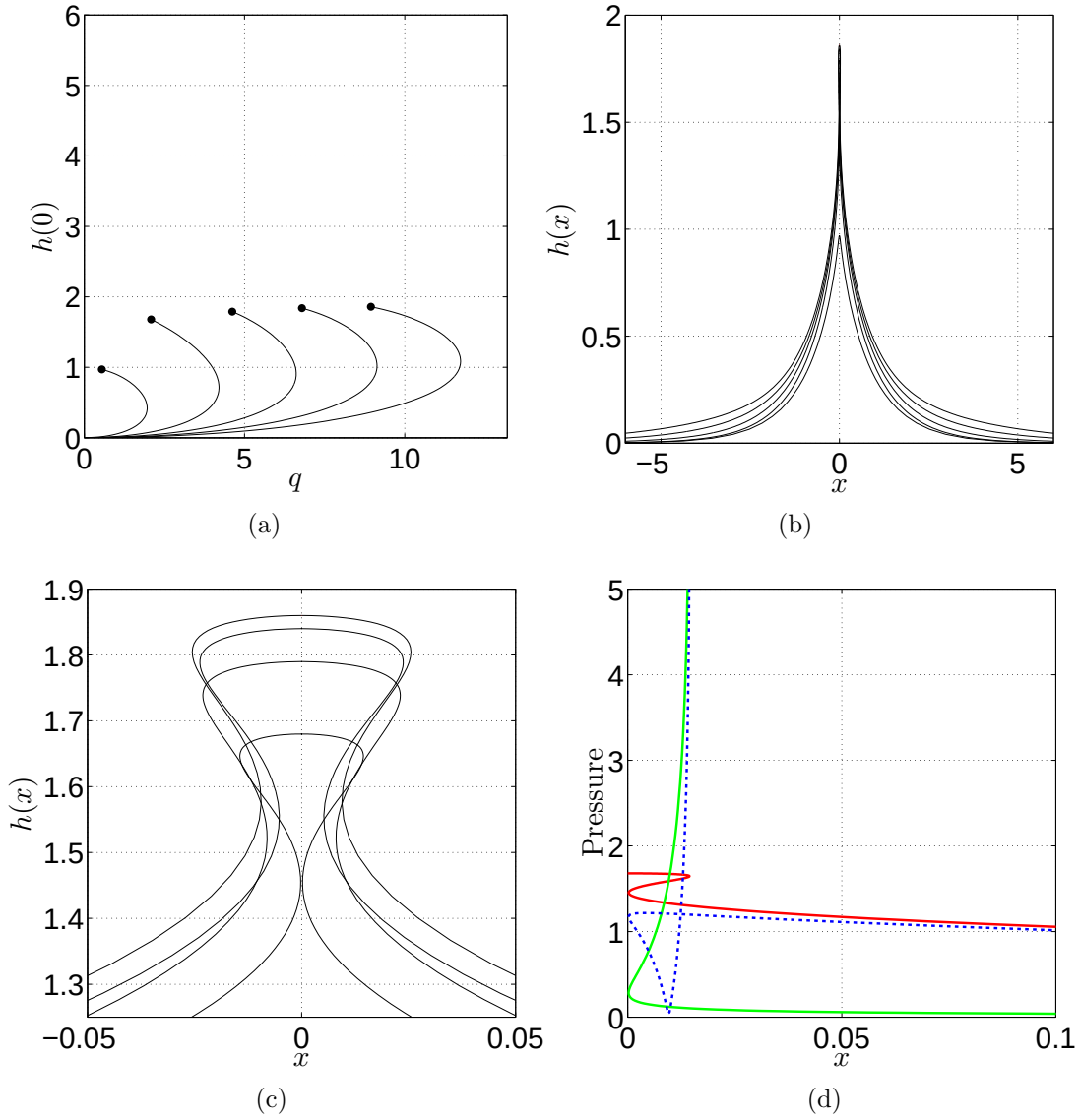

FIGURE 3.9. (a) Bifurcation diagrams showing tip height $h(0)$ plotted against computed forcing strength q, $l \in \{1, 2, 3, 4, 5\}$ (left to right). The unstable solution branches for $l > \sqrt{2}$ do not appear to approach $(q, h(0)) = (0, l)$. (b) Final physical computed solutions for $l \in \{1, 2, 3, 4, 5\}$ (bottom to top). (c) Zoomed view of the profile tips from (b) for $l \in \{2, 3, 4, 5\}$. (d) The magnitude of the electrostatic (green), elastic (blue) and gravitational (red) terms in (3.3.4) for the computed equilibrium deflection profile with $l = 2$ and $h(0) = 1.68$.

fails to produce a solution within a reasonable number of iterations. For $l > \sqrt{2}$, this is no longer the cause for the termination of the unstable branches of solutions at the marked points. Figure 3.9(b) shows the final computed solutions for (bottom to top) $l \in \{1, 2, 3, 4, 5\}$. The narrow columns that cap the solutions for $l > \sqrt{2}$ are distinguished more clearly in Fig. 3.9(c) (solutions for $l \in \{2, 3, 4, 5\}$ shown, bottom to top). All feature a pinched neck. Any of the computed solutions with greater tip heights self-intersect and are therefore discarded as non-physical. The variation in neck widths is due only to the resolution used in stepping $h(0)$ when calculating bifurcation diagrams, and every forcing height $l > \sqrt{2}$ is capable of supporting unstable equilibrium profiles in which the pinched neck is arbitrarily narrow. Figure 3.9(d) compares the magnitudes of each term in (3.3.4) for the maximally-deflected stable solution corresponding to forcing height $l = 2$. We note from this that the electrostatic-elastic balance is only dominant in the portion of the interface that lies above the overhang shown in Fig. 3.9(c). As for solutions with $l < \sqrt{2}$, away from the tip the primary behavior is due to a balance between elastic and gravitational terms. Though not shown, the eventual balance between gravitational and electrostatic terms previously plotted in Fig. 3.8(b) also appears for $x \gg 1$ and h many orders of magnitude smaller than $h(0)$.

3.5.2 Dipole Forcing

In this section we compute interface deflection profiles and bifurcation diagrams for the modified electrostatic problem forced by a dipole. We follow the path of the previous section, and begin by studying systems with $0 < l < 1$. We again find that below a critical value of l, all deflection profiles remain one-to-one, and the collocation method breaks down when the interface tip becomes too sharp and the outer region of the interface is no longer accurately represented. For larger values of l, all systems feature profiles with folded tips, and the bifurcation diagrams for these systems all

terminate when the interface attempts to self-intersect.

Figure 3.10(a) shows interface deflection profiles computed with $l = 1$ for a range of $h(0)$ values. All interfaces dip below $y = 0$ and subsequently approach $y = 0$ from below as $x \to \infty$. The final computed solution in this case exhibits a folded tip, Fig. 3.10(b). This is not a feature of systems with smaller forcing height l, as demonstrated by the computed profiles of Fig. 3.10(c) in which $l = 0.25$.

The bifurcation structures of systems with $l \in \{0.25, 0.5, 0.75, 1\}$ are shown in Fig. 3.10(d). All show a saddle-node bifurcation associated with a pull-in instability. The unstable solution branches all appear to approach $(q, h(0)) = (0, l)$.

As before, we inspect the components of the governing pressure balance equation for a maximally-deflected profile to determine which balance dominates in each portion of the interface. Figure 3.11(a) confirms that the inner region profile behavior is still dominated by the interplay between electrostatic and elastic terms. The 'intermediate' region in which all three terms are of the same order of magnitude begins near the profile overhang and extends to $\mathcal{O}(1)$ values of x (Fig. 3.11(b)). The outer region balance of Fig. 3.11(c) shows most change when compared to the equivalent plot for point charge forcing (Fig. 3.7(b)). The primary balance for $x \gtrapprox 3$ is between electrostatic and gravitational forces. The argument we outlined for point charge forcing to deduce that this balance must always dominate for large enough x remains valid here, but the onset is much earlier than for the point charge profiles (recall that Fig. 3.8(b) shows exactly how late this onset is in one example with point charge forcing). There is no region in which gravitational and elastic forces alone control the relaxation of the interface. This discrepancy is a result of the sign change present in the electrostatic pressure term of (3.3.8) and absent from the equivalent point charge formulation (3.3.4). With point charge forcing, an accumulation of negative charge near the interface tip necessarily results in very rapidly decaying charge density away from the tip. With dipole forcing, this is no longer true - when the negative portion of the induced charge is highly concentrated, an equal amount of positive charge remains

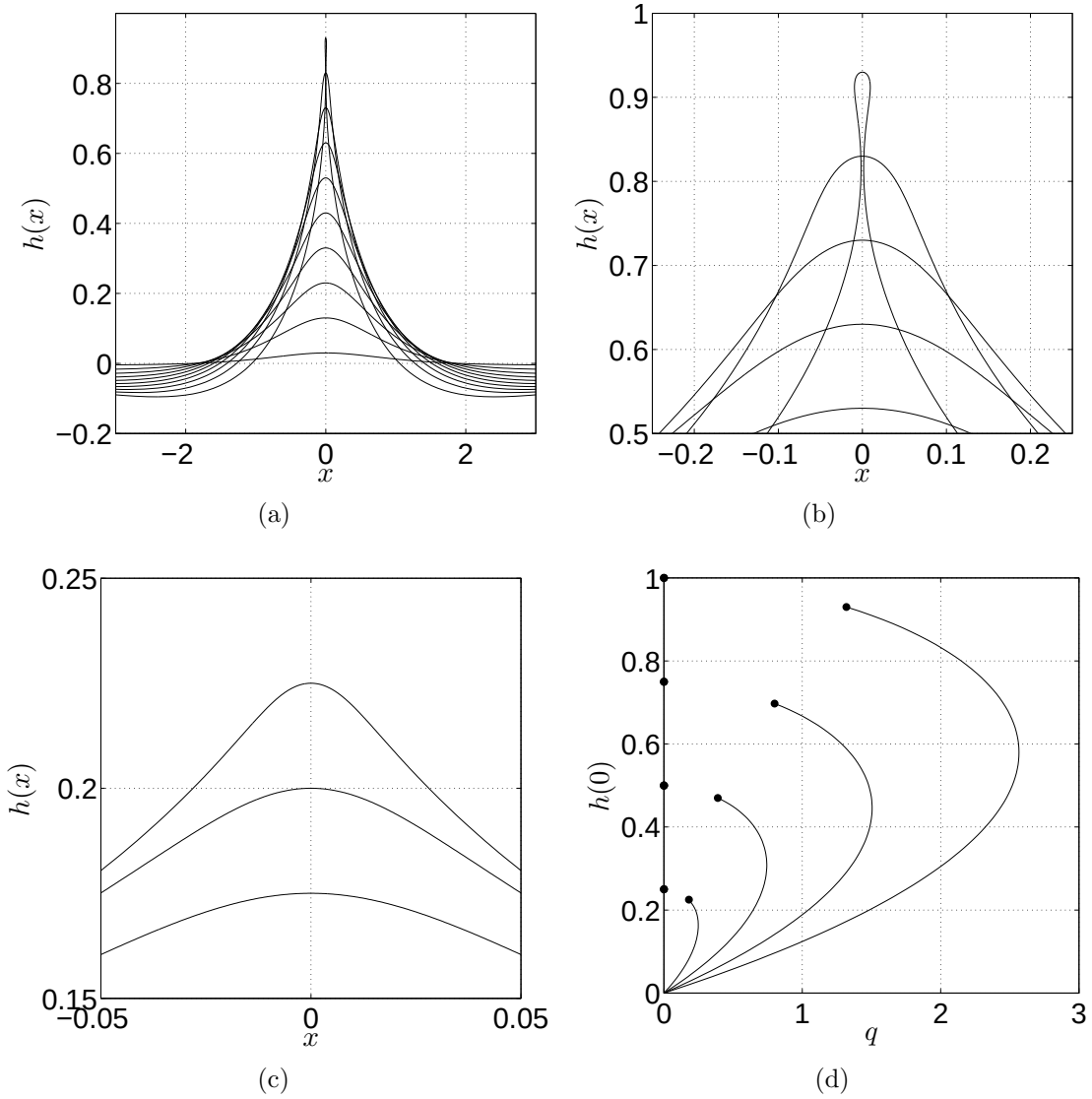

FIGURE 3.10. (a) Computed deflection profiles for $l = 1$, $M = 256$, various tip heights. The collocation method of §3.4 fails to produce profiles for any $h(0) > 0.93$. (b) Zoomed view of the profile tips from (a). (c) Computed deflection profile tips for $l = 0.25$, $M = 256$, various tip heights. The final computed deflection profile is one-to-one, unlike that of (a). (d) Bifurcation diagrams showing tip height $h(0)$ plotted against computed forcing strength q, $l \in \{0.25, 0.5, 0.75, 1\}$. All imply the existence of pull-in instabilities.

to be distributed over the remaining portion of the interface (the net induced charge must be zero, since there is no net forcing charge) and the corresponding density can decay much more slowly. The electrostatic/gravitational pressure balance therefore must play a much more prominent role in the matching algorithm discussed in §4.2 compared to the matching algorithm for the true EMS with point charge forcing (in which proper consideration of this particular balance may be neglected with very little error).

For larger values of l, profiles become non-physical due to self-intersection well below the forcing height. Figure 3.12(a) shows profiles computed with $l = 5$. The maximally deflected solution has tip height $h(0) = 2.54$. The tips of profiles from Fig. 3.12(a) are shown in Fig. 3.12(b). The tip curvature of the solution with $h(0) = 2.54$ is much smaller than for the maximally deflected solution of the system with $l = 1$, as can be seen by comparing the pressure terms plotted in Fig.s 3.11(a) ($l = 1$) and 3.12(c) ($l = 5$). As a result, the inner region equation (4.2.2) is a much less appropriate model for the deflection profile near the interface tip for large l.

Beyond $l \approx 3$, the bifurcation structure of the system also changes. Rather than featuring a saddle-node bifurcation, we find that $q'(h(0)) > 0$ for all $h(0) > 0$ (Fig. 3.12(d)). These bifurcation diagrams all terminate when the computed deflection profiles self-intersect. We have yet to develop an understanding of why this transition in system behavior occurs.

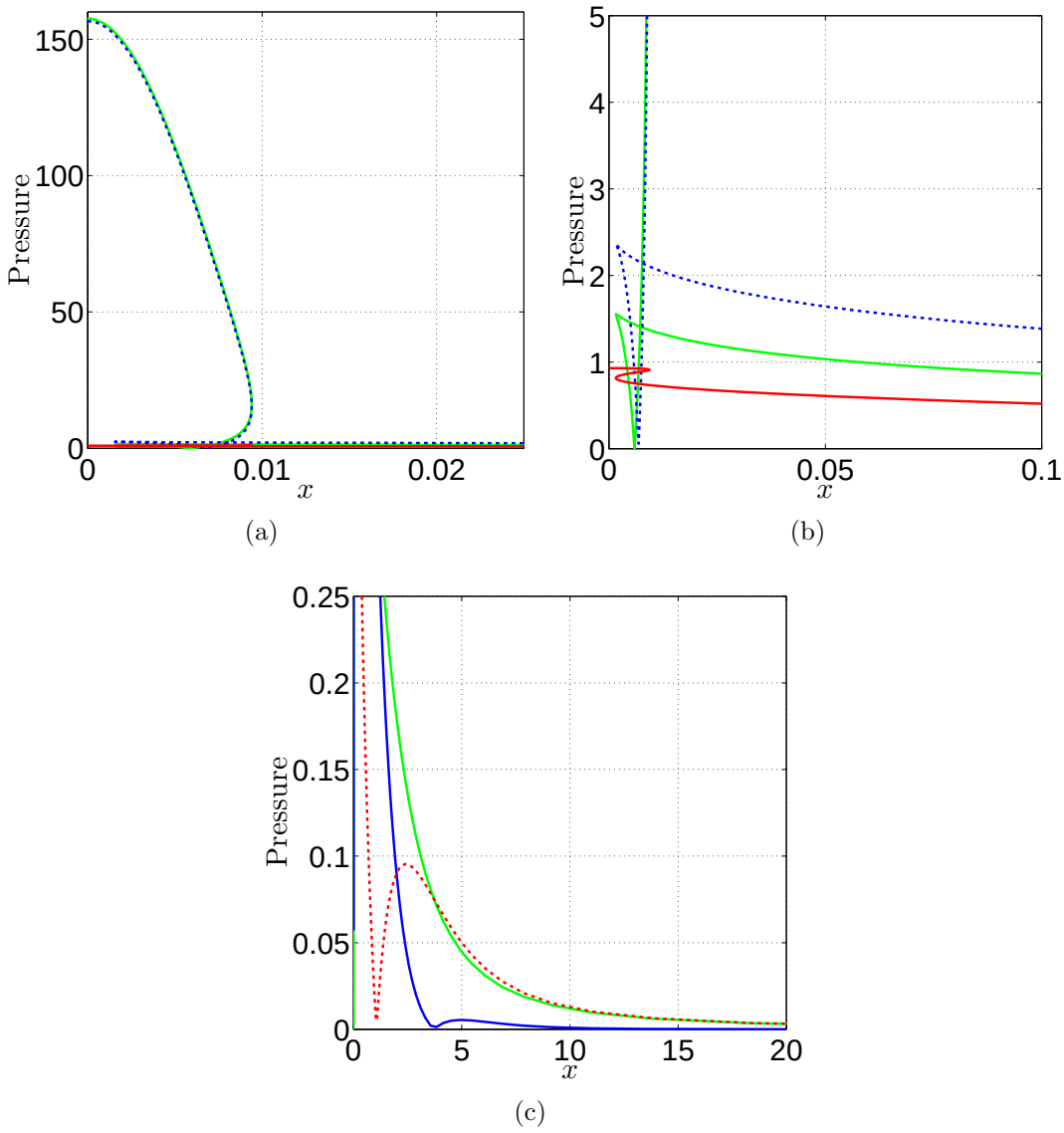

FIGURE 3.11. The magnitude of the electrostatic (green), elastic (blue) and gravitational (red) terms in (3.3.8) for the computed equilibrium deflection profile with $l = 1$ and $h(0) = 0.93$. (a) The balance near the interface tip is between elastic and electrostatic forces just as for point charge forcing. (b) An $\mathcal{O}(1)$-sized intermediate region exists in which all terms are equally important. (c) In the outer region, the dominant balance is between electrostatic and gravitational terms. The onset of this balance is at $\mathcal{O}(1)$ values of x (i.e. close to the capillary length scale), and it plays a much more significant role in determining the deflection profile than for point charge forcing.

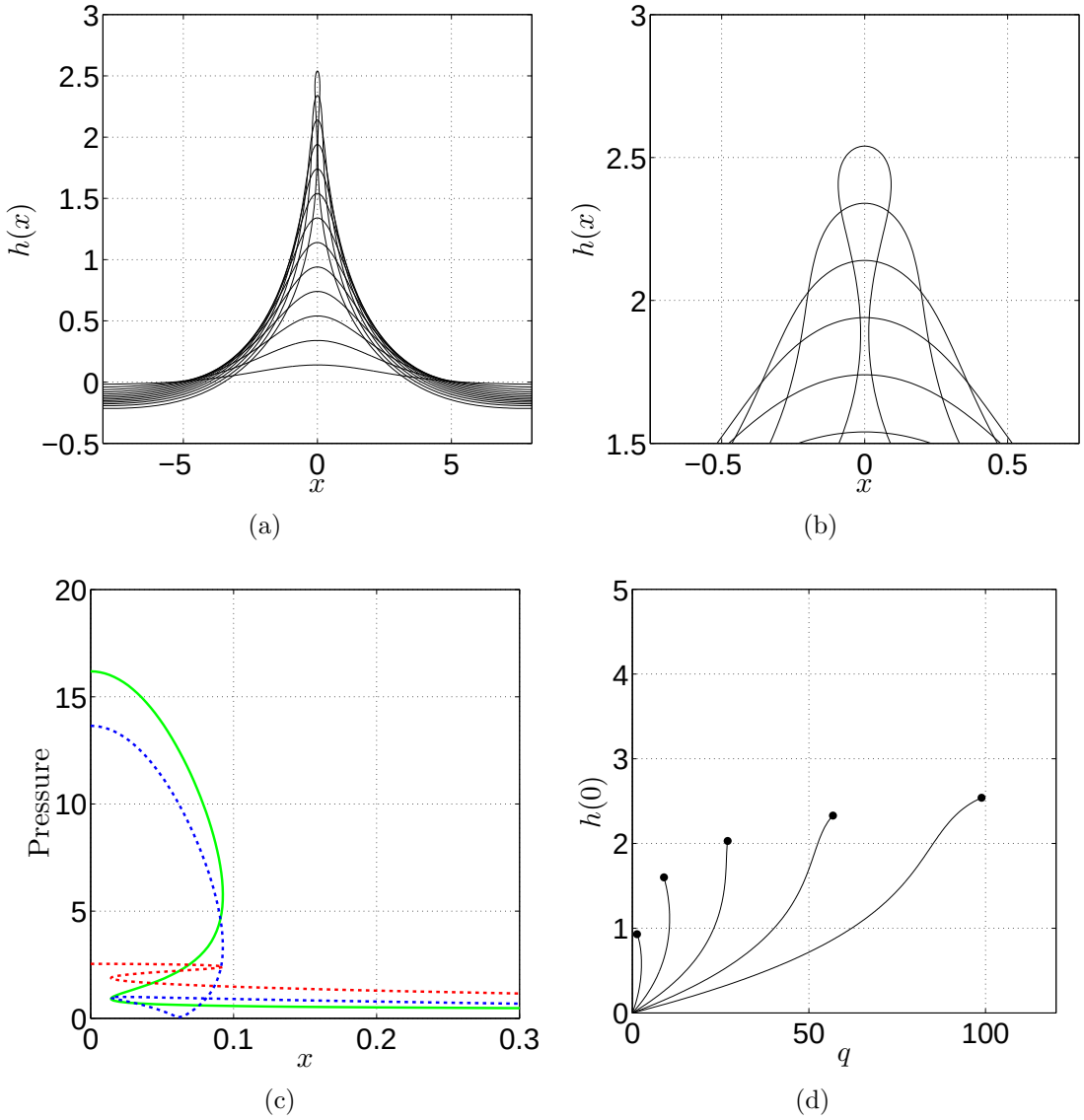

FIGURE 3.12. (a) Computed deflection profiles for $l = 1$, $M = 256$, various tip heights. The collocation method of §3.4 fails to produce profiles for any $h(0) > 2.54$. (b) Zoomed view of the profile tips from (a). (c) The magnitude of the electrostatic (green), elastic (blue) and gravitational (red) terms in (3.3.8) for the computed equilibrium deflection profile with $l = 5$ and $h(0) = 2.54$. The elastic and electrostatic terms are not as dominant as for the maximally-deflected profile computed with $l = 1$. (d) Bifurcation diagrams showing tip height $h(0)$ plotted against computed forcing strength q, $l \in \{1, 2, 3, 4, 5\}$. For $l \lessapprox 3$, all systems exhibit a saddle-node bifurcation. For $l \gtrapprox 3$, q instead increases monotonically with $h(0)$.

Chapter 4

Electrostatic Models: Matched Conformal Maps

In Chapter 3, we saw that the collocation method outlined in §3.4 fails to produce a representation of the interface deflection whenever $l - h(0)$ is sufficiently small (Fig. 3.3(b)). We will henceforth refer to such profiles as *large-deflection* profiles. Profiles of this type do not exist for l larger than some critical value (Fig. 3.9(a)). The failure of the collocation method highlights a challenging feature of the problem we are studying: large-deflection profiles feature distinct regions with very high and very low curvatures, and resolving the profile well in both regions is therefore difficult for non-adaptive numerical methods.

Near the tips of large-deflection profiles, the profile geometry is primarily controlled by a balance between the electrostatic and elastic terms only (Fig.s 3.7(a) and 3.11(a)). We will refer to the portion of the interface in which this balance remains dominant as the *inner* region. The corresponding profile is referred to as the *inner profile*. Away from the interface tip, a different balance controls the relaxation of the interface. We call this portion of the interface the *outer* region, and the profile there the *outer profile*. For the true EMS forced by a point charge, the primary balance here is between elastic and gravitational terms[1] (Fig. 3.7(b)), and the electrostatic term in (3.3.4) may be neglected. For the modified EMS forced by a dipole, the primary balance here is between elastic and electrostatic terms (Fig. 3.11(c)), and the gravitational term in (3.3.4) may be neglected. Outer profiles may be viewed as leading order approximations of large-deflection profiles, and inner profiles as next order corrections to the tip shapes of these leading order approximations.

[1] We also noted the existence of an 'outer outer' region in which the electrostatic and elastic terms dominate, but $h \ll h(0)$ in this region so we ignore it in this chapter with minimal error.

In the present chapter, we exploit the separation of large-deflection profiles into inner and outer regions to develop an efficient numerical method for calculating them. Conformal-mapping based representations of the interface deflection in each of the inner and outer regions are computed based on the dominant pressure-balances in each, and then matched together by requiring that the two profiles, as well as their parametrizations (recall that map parametrization is related to induced charge density/electrostatic pressure), agree in an intermediate region. Matching deflection profiles alone would ignore the relationship between the global deflection profile geometry and the induced electrostatic pressure everywhere along the interface, and is therefore completely physically unjustified. The classes of conformal maps from which each representation is selected are created by suitably modifying the original class of maps (3.4.2). The number of modes required to create accurate representations of the interface in each region separately (and therefore, of the entire interface once the computed representations are matched together) does not increase as the interface tip approaches the forcing charge height, a significant gain in both efficiency and simplicity when compared to the typical adaptive methods used to compute free boundaries featuring widely disparate length scales. Moreover, we will demonstrate that a single pair of computed inner and outer solutions may be used to produce a whole family of matched solutions.

In implementing the collocation method of §3.4, we argued that specifying the values of $h(0)$ and l and determining the forcing strength q as part of the numerical solution was necessary for calculating unstable interface deflections. For the matched solutions of §4.1, we shall see that specifying the leading order tip height $h_0(0)$ (or equivalently, the tip corner angle of the leading order profile) and the tip-charge separation $\varepsilon = l_1 - h_1(0)$ of the first order corrected interface allows the most natural formulation of the boundary conditions and matching conditions of the problem.

§4.1 contains analysis of the true electrostatic problem forced by a point charge. In §4.1.1, we consider the outer region. For this problem it is possible to compute

exact (implicit) representations of outer profiles, and the best approximation of each outer profile by a conformal map can then be calculated by minimizing the (sampled) distance between the exact and computed profiles directly. We call such maps *outer solutions*. The ODE that describes outer solutions is observed to be invariant under certain reparametrizations of $\partial\mathbb{D}$, a result of the small magnitude of the electrostatic pressure term in the outer region in this problem (refer back to (3.3.4) to observe the dependence of the electrostatic pressure at $i\mathbb{F}(e^{i\theta})$ on the parametrization $\mathbb{F}_\theta(e^{i\theta})$ there).

In §4.1.2, we describe the first of two methods for computing conformal maps that approximate inner profiles. We call these maps *inner solutions*. This idea is similar to that of Chapter 3, with the best approximating map calculated by minimizing the residual pressure along corresponding candidate inner profiles. However, since gravity is unimportant in the inner region, the residual pressure used here only includes electrostatic and elastic contributions. The ODE that describes inner solutions is found to be invariant under translations. The behavior of outer profiles near $x = 0$ is used to deduce the appropriate (angled) boundary conditions to be applied to inner profiles.

The conformal maps that represent inner and outer profiles are combined in §4.1.3 to produce approximate *matched solutions* of the full governing equation (3.3.4). Two matching conditions (based on the symmetries of the equations governing inner and outer solutions) are applied to ensure continuity of both the matched deflection profiles and the induced charge distributions along these profiles. We compare matched profiles to the largest-deflection profiles computed in Chapter 3 and find good agreement everywhere despite our neglect of the 'outer outer' region.

In §4.1.4, we describe an alternative method for calculating inner solutions. A first integral of the equation governing inner solutions is computed directly, and an iterative scheme then constructed based on the resulting first order equation.

In §4.2, we calculate conformal maps that represent inner solutions of the modified

electrostatic problem forced by a dipole and briefly discuss outer solutions of this same system. The construction of a matching algorithm analogous to that of §4.1 is yet to be completed (see Chapter 6).

4.1 Point Charge Forcing

4.1.1 Outer Solutions

We begin by studying the behavior of outer solutions of (3.3.4). Based on Fig.s 3.7(a)-3.7(b), we posit that the leading order behavior of large-deflection profiles may be well approximated everywhere by assuming that *all* of the induced charge $-q$ concentrates at the interface tip. The interface is then supported by an electrostatic point force (the strength of which we compute later in this subsection) and features a corner at $x = 0$. We let π/γ denote the outside angle of the leading order interface tip corner, so that $1/2 \leq \gamma \leq 1$ (see Fig. 4.1(b)). Inner solutions computed in §4.1.2 will provide a more subtle description of the true tip shape and induced charge distribution everywhere along the interface for any given $\varepsilon > 0$. Away from $x = 0$, the leading-order (outer) interface deflection $h_0(x)$ must decay due to the influences of elastic tension and gravity according to the equation

$$\frac{h_{0,xx}(x)}{(1 + h_{0,x}^2(x))^{3/2}} - h_0(x) = 0, \tag{4.1.1}$$

where $h_0(0)$ is given and $h_0(x) \to 0$ as $x \to \infty$. It is possible to implicitly solve this equation for any $h_0(0) \in [0, \sqrt{2}]$. We define $\delta = \sqrt{2} - h_0(0) > 0$ for future reference. The error introduced through neglecting the electrostatic pressure entirely is discussed in §4.1.3.

Integrating (4.1.1) once yields

$$\frac{1}{\sqrt{1 + h_{0,x}^2(x)}} + \frac{h_0^2(x)}{2} = 1, \tag{4.1.2}$$

where the constant term on the right hand side has been determined by applying the asymptotic boundary condition. At $x = 0$,

$$\frac{1}{\sqrt{1 + h_{0,x}^2(0)}} = 1 - \frac{h_0^2(0)}{2}$$

which can only be satisfied if $0 < h_0(0) < \sqrt{2}$, i.e. leading order profiles of the type we are seeking only exist for tip heights $h_0(0) < \sqrt{2}$. Rearranging gives

$$h_{0,x}(x) = -\frac{h_0(x)\sqrt{4 - h_0^2(x)}}{2 - h_0^2(x)}, \tag{4.1.3}$$

where the negative branch of the square root has been chosen without loss of generality (this equation now describes just the right-hand half of the leading order interface deflection ($h_{0,x} < 0$ everywhere there)). Using this expression for $h_{0,x}(0)$, we may now write

$$\gamma(h_0(0)) = \frac{\pi}{2}\left(\pi - \arctan\left(\frac{2 - h_0^2(0)}{h_0(0)\sqrt{4 - h_0^2(0)}}\right)\right)^{-1},$$

where arctan takes values in $[0, \pi/2]$. We note that for $\delta \ll 1$,

$$\gamma(\sqrt{2} - \delta) \sim \frac{\pi}{2}\left(\frac{1}{\pi - \arctan(\delta)}\right) \sim \frac{1}{2} + \frac{\delta}{2\pi} + \mathcal{O}(\delta^2).$$

As $\delta \to 0$, $\gamma \to 1/2$, i.e. the leading order profile approaches a cusp as $h_0(0) \to \sqrt{2}$.

Inverting the derivative in (4.1.3), we may integrate once more:

$$\frac{dx}{dh_0} = -\frac{2 - h_0^2}{h_0\sqrt{4 - h_0^2}} \quad \Rightarrow \quad x(h_0) = \int_{h_0(0)}^{h_0}\left[-\frac{2 - t^2}{t\sqrt{4 - t^2}}\right]dt.$$

This choice of lower limit ensures that the boundary condition $x(h_0(0)) = 0$ is satis-

fied. Substituting $u = \sqrt{4-t^2}$ leads to

$$\begin{aligned} x(h_0) &= \int_{\sqrt{4-h_0^2(0)}}^{\sqrt{4-h_0^2}} \left[\frac{1}{2}\left(\frac{1}{2-u}+\frac{1}{2+u}\right)-1\right] du \\ &= \left[\frac{1}{2}\left(-\log(2-u)+\log(2+u)\right)-u\right]_{\sqrt{4-h_0^2(0)}}^{\sqrt{4-h_0^2}} \\ &= \left[-\frac{1}{2}\log\left(\frac{4-u^2}{(2+u)^2}\right)-u\right]_{\sqrt{4-h_0^2(0)}}^{\sqrt{4-h_0^2}} \\ &= \log\left(\frac{2+\sqrt{4-h_0^2}}{2+\sqrt{4-h_0^2(0)}}\right) - \log\left(\frac{h_0}{h_0(0)}\right) + \sqrt{4-h_0^2(0)} - \sqrt{4-h_0^2}. \end{aligned}$$

This particular grouping of the logarithmic terms makes it clear that $h_0(x) \sim h_0(0)e^{-x}$ for $x \gg 0$. The exponential decay of both h_0 and $h_{0,xx}$ for large x implied by this solution confirms that the electrostatic pressure must eventually become a significant term in the governing force balance again. Beyond this point, the dominant force balance will be between gravitational and electrostatic forces. However, we know from Fig.s 3.7(a) and 3.7(b) that this crossover point occurs very far from the tip and for very small values of h - we therefore treat the governing equation (4.1.2) as accurate for all large x, accepting that inaccuracies in computed profiles created by ignoring electrostatic pressure there are very slight.

Fig. 4.1(a) shows exact outer deflection profiles for two $h_0(0)$-values. The corresponding full deflection profiles from Fig. 3.3(a) are overlaid. The agreement between the computed and leading order profiles is excellent away from the interface tip as expected. The size of the region in which the approximation is poor increases with ε.

The leading order forcing strength q_0 required to support the large-deflection profiles computed above depends on the leading order tip height $h_0(0)$ and the leading order charge location l_0. The total electrostatic force supporting the interface tip has magnitude $q^2/2\pi\varepsilon$, and in equilibrium this must balance the net downward force of magnitude $-2h_{0,x}(0)/\sqrt{1+h_{0,x}^2(0)}$ due to elastic tension. Using (4.1.3) to re-express the latter force in terms of $h_0(0)$, this force balance yields the following relationship

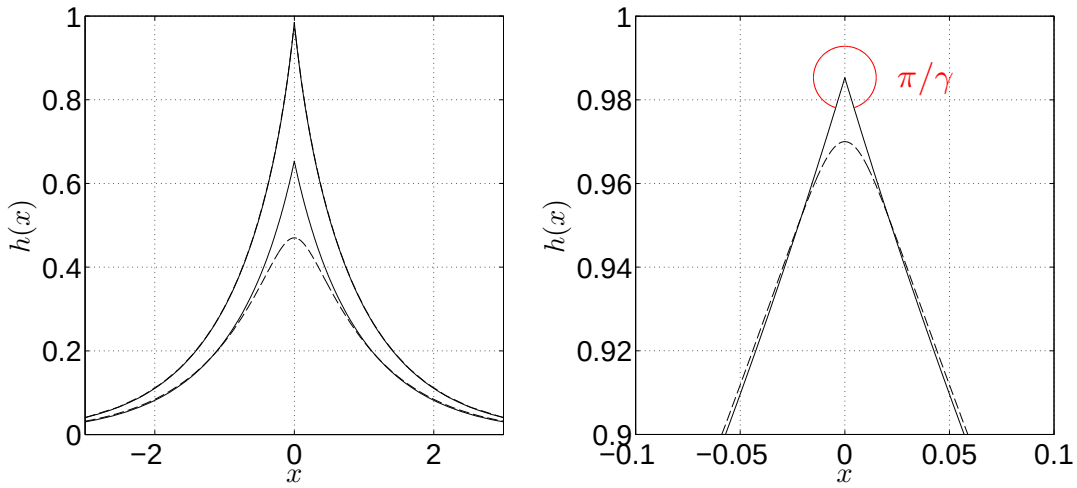

FIGURE 4.1. (a) Leading order large deflection profiles ($h_0(0) = 0.99$, $h_0(0) = 0.65$, solid curves) corresponding to computed interfaces from Fig. 3.3(a) ($h(0) = 0.96$. $h(0) = 0.5$, dashed curves). (b) Zoomed view of 4.1(a). The width of the region in which the leading order large deflection approximation is inaccurate approaches zero as $\varepsilon \to 0$. The outer tip angle π/γ is marked in red.

between q_0 and $h_0(0)$:

$$q_0 = \sqrt{2\pi\varepsilon h_0(0)\sqrt{4 - h_0(0)^2}}. \tag{4.1.4}$$

Note in particular that $q \sim C\sqrt{\varepsilon}$ as $\varepsilon \to 0$. This will inform scaling choices in §4.1.2. While the leading order profiles that produce (4.1.4) were derived under the assumption that $\varepsilon \ll 1$, the calculated formula can be evaluated for any $0 < h_0(0) < l_0$. Fig. 4.2 compares the bifurcation diagrams corresponding to (4.1.4) with the computed bifurcation diagrams of Fig. 3.3(b) for various $l_0 < \sqrt{2}$. As expected, the curves provide a consistent extension of the computed bifurcation diagrams in the asymptotic regime $\varepsilon \ll 1$. While not quantitatively accurate for $\varepsilon \sim \mathcal{O}(l_0)$, the leading order solutions capture the saddle-node bifurcation structure of the full system.

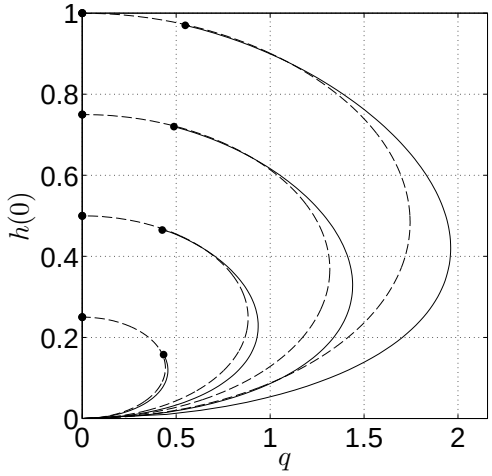

FIGURE 4.2. The bifurcation diagrams of Fig. 3.3(b) (solid curves) compared to diagrams based on leading order large deflection profiles (dashed curves) with $l_0 \in \{0.25, 0.5, 0.75, 1\}$. The leading order diagrams provide consistent extensions of the computed bifurcation diagrams to small-ε solutions, as well as capturing the overall saddle-node bifurcation structure of the system. Unsurprisingly, the accuracy is generally poor when ε is $\mathcal{O}(l_0)$.

Conformal map representation

Assume we begin with a map $\mathbb{G}(w)$ of the form (3.4.2), with relabeled parameter values $\mathbb{A} = a$, $\mathbb{B}_n = b_n$, $M = M_{out}$, $N = N_{out}$. We define the conformal map g by

$$g(w) = \frac{(\mathbb{G}(w) - \mathbb{G}(1))^{1/\gamma}}{((\mathbb{G}(w) - \mathbb{G}(1)) - t)^{1/\gamma - 1}} + h_0(0) \tag{4.1.5}$$

where $t < 0$ is an arbitrary parameter marking the end of the branch cut that creates the sharp outer solution interface tip, and let $\xi(\psi) = ig(e^{i\psi})$ for $\psi \in [-\pi, \pi)$. $g(w)$ incorporates three transformations applied to the curve $\{\mathbb{G}(e^{i\psi}) : \psi \in (-\pi, \pi]\}$:

- shifts the curve left so that the tip moves from $\mathbb{G}(1)$ to 0;
- folds the resulting curve by the appropriate angle at the tip, while ensuring that the curve still approaches a vertical asymptote as $\psi \to \pm\pi$;
- shifts the curve right so that the tip height now matches the given value $h_0(0)$.

Schematic diagrams showing the effects of the maps $\mathbb{G}$ and g and the locations of the pertinent branch cuts are given in Fig.s 4.3(a), 4.3(b) and 4.3(c). The branch cut in the preimage plane (Fig. 4.3(a)) touches $\partial\mathbb{D}$ at $w = 1$, and extends to $w_0 > 1$ such that $\mathbb{G}(w_0) = \mathbb{G}(1) + t$. Importantly, it lies entirely outside the unit circle, so the mapping g remains conformal on $\mathbb{D}$. In the intermediate plane, the profile $\{\mathbb{G}(e^{i\psi}) : \psi \in (-\pi, \pi)\}$ (Fig. 4.3(b)) features a smooth tip. The branch cut here extends from $\mathbb{G}(1)$ to $\mathbb{G}(1) + t$. The branch point at $\mathbb{G}(1)$ creates a corner at the tip of the image profile $\{g(e^{i\psi}) : \psi \in (-\pi, \pi)\}$. Because the branch cut in the intermediate plane does not extend all the way to infinity, the image profile is still asymptotically flat.

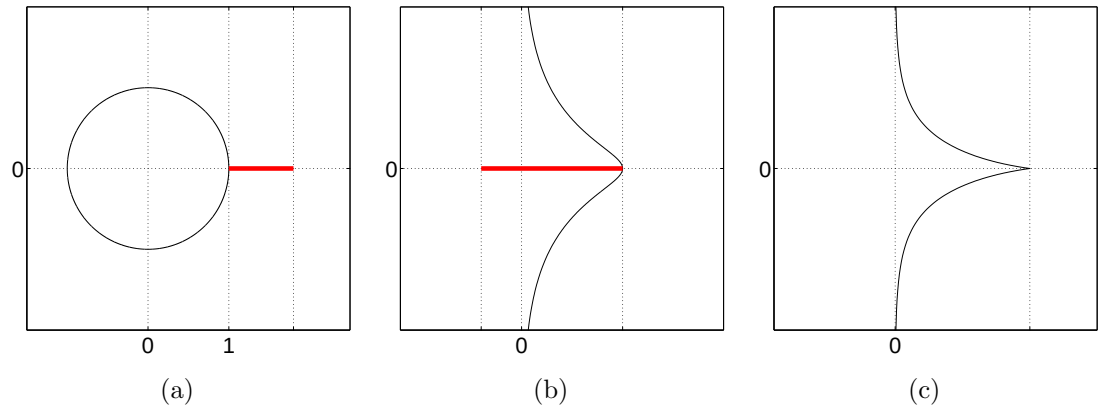

FIGURE 4.3. (a) Preimage (w) plane showing the location of the branch cut in (4.1.5). (b) Intermediate plane showing the branch cut location with respect to the profile $\{\mathbb{G}(e^{i\psi}) : \psi \in (-\pi, \pi)\}$. (c) The resulting image profile $\{g(e^{i\psi}) : \psi \in (-\pi, \pi)\}$, a candidate outer solution featuring appropriate tip profile and decay.

The parametrization with respect to ψ, rather than θ, foreshadows the need to reparametrize outer solutions - a critical part of the matching algorithm described in the upcoming §4.1.3.

We claim that the coefficients of $\mathbb{G}$ must satisfy two equations:

$$\mathrm{Re}\left(\lim_{\psi\to\pm\pi}\mathbb{G}(e^{i\psi})\right) = \sum_{n=0}^{M_{out}}(-1)^n b_n = 0, \tag{4.1.6a}$$

$$\mathbb{G}(1) = \sum_{n=0}^{M_{out}} b_n = h(0) + \left(\frac{1}{\gamma} - 1\right) t. \tag{4.1.6b}$$

It is clear that $g(1) = h(0)$, so that the tip of the interface is already fixed in the correct location. (4.1.6a) is arbitrarily specified without loss of generality, since g as defined in (4.1.5) is unaltered by the addition of any constant to $\mathbb{G}$. To understand the effects of condition (4.1.6b), we must study the asymptotic behavior of $\xi(\psi)$.

By definition,

$$\begin{aligned}
\xi(\psi) &= \frac{i\left(a\left(\frac{1-e^{i\psi}}{1+e^{i\psi}}\right) + \left(\sum_{n=0}^{M_{out}} b_n e^{in\psi} - \mathbb{G}(1)\right)\right)^{1/\gamma}}{\left(a\left(\frac{1-e^{i\psi}}{1+e^{i\psi}}\right) + \left(\sum_{n=0}^{M_{out}} b_n e^{in\psi} - \mathbb{G}(1)\right) - t\right)^{1/\gamma-1}} + ih(0), \\
&= \frac{i\left(-ia\tan(\psi/2) + \left(\sum_{n=0}^{M_{out}} b_n e^{in\psi} - \mathbb{G}(1)\right)\right)^{1/\gamma}}{\left(-ia\tan(\psi/2) + \left(\sum_{n=0}^{M_{out}} b_n e^{in\psi} - \mathbb{G}(1)\right) - t\right)^{1/\gamma-1}} + ih(0).
\end{aligned}$$

Let $s(\psi) = a\tan(\psi/2)$. Then we may re-express ξ in terms of s:

$$\widehat{\xi}(s) = \frac{i\left(-is + d(s)\right)^{1/\gamma}}{\left(-is + d(s) - t\right)^{1/\gamma-1}} + ih(0).$$

As $\psi \to \pi$ $(s \to \infty)$,

$$\begin{aligned}
\widehat{\xi}(s) &= \frac{s\left(1 + \frac{id(s)}{s}\right)^{1/\gamma}}{\left(1 + \frac{i(d(s)-t)}{s}\right)^{1/\gamma-1}} + ih(0), \\
&\sim s + i\left(\frac{d(s)}{\gamma} - (d(s) - t)\left(\frac{1}{\gamma} - 1\right)\right) + ih(0) + \mathcal{O}(s^{-1}), \\
&\sim s + id(s) + i\left(\frac{1}{\gamma} - 1\right)t + ih(0) + \mathcal{O}(s^{-1}).
\end{aligned}$$

To ascertain the dominant behavior of the second term, note that

$$s = ia\left(\frac{1 - e^{i\psi}}{1 + e^{i\psi}}\right) \Rightarrow e^{i\psi} = \frac{a + is}{a - is}.$$

Substituting gives

$$\begin{aligned}
d(s) &= \sum_{n=0}^{M_{out}} b_n \left(\frac{a + is}{a - is}\right)^n - \mathbb{G}(1), \\
&\sim -\mathbb{G}(1) + \mathcal{O}(s^{-1})
\end{aligned}$$

(having applied (4.1.6a)), so that

$$\widehat{\xi}(s) \sim s - i\left(\mathbb{G}(1) + \left(\frac{1}{\gamma} - 1\right)t + h(0)\right) + \mathcal{O}(s^{-1}).$$

Condition (4.1.6b) is therefore equivalent to requiring that the deflection of the outer region profile decays to zero as $|\psi| \to \pi$.

To confirm that we obtain the correct interface tip corner angle via this map, we may expand $\widehat{\xi}(s)$ near $s = 0$. We find that

$$d(s) \sim \frac{2is}{a}\sum_{n=0}^{M_{out}} nb_n + \mathcal{O}(s^2),$$

and consequently that

$$\widehat{\xi}(s) \sim ih(0) + \frac{e^{i(\pi/2-\pi/2\gamma)}s^{1/\gamma}\left(1 - \frac{2}{a}\sum_{n=0}^{M_{out}} nb_n\right)}{(-t)^{1/\gamma-1}} + \mathcal{O}(s^{1/\gamma+1}). \tag{4.1.7}$$

We see that the interface argument is $\pi/2 - \pi/2\gamma$ near $s = 0$ as desired.

Invariance of outer solutions under automorphisms of the unit circle

The governing equation (4.1.1) can be recast as

$$\frac{\mathrm{Im}(f_{\theta\theta}(e^{i\theta})\overline{f_\theta}(e^{i\theta}))}{|f_\theta(e^{i\theta})|^3} - \mathrm{Re}(f(e^{i\theta})) = 0. \tag{4.1.8}$$

In the previous subsection, we showed how to construct solutions of (4.1.8) for a given leading order interface tip height. It is intuitively clear that solutions of (4.1.8) are independent of the parametrization of the profile $\xi(\theta)$, since both included terms depend only on the interface *shape* (curvature and height), and electrostatic pressure (a term that most definitely is linked to the interface parametrization) is neglected everywhere. This symmetry of outer solutions and its interpretation in terms of induced charge density will be leveraged to ensure that charge density varies continuously along full deflection profiles when constructing matched solutions of (3.3.4).

We now formalize the outlined claims.

Definition 4.1.1. A *conformal automorphism* of the unit disk $\mathbb{D}$ is a bijective conformal map from $\mathbb{D}$ to itself. (The family of all such maps on $\mathbb{D}$ may be identified with the class of schlict functions.)

Since we are clearly interested only in conformal maps, we will assume the conformal prefix in all following discussion.

Theorem 4.1.2. All automorphisms of $\mathbb{D}$ have the form

$$\mathcal{A}_{\alpha,\theta_0}(w) = e^{i\theta_0}\mathcal{A}_\alpha(w) = e^{i\theta_0}\left(\frac{w-\alpha}{1-\overline{\alpha}w}\right). \tag{4.1.9}$$

for some $\theta_0 \in [-\pi, \pi)$, $\alpha \in \mathbb{D}$.

We rely on some elements of the Schwarz lemma in the proof of this claim:

Lemma 4.1.3. (Schwarz) Let $f : \mathbb{D} \to \mathbb{D}$ be analytic with $f(0) = 0$. Then:

(i) $|f(w)| \leq |w|$ for all $w \in \mathbb{D}$;

(ii) if $|f(w_0)| = |w_0|$ for some $w_0 \neq 0$ in $\mathbb{D}$, then f must be a rotation about 0.

Proof of Lemma 4.1.3. (i) Write $f(w) = \sum_{j=0}^{\infty} f_j w^j$. $f(0) = 0$ implies that $f_0 = 0$, and hence $f(w)/w$ is also analytic everywhere in $\mathbb{D}$.

Since $f : \mathbb{D} \to \mathbb{D}$, $|f(w)| \leq 1$ everywhere in $\mathbb{D}$. For each $0 < r < 1$, the inequality

$$\left|\frac{f(w)}{w}\right| \leq \frac{1}{r}$$

therefore holds everywhere in $\{|w| = r\}$. $f(w)/w$ is analytic, so the maximum modulus principle applies and we can extend this upper bound to $\{|w| \leq r\}$. As $r \to 1$, we recover the stated inequality.

(ii) From (i), we know that $f(w)/w \leq 1$ on $\mathbb{D}$. Since $|f(w_0)/w_0| = 1$ (and this must be at least a local maximum), the maximum modulus principle implies that $f(w)/w$ is constant on $\mathbb{D}$. But $|f(w_0)| = |w_0|$, so this constant must have modulus 1. Hence $f(w)$ is a rotation. $\square$

We can now prove the original theorem:

Proof of Theorem 4.1.2[2]. Let g be any analytic automorphism of the unit disk. There exists a unique $\alpha \in \mathbb{D}$ such that $g(\alpha) = 0$, so the composition $f = g \circ (-\mathcal{A}_\alpha)$ maps 0 to itself. By part (i) of 4.1.3, $|f(w)| \leq |w|$ for all $w \in \mathbb{D}$. It is also true that $f^{-1}(0) = 0$, so $|f^{-1}(z)| \leq |z|$ for all $z \in \mathbb{D}$. Applying this second inequality to $z = f(w)$ gives $|w| \leq |f(w)|$ for all $w \in \mathbb{D}$. This sandwiching argument implies that $|f(w)| = |w|$ everywhere in $\mathbb{D}$. Hence, by part (ii) of 4.1.3, $f(w) = e^{i\theta}w$ for some $\theta \in [-\pi, \pi)$. Replacing w by $(-\mathcal{A}_\alpha(w))$ and applying the easily-verified identity $((-\mathcal{A}_\alpha) \circ (-\mathcal{A}_\alpha))(w) = w$, we deduce that $g(w) = e^{i\theta_0}\mathcal{A}_\alpha(w)$ for some $\theta_0 \in [\pi, \pi)$, $\alpha \in \mathbb{D}$ as claimed. □

The conformal automorphisms of $\mathbb{D}$ form a subgroup of the group of Möbius transformations defined on $\mathbb{D}$. We care particularly about a further subgroup of conformal automorphisms that fix 1 and -1 (these preserve the symmetry of deflection profiles). Applying these conditions to the conformal automorphisms described by Theorem 4.1.2 implies that θ_0 and α must satisfy the equations

$$e^{i\theta_0}\left(\frac{1-\alpha}{1-\overline{\alpha}}\right) = 1,$$
$$-e^{i\theta_0}\left(\frac{1+\alpha}{1+\overline{\alpha}}\right) = -1.$$

Eliminating θ_0 leads to the consistency condition $\mathrm{Im}(\alpha) = 0$, which in turn forces $e^{i\theta_0} = 1$. So for our purposes, it is enough to consider the one-parameter family of automorphisms

$$\mathcal{A}_\alpha(w) = \frac{w-\alpha}{1-\alpha w},\ \alpha \in (-1, 1). \tag{4.1.10}$$

for $\alpha \in \mathbb{R}$. These maps (in fact all automorphisms of $\mathbb{D}$) send the unit circle to itself:

$$\left|\frac{e^{i\theta}-\alpha}{1-\alpha e^{i\theta}}\right| = \left|\frac{e^{i\theta}-\alpha}{e^{-i\theta}-\alpha}\right| = \left|\frac{e^{i\theta}-\alpha}{\overline{e^{i\theta}-\alpha}}\right| = 1.$$

Thus, $\mathcal{A}_\alpha(e^{i\theta}) = e^{i\psi_\alpha}$ for some function $\psi_\alpha = \psi_\alpha(\theta)$ defined on $[-\pi, \pi)$. Determining ψ_α directly from the definition of $\mathcal{A}_\alpha$ is not straightforward. The comparison becomes

easier if we first map $\mathbb{D}$ to the right half plane $\mathcal{R}$ - the unit circle maps to the imaginary axis and all scaling along the boundary $\partial\mathcal{R}$ will be with respect to modulus, rather than argument.

Let $z = R(w) = (1-w)/(1+w)$. In particular, note that $R(e^{i\theta}) = -i\tan(\theta/2)$. A short calculation shows that

$$R(\mathcal{A}_\alpha(e^{i\theta})) = \frac{(1+\alpha)}{(1-\alpha)} R(e^{i\theta}), \tag{4.1.11}$$

i.e. the family of automorphisms (4.1.10) of $\mathbb{D}$ corresponds to the family of automorphisms

$$\mathcal{B}_\beta(z) = \beta z,\ \beta \in (0,\infty)$$

of $\mathcal{R}$. Applying R^{-1} to both sides of (4.1.11), where $R^{-1}(0+iy) = -2\tan^{-1}(y)$, gives

$$\psi_\alpha(\theta) = 2\tan^{-1}(\beta(\alpha)\tan(\theta/2)) \tag{4.1.12}$$

for $\beta(\alpha) = (1+\alpha)/(1-\alpha) \in (0,\infty)$. This alternative characterization of suitable automorphisms of $\mathbb{D}$ is useful when explicitly checking the following:

Claim 4.1.13. *Let $f(e^{i\theta})$ solve (4.1.8), and define g by $g(e^{i\theta}) = f(e^{i\psi(\theta)})$ for ψ any map of the form (4.1.12). Then $g(e^{i\theta})$ also satisfies (4.1.8).*

Proof of Claim 4.1.13. $g_\theta(e^{i\theta}) = f_\psi(e^{i\psi})\psi_\theta(\theta)$, and $g_{\theta\theta}(e^{i\theta}) = f_{\psi\psi}(e^{i\psi})\psi_\theta^2(\theta) + f_\psi(e^{i\psi})\psi_{\theta\theta}(\theta)$. The derivatives of ψ are all real-valued. So

$$\frac{\mathrm{Im}(g_{\theta\theta}(e^{i\theta})\overline{g_\theta}(e^{i\theta}))}{|g_\theta(e^{i\theta})|^3} = \frac{\mathrm{Im}\left(\left[f_{\psi\psi}(e^{i\psi})\psi_\theta^2(\theta) + f_\psi(e^{i\psi})\psi_{\theta\theta}(\theta)\right]\overline{f_\psi}(e^{i\psi})\psi_\theta(\theta)\right)}{|f_\psi(e^{i\psi})|^3|\psi_\theta(\theta)|^3} \tag{4.1.14}$$

$$= \frac{\phi_\theta^3(\theta)}{|\phi_\theta(\theta)|^3}\frac{\mathrm{Im}\left(f_{\psi\psi}(e^{i\psi})\overline{f_\psi}(e^{i\psi})\right)}{|f_\psi(e^{i\psi})|^3} + \frac{\phi_{\theta\theta}(\theta)\phi_\theta(\theta)}{|\phi_\theta(\theta)|^3}\frac{\mathrm{Im}\left(|f_\psi(e^{i\psi})|^2\right)}{|f_\psi(e^{i\psi})|^3} \tag{4.1.15}$$

$$= \mathrm{sign}(\phi_\theta(\theta))\frac{\mathrm{Im}\left(f_{\psi\psi}(e^{i\psi})\overline{f_\psi}(e^{i\psi})\right)}{|f_\psi(e^{i\psi})|^3} \tag{4.1.16}$$

$$= \frac{\mathrm{Im}\left(f_{\psi\psi}(e^{i\psi})\overline{f_\psi}(e^{i\psi})\right)}{|f_\psi(e^{i\psi})|^3} \tag{4.1.17}$$

($\text{sign}(\phi_\theta(\theta)) = 1$ for all θ, since tan and $\tan^{-1}$ are increasing functions on $(-\pi, \pi)$ and $(-\infty, \infty)$ respectively).

It is also obvious that

$$\text{Re}(g(e^{i\theta})) = \text{Re}(f(e^{i\psi})) \tag{4.1.18}$$

by definition. Hence

$$\frac{\text{Im}(g_{\theta\theta}(e^{i\theta})\overline{g_\theta}(e^{i\theta}))}{|g_\theta(e^{i\theta})|^3} - \text{Re}(g(e^{i\theta})) = \frac{\text{Im}(f_{\psi\psi}(e^{i\psi})\overline{f_\psi}(e^{i\psi}))}{|f_\psi(e^{i\psi})|^3} - \text{Re}(f(e^{i\psi})) = 0, \tag{4.1.19}$$

i.e. $f(e^{i\psi(\theta)})$ satisfies (4.1.8) whenever $f(e^{i\theta})$ does. □

4.1.2 Inner Solutions, Collocation Method

We argued in the introduction of this chapter that the concentration of induced charge near the tip of large-deflection profiles implies the existence of an inner region in which electrostatic pressure balances elastic tension and the influence of gravity is relatively unimportant. In this section, we formally derive the equation governing inner solutions and construct conformal maps to represent these solutions. As for outer solutions, we modify the original class of maps (3.4.2) to create candidate solutions. In the absence of an explicit representation of inner solutions, we compute the best fit inner solution by minimizing the residual pressure measured at discrete points along the sheet (exactly as we did for full solutions).

Conformal map representation

Let $\mathbb{F} = \varepsilon F$ (equivalent to scaling both x and y in the image plane) and $q = \sqrt{\varepsilon}Q$ (this scaling of the forcing strength was noted in the analysis of leading-order large-deflection profiles, see §4.1.1). Then (3.3.4) becomes

$$\frac{\text{Im}(F_{\theta\theta}(e^{i\theta})\overline{F_\theta}(e^{i\theta}))}{|F_\theta(e^{i\theta})|^3} - \varepsilon^2\text{Re}(F(e^{i\theta})) = -\frac{Q^2}{4\pi^2|F_\theta(e^{i\theta})|^2}. \tag{4.1.20}$$

Under the assumption that ε is small, we may neglect the second term in the inner region as long as F and Q remain $\mathcal{O}(1)$, so that

$$\frac{\mathrm{Im}(F_{\theta\theta}(e^{i\theta})\overline{F_\theta}(e^{i\theta}))}{|F_\theta(e^{i\theta})|^3} = -\frac{Q^2}{4\pi^2|F_\theta(e^{i\theta})|^2}. \tag{4.1.21}$$

The associated boundary conditions are

$$F(0) - F(1) = 1, \tag{4.1.22a}$$

$$F(e^{i\theta}) \sim C_{\text{asy}} + (e^{\pm i\pi/2} A \tan(\theta/2))^{1/\gamma} + o(1) \text{ as } \theta \to \mp\pi, \tag{4.1.22b}$$

where C_{asy} and A are constants whose values are determined as part of the numerical solution. We refer to C_{asy} as the 'asymptotic offset' of a computed solution. (4.1.22a) ensures that the tip-charge separation distance is ε in the physical plane, while (4.1.22b) ensures that the asymptotic behaviors of inner solution profiles agree with the tip shapes of corresponding outer solutions (for a specified value of γ).

Note that if F satisfies (4.1.21) and the boundary conditions (4.1.22), then $F + c$ will satisfy the same equations for any $c \in \mathbb{R}$ (with $C_{\text{asy}} \to C_{\text{asy}} + c$). When computing numerical solutions, this redundancy is removed by specifying a third (artificial) boundary condition[3]:

$$F(1) = (1 + T) \text{ for some } T > -1. \tag{4.1.22c}$$

The asymptotic offset C_{asy} is related to T by the equation

$$C_{\text{asy}} = T + k \tag{4.1.23}$$

for some constant k depending on γ only.

Assume we begin with a map $\mathbb{G}(w)$ of the form (3.4.2), with relabeled parameter values $\mathbb{A} = A$, $\mathbb{B}_n = B_n$, $M = M_{in}$, $N = N_{in}$. We define the conformal map G by

$$G(w) = \left(\mathbb{G}(w) + B_{M_{in}} \left(\frac{1+w}{2} \right)^{1/\gamma - 1} \right)^{1/\gamma}, \tag{4.1.24}$$

[3]The restriction on T is necessary to ensure the maps produced are still conformal above the sheet.

and write $\Xi(\theta) = iG(e^{i\theta})$ for $\theta \in [-\pi, \pi)$. $G(w)$ incorporates two transformations applied to the curve $\{\mathbb{G}(e^{i\theta}) : \psi \in (-\pi, \pi]\}$:

- adds a new term that decays as $w \to -1$ (with coefficient $B_{M_{in}}$) to allow for the appropriate decay towards asymptotically angled lines (more explanation of this claimed behavior is provided shortly);
- folds the resulting curve by the appropriate angle far away, while ensuring that the tip profile is still smooth (as long as $T > -1$).

Fig.s 4.4(a), 4.4(b), and 4.4(c) show the location of the branch cut in the preimage (Fig. 4.4(a)) and intermediate (Fig. 4.4(b)) planes, and an example of the candidate inner solutions produced (Fig. 4.4(c)). We will see in the following calculations that without the additional term added to $\mathbb{G}(w)$ in (4.1.24), it would be impossible to construct a solution that asymptotically approaches straight lines. This in turn is a result of the requirement that the branch cut must remain outside the unit disk in the preimage plane for $G(w)$ to remain conformal.

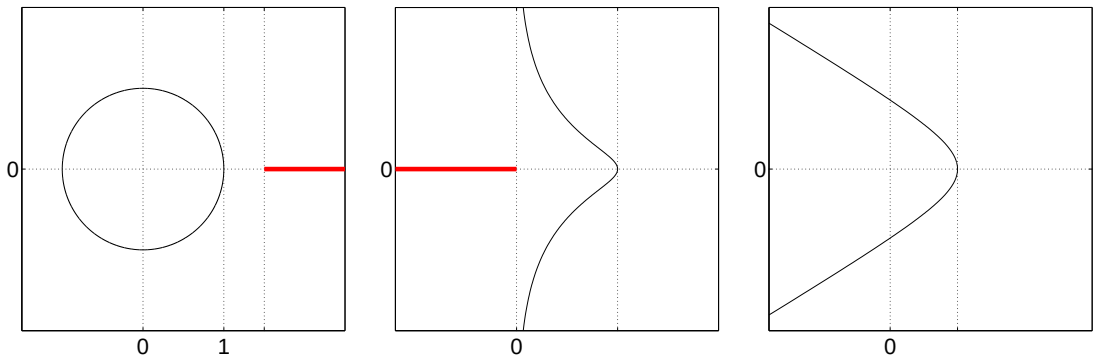

FIGURE 4.4. (a) Preimage (w) plane showing the location of the branch cut in (4.1.24). The branch cut extends to $+\infty$. (b) Intermediate plane showing the branch cut location with respect to the profile $\{\mathbb{G}(e^{i\theta}) : \theta \in (-\pi, \pi)\}$. The branch cut extends to $-\infty$. (c) The resulting image profile $\{G(e^{i\theta}) : \theta \in (-\pi, \pi)\}$, a candidate inner solution featuring appropriately angled asymptotes.

We claim that the coefficients of $\mathbb{G}$ must satisfy three equations:

$$\mathbb{G}(0) = A + B_0 + \frac{B_{M_{in}}}{2^{1/\gamma-1}} = (2+T)^\gamma, \tag{4.1.25a}$$

$$\mathbb{G}(1) = \sum_{n=0}^{M_{in}-1} B_n + B_{M_{in}} = (1+T)^\gamma, \tag{4.1.25b}$$

$$\mathrm{Re}\left(\lim_{\theta\to\pm\pi} \mathbb{G}(e^{i\theta})\right) = \sum_{n=0}^{M_{in}-1} (-1)^n B_n = 0. \tag{4.1.25c}$$

(4.1.25a) fixes $G(0) = 2+T$ and (4.1.25b) fixes $G(1) = 1+T$, so that (4.1.25a) and (4.1.25b) together ensure that (4.1.22a) and (4.1.22c) are satisfied. To understand the effect of (4.1.25c), we must study the asymptotic behavior of $\Xi(\theta)$.

By definition,

$$\begin{aligned}\Xi(\theta) &= i\left(A\left(\frac{1-e^{i\theta}}{1+e^{i\theta}}\right) + \sum_{n=0}^{M_{in}-1} B_n e^{in\theta} + B_{M_{in}}\left(\frac{1+e^{i\theta}}{2}\right)^{1/\gamma-1}\right)^{1/\gamma}, \\ &= i\left(-iA\tan(\theta/2) + \sum_{n=0}^{M_{in}-1} B_n e^{in\theta} + B_{M_{in}}\left(\frac{1+e^{i\theta}}{2}\right)^{1/\gamma-1}\right)^{1/\gamma}.\end{aligned} \tag{4.1.26}$$

Let $S(\theta) = A\tan(\theta/2)$. Then we may re-express Ξ in terms of S:

$$\widehat{\Xi}(S) = i\left(-iS + D_1(S) + D_2(S)\right)^{1/\gamma},$$

where D_1 and D_2 represent the second and third terms in (4.1.26). As $\theta \to \pi$ ($S \to \infty$),

$$\begin{aligned}\widehat{\Xi}(S) &= i(e^{-i\pi/2}S)^{1/\gamma}\left[1 + \frac{i(D_1(S)+D_2(S))}{S}\right]^{1/\gamma} \\ &= i\left((e^{-i\pi/2}A\tan(\theta/2))^{1/\gamma} + \frac{ie^{-i\pi/2\gamma}S^{1/\gamma-1}(D_1(S)+D_2(S))}{\gamma} + \mathcal{O}(S^{1/\gamma-2})\right).\end{aligned}$$

The first term in this expansion exactly equals the term in (4.1.22b) that represents a straight line passing through the origin with angle matching the applied boundary conditions. To ascertain the dominant behavior of the second term, note that

$$S = iA\left(\frac{1-e^{i\theta}}{1+e^{i\theta}}\right) \Rightarrow e^{i\theta} = \frac{A+iS}{A-iS}.$$

Substituting gives

$$D_1(S) = \sum_{n=0}^{M_{in}-1} B_n \left(\frac{A+iS}{A-iS}\right)^n = \sum_{n=0}^{M_{in}-1} (-1)^n B_n + \mathcal{O}(S^{-1}) = \mathcal{O}(S^{-1})$$

(by (4.1.25c)), and

$$D_2(S) = B_{M_{in}} \left(\frac{A}{A-iS}\right)^{1/\gamma-1} = \frac{-ie^{i\pi/2\gamma} B_{M_{in}} A^{1/\gamma-1}}{S^{1/\gamma-1}} + \mathcal{O}(S^{-1/\gamma})$$

Since $1 < 1/\gamma < 2$, $S^{1/\gamma-1} D_1(S) \to 0$ as $S \to \infty$. We also have that

$$\frac{ie^{-i\pi/2\gamma} S^{1/\gamma-1} D_2(S)}{\gamma} \sim \underbrace{\frac{B_{M_{in}} A^{1/\gamma-1}}{\gamma}}_{\equiv C_{\text{asy}}} + \mathcal{O}(S^{-1}),$$

so

$$\widehat{\Xi}(S) \sim \frac{iB_{M_{in}} A^{1/\gamma-1}}{\gamma} + i(e^{-i\pi/2} A \tan(\theta/2))^{1/\gamma}, \tag{4.1.27}$$

exactly matching the form (4.1.22b) with $C_{\text{asy}} = B_{M_{in}} A^{1\gamma-1}/\gamma$ (and with an extra factor of i to account for rotation to match physical coordinates).

We note that if condition (4.1.25c) is removed, $D_1(S) \sim \mathcal{O}(1)$ for $S \gg 1$. Additionally removing the corrective term $D_2(S)$ would yield the asymptotic behavior

$$\widehat{\Xi}(S) \sim ie^{-\pi/2\gamma} S^{1/\gamma} - e^{-i\pi/2\gamma} K S^{1/\gamma-1} + \ldots \tag{4.1.28}$$

for K a constant. The second term is always perpendicular to the first and increases in magnitude as $S \to \infty$. However, the rate of growth of the second term is smaller than that of the leading order term. Such growth does not prevent the argument of the inner profile from approaching $-\pi/\gamma$ as $S \to \infty$, but it cannot accommodate profiles that asymptotically approach a line of the form (4.1.22b). This is best illustrated with an example as shown in Fig. 4.5.

Computed solutions

For intermediate values of γ (not too close to 1/2) and T moderately close to -1, the algorithm for computing inner solutions produces curves with all of the desired properties (Fig. 4.6(a)). The asymptotic offset $C_{\text{asy}} = B_{M_{in}} A^{1/\gamma-1}/\gamma$ for a single computed

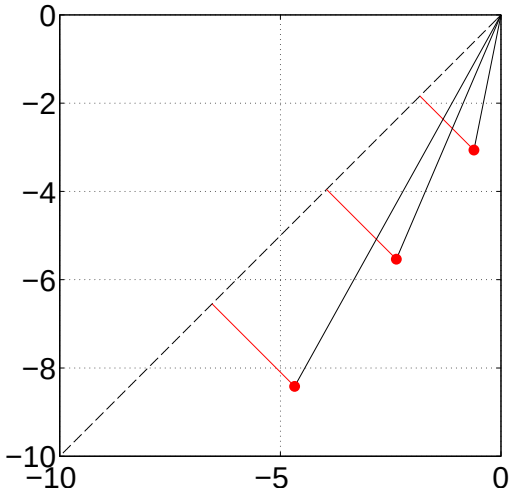

FIGURE 4.5. A sequence of points whose arguments approach that of the dashed line, but whose perpendicular distances from that same line (in red) increase (looking top to bottom). Such sequences are not compatible with the boundary condition of the form (4.1.22b) applied to inner solution profiles.

inner solution is marked in Fig. 4.6(b). However, the explicit relationship (4.1.23) between C_{asy} and T is not respected by computed solutions if T becomes either very close to -1 or larger than some *a priori* unknown threshold value (Fig. 4.6(c)). For the value of γ used in these demonstrations, the expected linear behavior is only displayed for $-0.9 < T < 0$.

As γ approaches $1/2$, a very limited range of T-values clearly display the expected linear dependence of the asymptotic offset on T. This is not surprising - the scaling we have applied in this chapter ignores the formation of a cusp at the tip of outer solutions as $l \to \sqrt{2}$ ($\delta \to 0$). Our problem is one that contains multiple (potentially) small scales, and a new scaling regime would be required to properly describe the system behavior for $\delta \ll 1$. We comment further on this topic in Chapter 6.

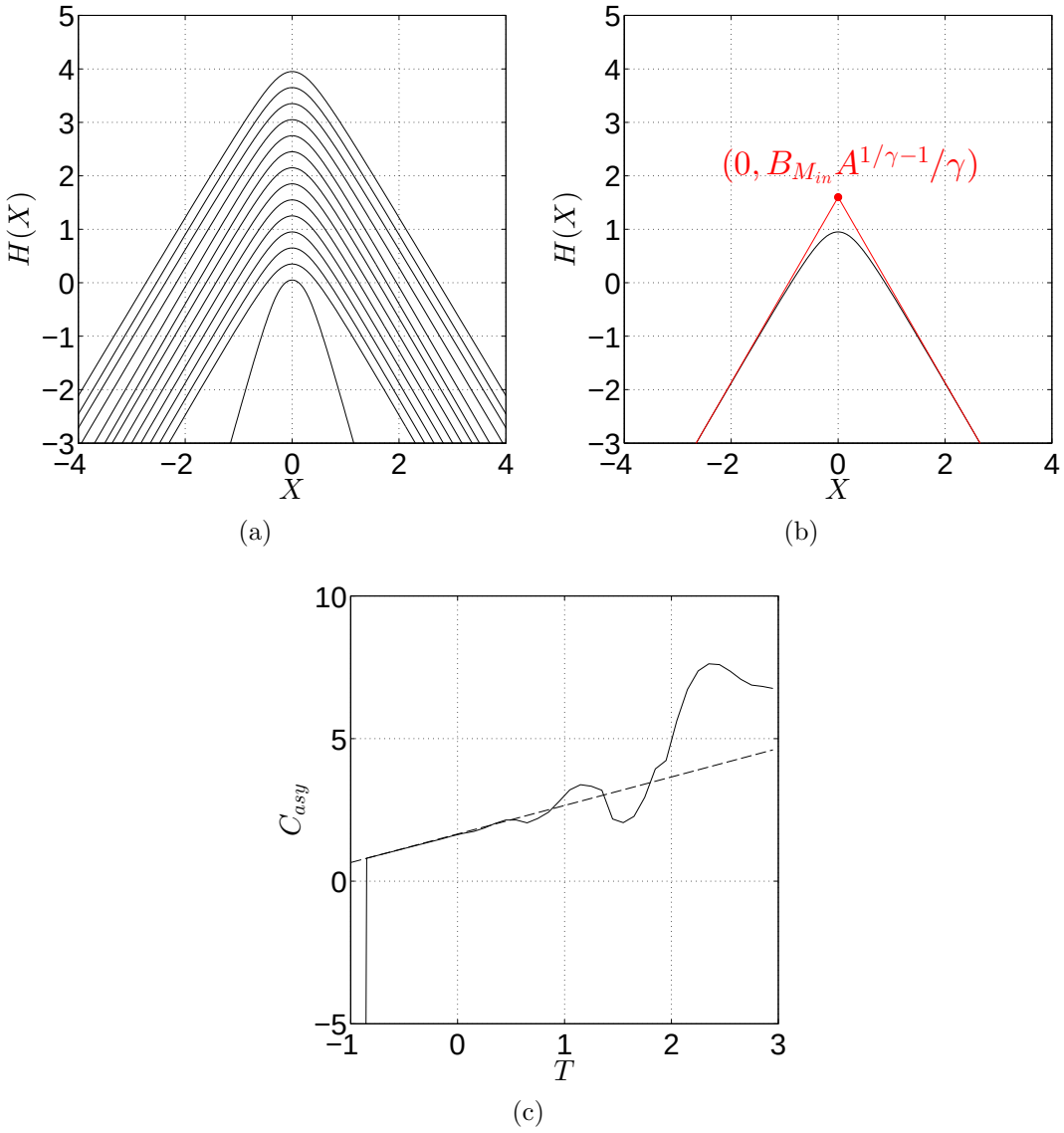

FIGURE 4.6. (a) Computed inner solution profiles for $\gamma = 0.6$, $-0.95 \leq T \leq 3$. The profile for $T = -0.95$ is clearly inaccurate; the profiles for $T \gtrapprox 0$ less obviously so. (b) A single profile from (a) with $T = -0.05$, showing the calculated asymptotic offset $C_{\text{asy}} = B_{M_{in}} A^{1/\gamma-1}/\gamma$. (c) Asymptotic offsets computed using the image node location $iF(e^{i\theta_{N_{in}-1}})$ and known asymptotic interface angle for the profiles in (a) (solid curve), plotted against T. The dashed curve shows the theoretical relationship (4.1.23).

4.1.3 Matched Solutions

Now that we can compute inner and outer solutions separately, we need to combine them to produce an approximate solution of the full system. We posit a solution of the form

$$\mathbb{G}(e^{i\theta}) = \big(\varepsilon G(e^{i\theta}) + H_0\big) + g(e^{i\psi_\alpha(\theta)}) - \mathcal{G}(e^{i\theta}) \tag{4.1.29}$$

for given values of ε and $h_0(0)$ (or γ). Here $\mathbb{G}$ is an approximate solution of (3.3.4), g is an outer solution, G is an inner solution from §4.1.2, H_0 is an $\mathcal{O}(1)$ real number (varying linearly with T) used to shift the inner solution vertically, and ψ_α is of the form (4.1.12). The functions H_0, $\mathcal{G}$ and ψ_α will be chosen to appropriately match the inner and outer solutions. $\mathbb{G}$ is necessarily a combination of conformal maps - matching profile shapes alone (the usual goal of the method of matched asymptotics) would be physically incorrect as it would fail to properly account for the non-local coupling between induced electrostatic pressure and global interface geometry.

Determining $\mathcal{G}$

$\mathcal{G}$ will be used to subtract the outer limit of the inner solution from the full solution, matching the deflection profiles in each region. The asymptotic behavior of G is of the form (4.1.22b) with $C = B_{M_{in}} A^{1/\gamma - 1}/\gamma$, so we set

$$\mathcal{G}(e^{i\theta}) = \varepsilon \left(A^{1/\gamma} \left(\frac{1 - e^{i\theta}}{1 + e^{i\theta}} \right)^{1/\gamma} + \frac{B_{M_{in}} A^{1/\gamma - 1}}{\gamma} \right) + H_0,$$

leaving

$$\mathbb{G}(e^{i\theta}) = \varepsilon \left(G(e^{i\theta}) - A^{1/\gamma} \left(\frac{1 - e^{i\theta}}{1 + e^{i\theta}} \right)^{1/\gamma} - \frac{B_{M_{in}} A^{1/\gamma - 1}}{\gamma} \right) + g(e^{i\psi_\alpha(\theta)}).$$

Determining ψ_α

To determine ψ_α, we will require that the parametrization of the outer limit of the inner equation agrees with the parametrization of the inner limit of the outer solution. Our freedom here lies entirely with the outer solution map.

We have already computed the scalings of the inner limit of the outer solution (4.1.7) and the outer limit of the inner solution (4.1.27) in terms of the 'intermediate' variables $s(\psi)$ and $S(\theta)$ respectively. Equating the highest-order terms of each representation (and multiplying the inner solution by ε to match physical variables) gives

$$\varepsilon(-iS)^{1/\gamma} = (-is)^{1/\gamma}\left(\frac{\left(1-\frac{2}{a}\sum_{n=0}^{M_{out}} nb_n\right)^{1/\gamma}}{(-t)^{1/\gamma-1}}\right),$$

or equivalently (substituting $(-iS) = iA\tan(\theta/2)$, $(-is) = ia\tan(\psi/2)$),

$$\psi(\theta) = 2\tan^{-1}(\beta\tan(\theta/2)) \text{ for } \beta = \underbrace{\left(\frac{A(-t)^{1-\gamma}}{a-2\sum_{n=0}^{M_{out}} nb_n}\right)}_{\mathcal{C}_\gamma}\varepsilon^\gamma. \tag{4.1.30}$$

We have now completely determined both of the unknown functions in (4.1.29).

Figures 4.7(a) and 4.7(b) illustrate the 'conformal' transformation (4.1.30) between the outer region angle (ψ) and the inner region angle (θ) applied when computing matched solutions of the form (4.1.29). $\mathcal{C}_\gamma$ is independent of ε, so will always be much larger than ε for ε small enough. We note that the leading order behavior of the automorphism $\mathcal{A}(w)$ corresponding to this mapping from ψ to θ is given by

$$\mathcal{A}(w) \sim \begin{cases} 1+\dfrac{w-1}{\mathcal{C}_\gamma\varepsilon^\gamma}, & |w-1| \ll 2\mathcal{C}_\gamma\varepsilon^\gamma, \\ -1-\dfrac{4\mathcal{C}_\gamma\varepsilon^\gamma}{w-1}, & |w-1| \gg 2\mathcal{C}_\gamma\varepsilon^\gamma. \end{cases}$$

Note on composite solution error

Now that we have computed the function ψ, we can estimate the error introduced by neglecting the electrostatic pressure in the outer region. The error in the composite solution (4.1.29) is bounded by the errors in the inner and outer regions as long as there exists an overlap region (i.e. a range of θ values) in which the inner and outer solutions can be made to agree exactly.

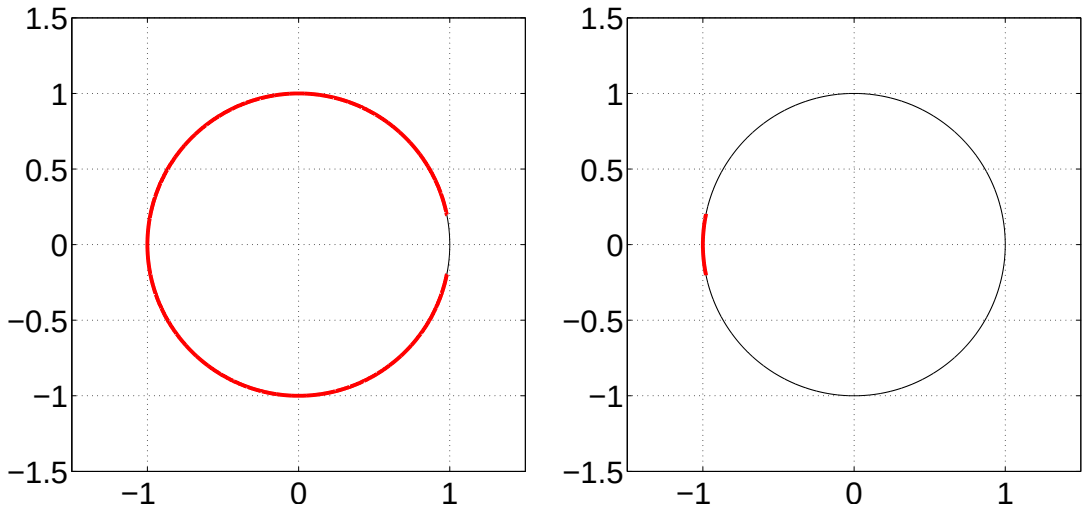

FIGURE 4.7. (a) In red: the region in which outer solutions are accurate, expressed in terms of the outer angle $\psi \in (-\pi, \pi)$. (b) The same region now expressed in terms of the inner angle $\theta \in (-\pi, \pi)$, as used for producing matched solutions of the form (4.1.29). ψ and θ are related by (4.1.30) with $\varepsilon \ll 1$.

Based on (4.1.20), it is easy to see that with the particular representation (4.1.24) of inner solutions the error in the inner region remains $\mathcal{O}(\varepsilon^\alpha)$ until

$$\varepsilon^2 \mathrm{Re}((-iA\tan(\theta/2))^{1/\gamma}) \sim \mathcal{O}(\varepsilon^\alpha),$$

i.e. until $\tan(\theta/2) \sim \mathcal{O}(\varepsilon^{\gamma(\alpha-2)})$.

Writing the outer solution $g(e^{i\psi(\theta)})$ in terms of the inner region coordinate θ and substituting into (3.3.4) gives

$$\frac{\mathrm{Im}(g_{\psi\psi}(e^{i\psi})\overline{g_\psi}(e^{i\psi}))}{|g_\psi(e^{i\psi})|^3} - \mathrm{Re}(g(e^{i\psi})) = \frac{-\varepsilon Q^2}{4\pi^2|\psi_\theta|^2|g_\psi(e^{i\psi})|^2}.$$

The error introduced in the outer region (i.e. for θ close to π) will remain $\mathcal{O}(\varepsilon^\beta)$ until $\varepsilon/|\psi_\theta(\theta)|^2 \sim \mathcal{O}(\varepsilon^\beta)$. Since $\psi_\theta(\theta) = C\varepsilon^\gamma/(C^2\varepsilon^{2\gamma}\sin^2(\theta/2) + \cos^2(\theta/2))$ where C is a constant that depends on γ but not on ε, we wish to find restrictions on θ that guarantee

$$C^2\varepsilon^{2\gamma}\sin^2(\theta/2) + \cos^2(\theta/2) \lesssim C\varepsilon^{\gamma+(\beta-1)/2}$$

If we take $\sin^2(\theta/2) \sim \varepsilon^{-\gamma+(\beta-1)/2}$, then $\cos^2(\theta/2) \sim 1$ which does not satisfy the given balance. We must therefore take $\cos^2(\theta/2) \sim \varepsilon^{\gamma+(\beta-1)/2} \Rightarrow \varepsilon^{2\gamma} \sin^2(\theta/2) \sim \varepsilon^{2\gamma}$, so that $\tan(\theta/2) \sim \varepsilon^{-\gamma/2-(\beta-1)/4}$. This will satisfy the given balance as long as $\gamma \leq (\beta-1)/2$, or equivalently, $\beta \geq 2\gamma + 1$.

To obtain a uniform bound on the error in the composite solution, we must set $\alpha = \beta$ and calculate which values of α produce inner and outer regions (expressed with respect to θ) that overlap. We therefore solve $\gamma(\alpha-2) \leq -\gamma/2-(\alpha-1)/4$ which yields $\alpha \leq (6\gamma+1)/(4\gamma+1)$. However, the inequality $1+2\gamma \leq \alpha \leq (6\gamma+1)/(4\gamma+1)$ has no solutions for $\gamma \in (1/2, 1)$. This is because we have neglected to properly consider the 'outer outer' region (in which electrostatic pressure balances gravity) in our composite solution, and the outer solution we derived above should not remain valid through $\theta = \pi$. As argued in §3.5.1, the error introduced in the computed profile in the 'outer outer' region should nevertheless be extremely small and this is confirmed when we computed matched solutions (Fig.s 4.9(a) and 4.9(b)). We directly inspect the 'overlap' between inner and outer profiles in Fig.s 4.8(a) and 4.8(b), and find that for a suitable[4] error tolerance it is possible to identify a region of the form $\varepsilon k < x < K$ with k and K $\mathcal{O}(1)$ constants in which both inner and outer profiles differ from the overlap profile by no more than the selected tolerance.

Computed solutions

First, we verify that the matched solutions agree well with full computed solutions in regions where they overlap. Figures 4.9(a) and 4.9(b) compare inner and outer profiles computed using the collocation method of §3.4 (solid curves) and the matching method of the present section, for $l = 1$, $h(0) = 0.96$, $M = 256$, $M_{inner} = 16$, and $M_{outer} = 256$. The computation times required to calculate each profile type are of the same order of magnitude. The full bifurcation diagrams computed using the full

[4]The referenced plots clearly show the existence of a lower bound on the allowable range of tolerances for fixed ε, but also that this lower bound decreases as ε decreases.

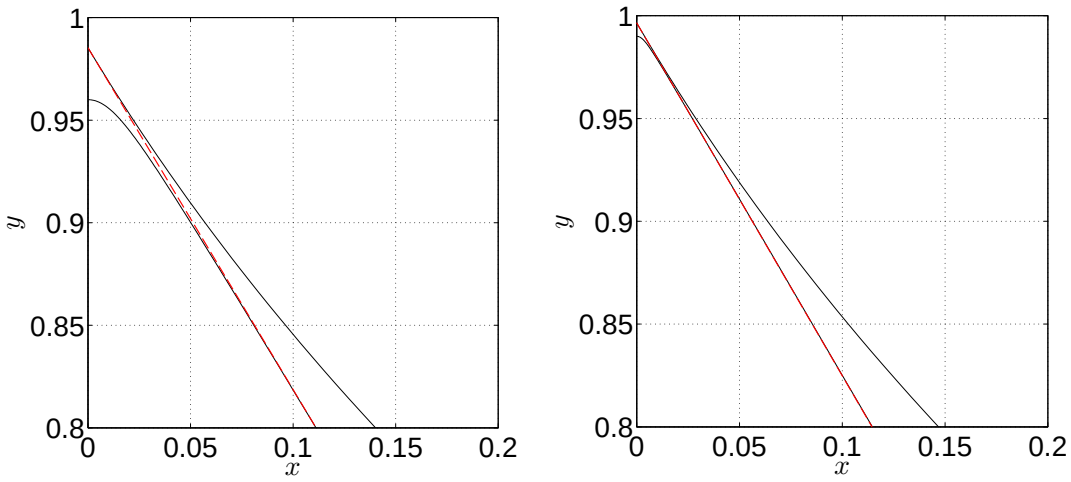

FIGURE 4.8. Inner and outer solution profiles (solid black lines) for $l_1 = 1$, $M_{out} = 128$, $N_{out} = 128$, $M_{in} = 32$, $N_{in} = 128$. Each profile is compared to the overlap profile $\mathcal{G}$ (red dashed line). By comparing the profiles computed using (a) $\varepsilon = 0.04$ and (b) $\varepsilon = 0.01$, we observe that the region in which both inner and outer profiles agree with the overlap profile to within a given tolerance is of the form $\varepsilon k < x < K$ where k and K are both $\mathcal{O}(1)$.

collocation method (solid curve), leading order large deflection approximation (dashed curve) and matching method (dotted curve) with $l = 1$ are compared in Fig. 4.9(c). The matched solutions improve on the accuracy of the leading order solutions for all $\varepsilon \in (0, 1)$, while remaining efficient for $\varepsilon \ll 1$.

The matching method described does not produce useable solutions for l_0 close to $\sqrt{2}$. As $\sqrt{2} - l_0$ becomes small, the scaling used in creating these matched solutions does not remain appropriate (the asymptotically angled outer limits of inner solutions have exterior angle $\sim 2(\pi - \delta)$ for $\delta \ll 1$, and therefore the gravitational term can only be considered small relative to the elastic and electrostatic terms in some very small neighborhood of the interface tip). We will need a different scaling that properly accommodates the small length scale $\sqrt{2} - l_0$ to investigate this particular regime.

Figures 4.10(a) and 4.10(b) show matched profiles created by combining a single

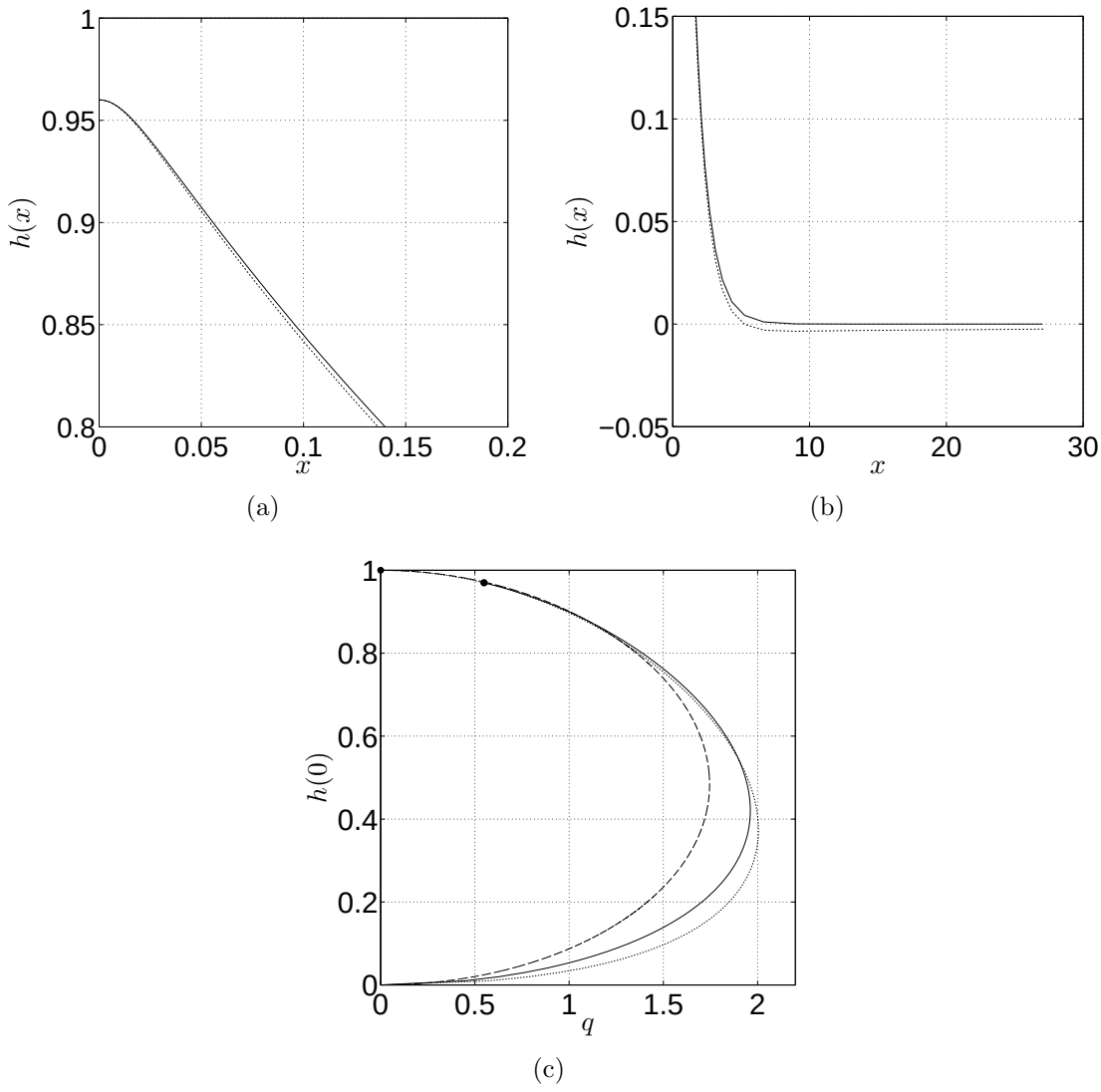

FIGURE 4.9. (a) Interface tip profiles computed using the collocation method of §3.4 (solid) and the matching method of §4.1.3 (dashed) for $L = 1$, $h(0) = 0.96$, $M = 256$, $M_{inner} = 16$, $M_{outer} = 256$. The discrepancy is $\mathcal{O}(\varepsilon^2)$ as expected. (b) The same profiles as in (a), compared in the outer region. The error in matched profiles is uniformly $\mathcal{O}(\varepsilon^2)$ as claimed. (c) The computed and leading order bifurcation diagrams of Fig. 4.2 (solid and dashed curves respectively) compared to the bifurcation diagram based on matched solutions (dotted curve) with $l_0 = 1$.

pair of inner and outer profiles using different values of ε. Generating profiles in this way (with fixed γ) is extremely efficient once the initial calculations required to determine the appropriate inner and outer solutions have been performed. Note that the first order corrected forcing height l_1 is not equal for all these interfaces. This is a minor drawback when seeking solutions of the forward problem.

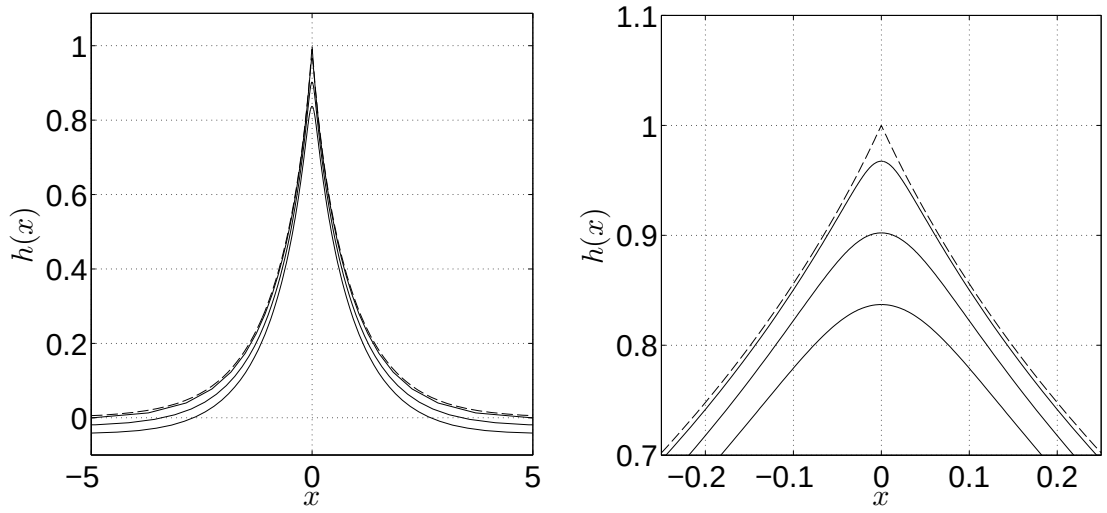

FIGURE 4.10. (a) Matched profiles computed with $h_0(0) = 1$ and $\varepsilon = 0.03$, 0.1, 0.17. The inner and outer solutions only need to be calculated once to produce these plots. (b) Tip shapes for the profiles from (a). The rescaling of the inner solution by ε produces the appropriate tip curvature in each case.

4.1.4 Inner Solutions, Iterative Integral Equation Method

While we are able to construct exact (if implicit) representations for outer solution profiles and measure the accuracy of our conformal mapping based outer solution profiles against them, inner solutions as described above are (like full computed solutions) determined by directly minimizing the governing pressure balance. The need to specify an arbitrary parameter T ahead of time is a weakness of the method since asymptotic solution accuracy is influenced by T in an unpredictable manner

(Fig. 4.6(c)). In the present section, we detail an alternate, iterative method for producing approximations to inner solution maps.

Let $\Xi(\theta) = iF(e^{i\theta})$ parametrize the inner solution (image) deflection profile, and define the function $\chi(\theta)$ by

$$\Xi_\theta = |\Xi_\theta| \exp(i\chi(\theta)). \tag{4.1.31}$$

$\chi(\theta)$ represents the argument of the tangent to the deflection profile at $iF(e^{i\theta})$. The inner region equation (4.1.21) may then be written

$$\frac{1}{|\Xi_\theta(\theta)|}\frac{d\chi}{d\theta} = -\frac{Q^2}{4\pi^2|\Xi_\theta(\theta)|^2} \Longrightarrow \chi(\theta) = -\frac{Q^2}{4\pi^2}\int_0^\theta \frac{dt}{|\Xi_\theta(t)|}. \tag{4.1.32}$$

The expression used to represent the curvature is based on the definition $\kappa(s) = (dt/ds)\cdot n$ plus one application of the chain rule, where $t(\Xi(\theta)) = (\cos(\chi(\theta)), \sin(\chi(\theta))$ and $n(\Xi(\theta)) = (-\sin(\chi(\theta)), \cos(\chi(\theta)))$. The constant of integration is chosen to match the orientation of the inner profile, i.e. to ensure that $\chi(0) = 0$. (4.1.32) can be used to define an iterative process that produces inner solution profiles for either (i) given inner forcing strength Q, or (ii) given asymptotic angle $\chi(\pi)$.

We begin with an initial guess for the deflection profile, $\Xi(\theta)$ for $\theta \in (-\pi, \pi]$. If Q is given, we can immediately compute $\chi(\theta)$ using (4.1.32). If the asymptotic angle $\chi(\pi)$ is known, we can first calculate Q via the equation

$$\chi(\pi) = -\frac{Q^2}{4\pi^2}\int_0^\pi \frac{dt}{|\Xi_\theta(t)|}, \tag{4.1.33}$$

and then proceed as in the first case.

Since $\Xi(\theta) = iF(e^{i\theta})$, $\Xi_\theta(\theta) = -e^{i\theta}F_w(e^{i\theta}) = -wF_w(w)$ on $|w| = 1$. Dividing both sides of equation (4.1.31) by their respective complex conjugates yields

$$\frac{wF_w(w)}{\overline{wF_w(w)}} = \exp\left(2i\chi(\theta)\right)$$

on $|w| = 1$.

The symmetry of deflection profiles suggests that it should always be possible to write

$$\chi(\theta) = \sum_{n=1}^{\infty} \chi_n \sin(n\theta), \text{ with } \chi_n = \frac{1}{\pi}\int_{-\pi}^{\pi} \chi(\theta)\sin(n\theta)d\theta.$$

We approximate this representation of χ numerically by using $M < \infty$ modes. Note that χ will be discontinuous at $\pm\pi$, so we expect overshoot in our Fourier series representation of χ near these points due to Gibb's phenomenon. (This will not be an issue when we apply this method to compute inner solutions of the modified system forced by a dipole - the logarithmic growth in inner region profile deflections corresponds to asymptotic angle $\chi(\pi) = 0$, so the periodic extension of χ to $\mathbb{R}$ will be smooth.) This overshoot is smoothed at each step when computing the interface representation via (4.1.36).

We may now write

$$\frac{wF_w(w)}{\overline{wF_w(w)}} = \exp\left(2i\sum_{n=1}^{M}\chi_n \sin(n\theta)\right) = \frac{\exp\left(\sum_{n=1}^{M}\chi_n w^n\right)}{\exp\left(\sum_{n=1}^{M}\chi_n \overline{w}^n\right)} \tag{4.1.34}$$

on $|w| = 1$. Because all coefficients in the definition of F are real, $\overline{F_w(w)} = F_w(\overline{w})$. Note also that

$$(1+w)^2 = (1+2w+w^2) = w(\overline{w}+2+w)$$

and

$$(1+\overline{w})^2 = (1+2\overline{w}+\overline{w}^2) = \overline{w}(\overline{w}+2+w)$$

so that

$$\frac{w}{\overline{w}} = \frac{(1+w)^2}{(1+\overline{w})^2}$$

everywhere on the unit circle. (4.1.34) is therefore equivalent to the equation

$$\frac{(1+w)^2F_w(w)}{\exp\left(\sum_{n=1}^{M}\chi_n w^n\right)} = \frac{(1+\overline{w})^2F_w(\overline{w})}{\exp\left(\sum_{n=1}^{M}\chi_n \overline{w}^n\right)}.$$

The map $C(w) = A(1-w)/(1+w)$, which sends the unit circle to the imaginary axis, forms the basis of the class of conformal maps we use to represent image deflection profiles. Since $C_w(w) = -2A/(1+w)^2$, the function C_w has a second order pole at $w = -1$. However, the product $(1+w)^2C_w(w)$ will be analytic at $w = -1$. Writing $F(w) = C(w) + D(w)$, where D controls the interface deflection and is

temporarily assumed to be no more singular than C near $w = -1$, we may deduce that $(1+w)^2 F_w(w)/\exp\left(\sum_{n=1}^{M} \chi_n w^n\right)$ is both analytic and anti-analytic[5] with respect to the argument w on $\overline{\mathbb{D}}$. This allows us to apply the following result:

Lemma 4.1.4. Let $f(w) : D_0 \to D_1$ be both analytic and anti-analytic on the domain D_0. Then f is constant on D_0.

Proof of Lemma 4.1.4. Since f is analytic in D_0, it can be expanded in a power series in w about any point in D_0. Similarly, since f is anti-analytic in D_0, it can be expanded in a power series in $\overline{w}$ about any point in D_0. These two expansions must be equal, and this can only be true if $f(w) \equiv K$ in D_0. □

The function $(1 + w)^2 F_w(w)/\exp\left(\sum_{n=1}^{M} \chi_n w^n\right)$ must therefore be constant everywhere in $\overline{\mathbb{D}}$. Denoting this constant value by K, F_w is now known to satisfy the equation

$$F_w(w) = \frac{K \exp\left(\sum_{n=1}^{M} \chi_n w^n\right)}{(1+w)^2}. \tag{4.1.35}$$

(4.1.35) directly defines $\Xi_\theta(\theta)$, so the iterative loop is closed and we may repeat these update steps beginning with (4.1.33) until the change in $\chi(\theta)$ is small everywhere in $(-\pi, \pi]$.

F is subject to the boundary conditions $F(0) - F(1) = 1$ (to produce the correct tip-charge separation in physical variables) and $F(1) = 0$ (without loss of generality). The first condition can be met by requiring that

$$K = \left(\int_0^1 \frac{\exp\left(\sum_{n=1}^{M} \chi_n x^n\right)}{(1+x)^2} dx \right)^{-1}$$

(relying on the analyticity of F_w away from $w = -1$), and the second may be enforced as an initial condition of the numerical integration at $\theta = 0$. deflection profiles are then given by

$$\Xi(\theta) = \int_0^\theta F_w(e^{i\theta}) i e^{i\theta} d\theta, \ -\pi < \theta < \pi, \tag{4.1.36}$$

[5] A function $f(w)$ is said to be anti-analytic if and only if $f(\overline{w})$ is an analytic function of $\overline{w}$.

for computed values of K and χ_n.

Figure 4.11(a) shows a typical inner solution computed using the outlined iterative method with $M = 32$ and $\chi(\pi) = -\pi/4$ (solid curve), compared against the same inner solution computed using the method of §4.1.2 with $M = 32$ and $\gamma = 2/3$ (dashed curve).[6] The agreement is excellent close to the deflection profile tip. The convergence of the iterative method to the final plotted profile is extremely rapid (Fig. 4.11(b)) even when beginning with a poor initial guess (a flat interface, in this example). However, the discontinuity in χ ensures that the Fourier approximation to χ will always be asymptotically flat leading to inaccuracies of the type displaying in Fig. 4.11(c) for large enough X. Unsurprisingly, the range of X-values for which profiles computed using the two methods agree can be extended by increasing M, demonstrated in Fig. 4.11(d) in which $\chi(\pi) = -\pi/4$ and $M = 256$.

To overcome the inaccuracies due to Gibb's phenomenon, we utilize the known Fourier series representation

$$\frac{2\chi(\pi)}{\pi}\sum_{n=1}^{\infty}\frac{(-1)^{n+1}}{n}\sin(n\theta).$$

of the sawtooth function defined by periodic extension of $\chi(\pi)x/\pi$, $x \in (-\pi, \pi]$ to $\mathbb{R}$. Write

$$\chi(\theta) = \sum_{n=1}^{M}\widehat{\chi}_n\sin(n\theta) + \frac{2\chi(\pi)}{\pi}\sum_{n=1}^{\infty}\frac{(-1)^{n+1}}{n}\sin(n\theta)$$

where the first term represents a finite-term approximation of the deviation of χ from the sawtooth function. This deviation will be at least C^1 by the symmetry of inner profiles.

Now

$$\frac{(1+w)^2F_w(w)}{(1+\overline{w})^2\overline{F_w(w)}} = \frac{\exp\left(\sum_{n=1}^{M}\widehat{\chi}_n w^n\right)\exp\left(\frac{2\chi(\pi)}{\pi}\sum_{n=1}^{\infty}\frac{(-1)^{n+1}}{n}w^n\right)}{\exp\left(\sum_{n=1}^{M}\widehat{\chi}_n \overline{w}^n\right)\exp\left(\frac{2\chi(\pi)}{\pi}\sum_{n=1}^{\infty}\frac{(-1)^{n+1}}{n}\overline{w}^n\right)} \tag{4.1.37}$$

[6] In general, $\gamma = \pi/(\pi - 2\chi(\pi))$.

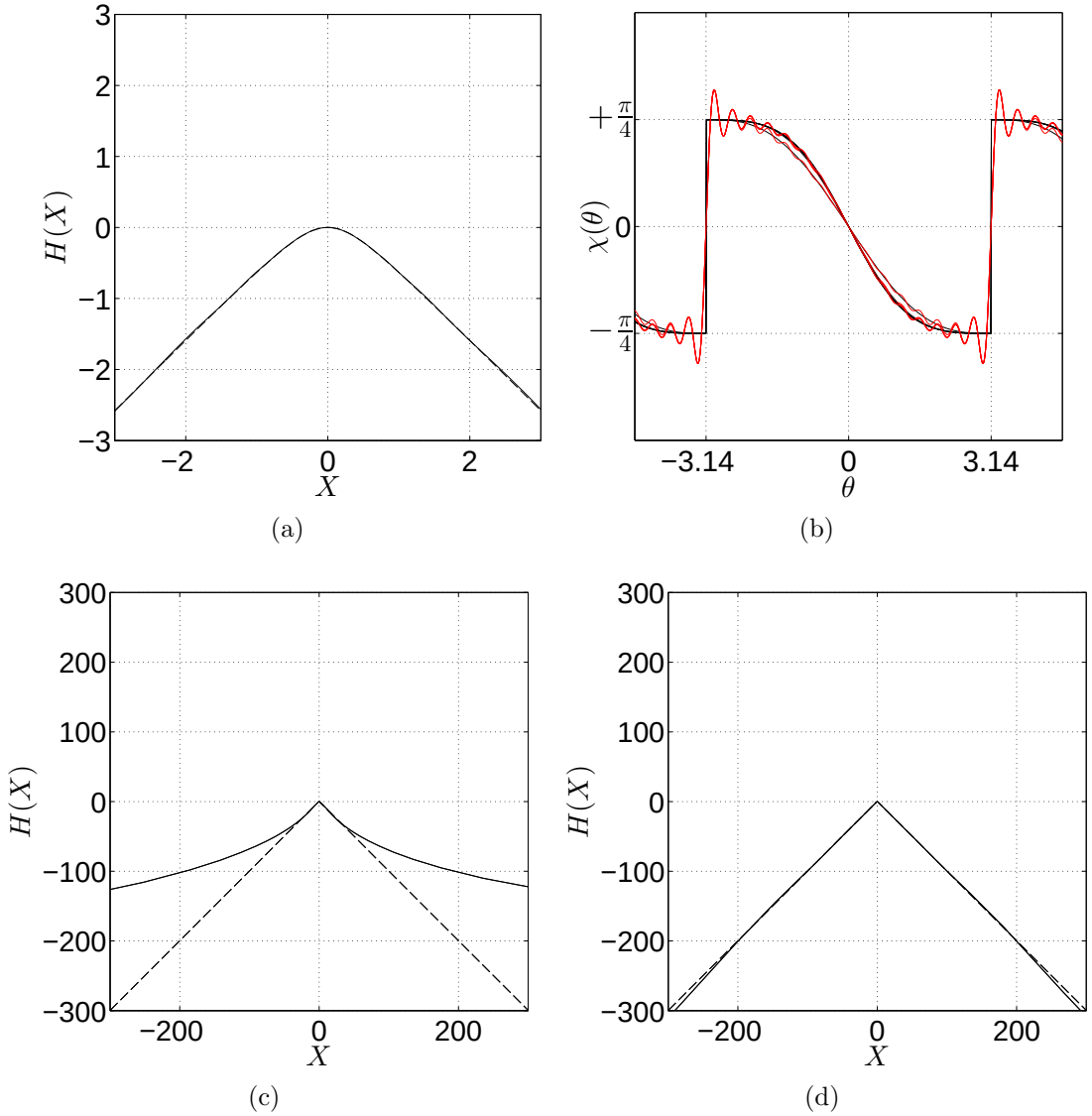

FIGURE 4.11. (a) Inner solution computed using the iterative method of §4.1.4 with $M = 32$ and $\chi(\pi) = -\pi/4$ (solid curve) plotted against inner solution computed using the method of §4.1.2 with $M = 32$ and $\gamma = 2/3$ (dashed curve). The agreement is excellent close to the tip. (b) The calculated functions $\chi(\theta)$ (black) and their Fourier approximations (red). The scheme converges to a final solution rapidly, even from a poor initial guess (here the initial interface was taken to be flat). (c) Gibb's phenomenon limits the accuracy of the computed inner solution far away from the tip. All approximate interfaces calculated using this method will have asymptotic angle equal to zero. (d) The region in which the iterated solution is accurate may be extended by increasing M, here to 256. This delays the onset of inaccuracies due to Gibb's phenomenon.

on $|w| = 1$. Noting that

$$\frac{2\chi(\pi)}{\pi}\sum_{n=1}^{\infty}\frac{(-1)^{n+1}}{n}w^n = \frac{2\chi(\pi)}{\pi}\log(1+w),$$

(4.1.37) may be rewritten

$$\frac{(1+w)^2F_w(w)}{(1+\overline{w})^2\overline{F_w(w)}} = \frac{\exp\left(\sum_{n=1}^{M}\widehat{\chi}_n w^n\right)(1+w)^{2\chi(\pi)/\pi}}{\exp\left(\sum_{n=1}^{M}\widehat{\chi}_n \overline{w}^n\right)(1+\overline{w})^{2\chi(\pi)/\pi}}.$$

If the branch cut associated with the fractional power of $(1+w)$ is positioned between -1 and $-\infty$ along the negative real axis, Lemma 4.1.4 applies and we deduce that F_w now satisfies

$$F_w(w) = \frac{K\exp\left(\sum_{n=1}^{M}\widehat{\chi}_n w^n\right)}{(1+w)^{2(1-\chi(\pi)/\pi)}}.$$

Defining

$$K = \left(\int_0^1 \frac{\exp\left(\sum_{n=1}^{M}\widehat{\chi}_n x^n\right)}{(1+x)^{2(1-\chi(\pi)/\pi)}}dx\right)^{-1},$$

completely determines the new form of F_w, and hence the interface deflection profile Ξ through the same equation (4.1.36) as before.

The profiles computed using this method agree extremely well with profiles from §4.1.2 for all values of $\theta \in (-\pi, \pi)$. Convergence remains fast as for the original scheme (refer to Fig. 4.11(b)).

4.2 Dipole Forcing, Inner Solutions

We now briefly discuss inner solutions for the modified electrostatic case forced by a dipole. The method we use to compute inner solutions for dipole forcing is identical to that of §4.1.4. However, the linear dependence of electrostatic pressure on the electric field at the interface allows a much more explicit form for F_w to be found. No iteration is required to produce accurate numerical inner solutions. We note that it would be possible to apply the collocation method of §4.1.2 to determine inner solutions of

the dipole-forced modified EMS if desired, but this would be much less efficient than the method presented. Calculation of outer solutions and matched solutions for this system remains future work and is discussed in Chapter 6.

The primary pressure balance near the tip of large deflection profiles forced by a dipole is between electrostatic and elastic terms exactly as for point charge forcing (Fig. 3.11(a)). The full equation governing dipole-forced systems (3.3.8) unsurprisingly reduces to

$$\frac{\mathrm{Im}(F_{\theta\theta}(e^{i\theta})\overline{F_\theta}(e^{i\theta}))}{|F_\theta(e^{i\theta})|^3} = -\frac{\widehat{q}\cos\theta}{\pi|F_\theta(e^{i\theta})|} \tag{4.2.1}$$

under the same scaling $\mathbb{F} = \varepsilon F$ as used for point charge forcing. Recall that we consider values of $\widehat{q} > 0$.

Let $\Xi(\theta)$ and $\chi(\theta)$ be defined as in §4.1.4. Then (4.2.1) yields

$$\frac{1}{|\Xi_\theta(\theta)|}\frac{d\chi}{d\theta} = -\frac{\widehat{q}\cos\theta}{\pi|\Xi_\theta(\theta)|} \Longrightarrow \chi(\theta) = -\frac{\widehat{q}\sin\theta}{\pi}.$$

We again fix the constant of integration to be zero so that $\chi(0) = 0$. We note that the interface will fold if $\widehat{q} > \pi^2/2$. (There is no method for immediately determining for which $\widehat{q}$ values the corresponding interface will self-intersect (a non-physical situation)). Because we have a closed-form expression for χ, the same arguments as for point charge forcing now produce the explicit equation

$$F_w(w) = \frac{K\exp\left(-\widehat{q}w/\pi\right)}{(1+w)^2} \tag{4.2.2}$$

for F_w (the analog of (4.1.35)). The corresponding profile may still be computed by (4.1.36), with

$$K = \left(\int_0^1 \frac{\exp\left(-\widehat{q}x/\pi\right)}{(1+x)^2}dx\right)^{-1}$$

to enforce the boundary condition $F(0) - F(1) = 1$.

Figures 4.12(a) and 4.12 compare full profiles computed using the collocation method of section §4.1.4 plotted against inner region profiles (scaled by ε) obtained via numerical evaluation of (4.1.36). The values of $\widehat{q}$ computed by the collocation method

are used as inputs to the inner solution integration. We see excellent agreement between full profiles and inner solution profiles near the full profile tip for all values of ε. The points at which the computed inner solutions fail to accurately represent the full solution tip profile agree with the locations at which the gravitational term becomes relatively important. All inner profiles exhibit logarithmic growth as $|\theta| \to \pi$, but this does not contradict the assumed analyticity of $(1+w)^2 F_w(w)$ near $w = -1$. We therefore expect that outer solutions for this system must exhibit logarithmic growth near $x = 0$ (in contrast to the corners featured in the outer solutions of §4.1.1).

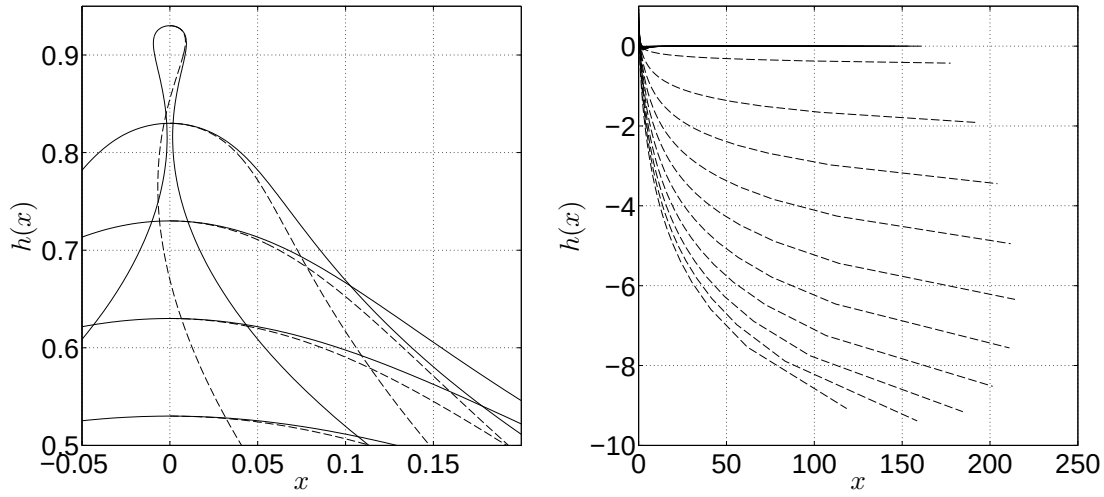

(a)

FIGURE 4.12. Full deflection profiles computed using the collocation method of §3.4 (solid curves) plotted against inner region profiles obtained via numerical evaluation of (4.2.2) (dashed curves).

Chapter 5

Electrostatic Models: The Inverse Problem

In Chapters 2, 3 and 4, our focus was on forward problems in which properties of the forcing applied to the system are treated as inputs and the corresponding equilibrium deflection profiles are sought. This is the most natural approach to take when models are derived from existing experiments, where the forcing is typically a fixed part of the experimental design. In the present chapter, we investigate the inverse problem: for any given candidate deflection profile, does there exist a forcing configuration for which the corresponding system is in both electrostatic and mechanical equilibrium (and if so, how do we compute it)? While models of the forward problem have allowed us to gain a more thorough understanding of the interactions between elastic, electrostatic and gravitational forces within a microelectromechanical system, solutions computed for inverse problems may be used to directly inform the design of MEMS and to gain direct control over the deflection profiles produced.

As in Chapter 3, we find that this question is best addressed within the framework of complex analysis. We therefore continue to represent candidate deflection profiles as images of the unit circle $\partial\mathbb{D}$ under conformal maps $\mathbb{F} : w \mapsto z$ (see §3.3 for the justification). We describe a class of conformal maps for which it is always possible to compute the requisite forcing configuration in Claim 5.0.4, and demonstrate the calculation of the forcing for several specific maps $\mathbb{F}$ related to the forward problems studied earlier.

The steps required to determine the appropriate forcing for a given map $\mathbb{F}$ are as follows:

1. Compute the induced charge density (or equivalently, the normal component of the electric field) on the unit circle in the preimage plane required to balance

the elastic and gravitational forces experienced by the image interface;

2. From this charge density, define a consistent extension of the electric field everywhere inside the unit disc;

3. Find the poles and residues of this electric field to locate singularities and their strengths in the preimage plane;

4. Map these singularities and their strengths to the image plane to find the physical forcing configuration.

We describe each step in more detail in the following section. The method is applied to inner solutions of the modified electrostatic problem (which features a linear relationship between electric field and induced electrostatic pressure at the conducting interface) as this is the simplest case to demonstrate. Comments on other extensions are given in §5.4.

Inner solutions are described by a balance between elastic and electrostatic forces only. For the inverse problem in which the inner solution map F is given, this relationship (a generalization of (4.2.1)) *defines* the normal electric field E_n on $\partial\mathbb{D}$ in the preimage plane required to support the corresponding image interface deflection:

$$\frac{E_n(e^{i\theta})}{|F_\theta(e^{i\theta})|} = \frac{\mathrm{Im}(F_{\theta\theta}(e^{i\theta})\overline{F_\theta}(e^{i\theta}))}{|F_\theta(e^{i\theta})|^3}. \tag{5.0.1}$$

If we define $\Xi(\theta)$ and $\chi(\theta)$ as in §4.1.4, (5.0.1) becomes

$$\frac{E_n(e^{i\theta})}{|\Xi_\theta(\theta)|} = \frac{1}{|\Xi_\theta(\theta)|}\frac{d\chi}{d\theta} \Rightarrow E_n(e^{i\theta}) = \frac{d\chi}{d\theta}.$$

Determining $E_n(e^{i\theta})$ on $\partial\mathbb{D}$ is therefore reduced to finding an expression for $\chi_\theta(\theta)$ on $\partial\mathbb{D}$.

Note that $\Xi_\theta(-\theta) = ie^{-i\theta}F_\theta(e^{-i\theta}) = -\overline{\Xi_\theta}(\theta)$ and similarly that $\Xi_{\theta\theta}(-\theta) = \overline{\Xi_{\theta\theta}}(\theta)$ by the symmetry of the given deflection profile.

By definition,

$$\exp(2i\chi(\theta)) = \frac{\Xi_\theta(\theta)}{\overline{\Xi_\theta}(\theta)} = -\frac{\Xi_\theta(\theta)}{\Xi_\theta(-\theta)},$$

so that

$$2i\chi_\theta(\theta)\exp(2i\chi(\theta)) = -\left(\frac{\Xi_\theta(-\theta)\Xi_{\theta\theta}(\theta) + \Xi_\theta(\theta)\Xi_{\theta\theta}(-\theta)}{\Xi_\theta^2(-\theta)}\right).$$

Substituting for $\exp(2i\chi(\theta))$ gives

$$\begin{aligned}
\chi_\theta(\theta) &= \frac{1}{2i}\frac{\Xi_\theta(-\theta)}{\Xi_\theta(\theta)}\left(\frac{\Xi_\theta(-\theta)\Xi_{\theta\theta}(\theta) + \Xi_\theta(\theta)\Xi_{\theta\theta}(-\theta)}{\Xi_\theta^2(-\theta)}\right), \\
&= \frac{1}{2i}\left(\frac{\Xi_{\theta\theta}(\theta)}{\Xi_\theta(\theta)} + \frac{\Xi_{\theta\theta}(-\theta)}{\Xi_\theta(-\theta)}\right), \\
&= \frac{1}{2i}\left(\frac{\Xi_{\theta\theta}(\theta)}{\Xi_\theta(\theta)} - \overline{\left(\frac{\Xi_{\theta\theta}(\theta)}{\Xi_\theta(\theta)}\right)}\right),
\end{aligned}$$

which specifies E_n completely in terms of Ξ (i.e. F):

$$E_n(e^{i\theta}) = \mathrm{Im}\left(\frac{\Xi_{\theta\theta}(\theta)}{\Xi_\theta(\theta)}\right).$$

Our next target is to calculate the electric field inside $\mathbb{D}$ based on the boundary values just computed. We express the electric potential and electric field as complex-valued functions, and extrapolate the relationship between them by considering the potential and field induced by a single point charge located inside $\mathbb{D}$.

For a charge of strength $\widehat{q}$ located at $w = u_0 \in (-1, 1)$, the electric potential $\phi(w)$ that makes $\partial\mathbb{D}$ an equipotential is given by

$$\phi(w) = -\frac{\widehat{q}}{2\pi}\left(\log|w - u_0| - \log\left|w - \frac{1}{w_0}\right|\right).$$

If we write $w = u + iv$ and treat ϕ as a function of u and v, we can directly compute

$$E(w) = -\nabla\phi = \frac{\widehat{q}}{2\pi}\left(\frac{w - u_0}{|w - u_0|^2} - \frac{w - 1/u_0}{|w - 1/u_0|^2}\right) = \frac{\widehat{q}}{2\pi}\left(\frac{1}{\overline{w - u_0}} - \frac{1}{\overline{w - 1/u_0}}\right).$$

Taking a derivative of ϕ with respect to w directly yields

$$\begin{aligned}
\frac{d\phi}{dw} &= -\frac{\widehat{q}}{2\pi}\left(\frac{1}{|w-u_0|}\frac{d|w-u_0|}{dw} - \frac{1}{|w-1/u_0|}\frac{d|w-1/u_0|}{dw}\right), \\
&= -\frac{\widehat{q}}{2\pi}\left(\frac{1}{|w-u_0|}\exp(-i\arg(w-u_0)) - \frac{1}{|w-1/u_0|}\exp(-i\arg(w-1/u_0))\right), \\
&= -\frac{\widehat{q}}{2\pi}\left(\frac{\overline{w-u_0}}{|w-u_0|^2} - \frac{\overline{w-1/u_0}}{|w-1/u_0|^2}\right), \\
&= -\frac{\widehat{q}}{2\pi}\left(\frac{1}{w-u_0} - \frac{1}{w-1/u_0}\right), \qquad (5.0.2)
\end{aligned}$$

and we deduce that

$$E(w) = -\overline{\frac{d\phi}{dw}}$$

everywhere in $\mathbb{D}$. The (inward) normal component of E at $w = e^{i\theta}$ is given by

$$\begin{aligned}
E_n(w) &= \frac{\widehat{q}}{2\pi}\left(\frac{(u-u_0,v)}{|w-u_0|^2} - \frac{(u-1/u_0,v)}{|w-1/u_0|^2}\right)\cdot(-u,-v), \\
&= -\frac{\widehat{q}}{2\pi}\left(\frac{u(u-u_0)+v^2}{|w-u_0|^2} - \frac{u(u-1/u_0)+v^2}{|w-1/u_0|^2}\right), \\
&= -\frac{\widehat{q}}{2\pi}\left(\frac{\mathrm{Re}(w)\mathrm{Re}(w-u_0)+\mathrm{Im}(w)\mathrm{Im}(w-u_0)}{|w-u_0|^2}\right. \\
&\qquad\qquad \left. -\frac{\mathrm{Re}(w)\mathrm{Re}(w-1/u_0)+\mathrm{Im}(w)\mathrm{Im}(w-1/u_0))}{|w-1/u_0|^2}\right), \\
&= \mathrm{Re}\left(w\frac{d\phi}{dw}\right).
\end{aligned}$$

Since $\partial\mathbb{D}$ is a conductor,

$$E_t(w) \propto \mathrm{Im}\left(w\frac{d\phi}{dw}\right) = 0$$

for all $w \in e^{i\theta}$. We may therefore write

$$E_n(w) = w\frac{d\phi}{dw} \Rightarrow \frac{d\phi}{dw} = \frac{E_n(w)}{w} \qquad (5.0.3)$$

on $\partial\mathbb{D}$.

There is no unique extension of $d\phi/dw$ to the interior of $\mathbb{D}$. In the following explicit examples, we choose to 'formally' extend $d\phi/dw$ to all of $\mathbb{D}$ using the formula

(5.0.3). $E(w)$ defined using this method will correspond to an electric field generated by finitely many point charges inside $\mathbb{D}$ (this is guaranteed whenever the assumptions of Claim 5.0.4 are satisfied). However, even if Claim 5.0.4 does not apply, a multipole expansion centered at $w = 0$ will always be able to match E_n on $\partial\mathbb{D}$ ($E_n(e^{i\theta})$ is a real-valued even function of θ, so may be expanded in a Fourier cosine series). The following claim shows that this extension will be rational in $\mathbb{D}$ whenever the map $F_w(w)$ is a rational function of w in $\overline{\mathbb{D}}$.

Claim 5.0.4. *Let $F_w(w)$ be a rational function of w defined on $\overline{\mathbb{D}}$. Then $d\phi/dw$ defined on $\overline{\mathbb{D}}$ by* (5.0.3) *is a rational function of w.*

Proof of Theorem 5.0.4. First, note that $F_\theta(w) = iwF_w(w)$ for $w \in \partial\mathbb{D}$, so $F_\theta(w)$ is a rational function of w on $\partial\mathbb{D}$ whenever $F_w(w)$ is. (5.0.1) may be rewritten as

$$E_n(w) = \frac{F_{\theta\theta}(w)\overline{F_\theta(w)} + \overline{F_{\theta\theta}(w)}F_\theta(w)}{2iF_\theta(w)\overline{F_\theta(w)}} \tag{5.0.5}$$

for $w \in \partial\mathbb{D}$. It is clear that both the derivative of a rational function and the product (and therefore, the ratio) of two rational functions are also rational, so if we show that the conjugated terms in (5.0.5) are rational functions of $w \in \partial\mathbb{D}$ it will follow that $E_n(w)$ is a rational function of $w \in \partial\mathbb{D}$.

Let $f(w) = C\prod_{n=1}^{N}(w - w_n)/\prod_{m=1}^{M}(w - w_m)$ be any rational function defined on $\partial\mathbb{D}$. Then

$$\begin{aligned}\overline{f}(w) &= \frac{\overline{C}\prod_{n=1}^{N}(\overline{w} - \overline{w_n})}{\prod_{m=1}^{M}(\overline{w} - \overline{w_m})}, \\ &= \frac{\overline{C}w^{M-N}\prod_{n=1}^{N}(1 - \overline{w_n}w)}{\prod_{m=1}^{M}(1 - \overline{w_m}w)} \text{ on } \partial\mathbb{D},\end{aligned}$$

i.e. $\overline{f}(w)$ is also a rational function on $\partial\mathbb{D}$.

This is enough to conclude that $E_n(w)$ is a rational function of $w \in \partial\mathbb{D}$, and hence that $d\phi/dw$ defined on $\mathbb{D}$ by (5.0.3) is rational as originally claimed. □

The simple poles of $d\phi/dw$ correspond to isolated point charges in the preimage plane (see (5.0.2)), with the residue of $d\phi/dw$ at each pole indicating the strength of the charge placed there. We therefore expect that any interface deflection generated by a map F whose derivative F_w is rational will be supported by a finite number of isolated singularities whose order matches the multiplicity of the corresponding pole.

5.1 Example 1 - Logarithmic Outer Limit

We now perform the steps outlined in the chapter introduction using the maps F defined by

$$F(w) = \left(\frac{1-w}{1+w}\right) + (1-a)\log(1+w) \tag{5.1.1}$$

for $a \in (0,1)$. The family $F(w)$ consists of maps with rational derivatives constructed to produce interface deflection profiles that exhibit the same logarithmic outer limit as the inner solutions of §4.2.

Note that there is no coefficient on the 'stretching' term $(1-w)/(1+w)$ - the placement of the required preimage plane point charge(s), rather than this stretching coefficient, will be used to produce the correct induced charge density (i.e., the correct scaling of the parametrization) along the given deflection profile. This is in contrast to our calculations with the forward problem in which we fixed the forcing charge at $w = 0$, but the formulations are equivalent - one can be recovered from the other through appropriate automorphisms of the preimage plane.

The map F satisfies $F(1) = (1-a)\log(2)$, $F_\theta(1) = -ia/2$, $F_\theta(1) = -ia/2$, and $F_{\theta\theta}(1) = a/2$, so that the tip curvature $\kappa(1) = (a-1)/a^2 < 0$ for the given range of a values. As this is the first example, explicit expressions for the following steps are given to demonstrate the accuracy of earlier claims.

The normal electric field on $\partial\mathbb{D}$ is given by

$$E_n = \frac{-(1-a)((w-1)^2 + (w+1)^2 a)}{2(1+a-(1-a)w)(1-a-(1+a)w)},$$

a rational function of w. The corresponding poles of $d\phi/dw$ in $\mathbb{D}$ are located at $w = 0$, $w = (1+a)/(1-a)$ and $w = (1-a)/(1+a)$, so that the boundary is supported by two isolated charges (the third is a non-physical image charge) rather than a pure dipole. Based on (5.0.2), the strengths at each pole w_0 are given by $-2\pi\text{Res}(d\phi/dw, w_0)$. The three charges in this case therefore have strengths $-\pi$, π, and $-\pi$ respectively (for any a). The corresponding charge locations in the image (inner solution) plane are $z = 1$, $z = a + (1-a)\log(2/(1+a))$ and $z = -a + (1-a)\log(2/(1-a))$. Two sample image plane configurations are shown in Fig.s 5.1(a) and 5.1(b).

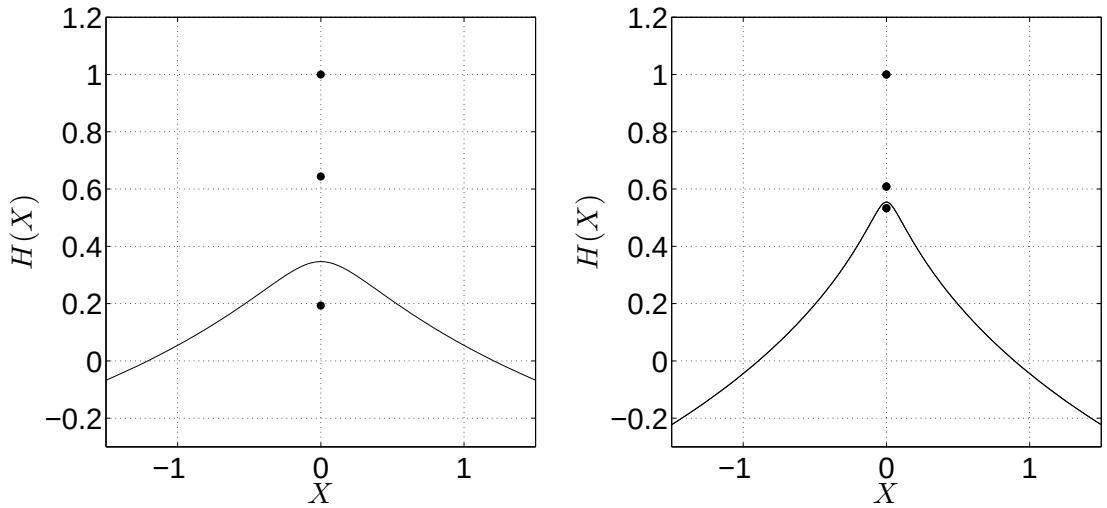

FIGURE 5.1. Deflection profiles and their supporting point charges (solid dots) calculated using maps of the form (5.1.1). Both interfaces diverge logarithmically as $\theta \to \pm\pi$. The charges appearing above the interface are the forcing charges; those appearing below are image charges. (a) $a = 0.5$, $\kappa(1) = -2$. (b) $a = 0.2$, $\kappa(1) = -20$.

5.2 Example 2 - Decaying Outer Limit

We may extend the results of the previous example to show that it is possible for equation (5.0.1) to support inner profiles that decay to zero in the outer limit. We

consider maps of the form

$$F(w) = \left(\frac{1-w}{1+w}\right) + \frac{(1-a)(1+w)}{2} \tag{5.2.1}$$

for $a \in (0,1)$. $F(1) = (1-a)$, and $\kappa(1) = 2(1-a)/a^2$. The same calculations as in the previous example yield image plane point charges of strengths 2π, $-\pi$, $-\pi$, π, and π (for any a) located at $z = (3-a)/2$, $z = ((5-a) \pm 2(1+a)\sqrt{1-a})/(3+a)$, and $z = -1 \pm 2\sqrt{1-a}$ respectively. Figures 5.2(a) and 5.2(b) show two sample interface deflections and the charge configurations that support them.

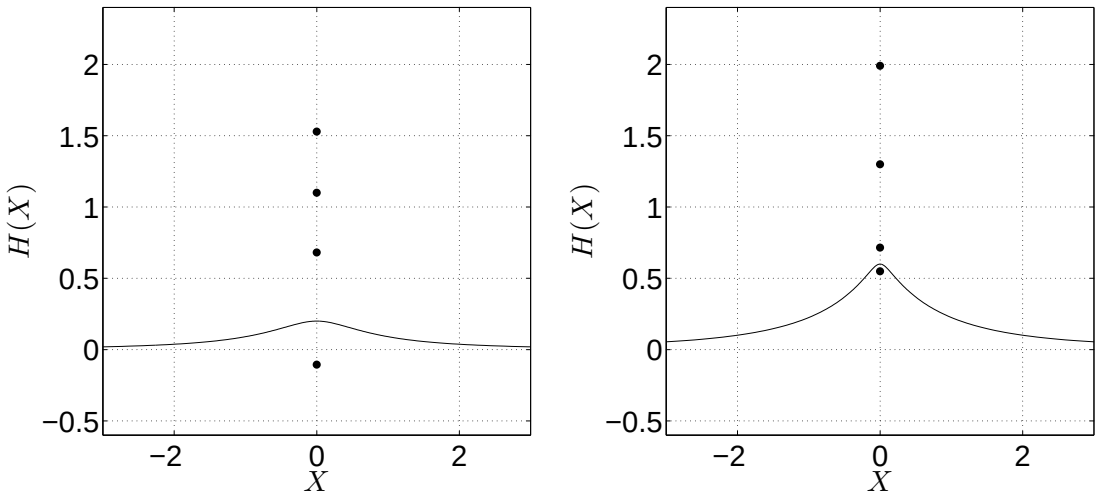

(a) (b)

FIGURE 5.2. Deflection profiles and their supporting point charges (solid dots) calculated using maps of the form (5.2.1). $H(X) \to 0$ as $x \pm \pi$ in both cases. The charges appearing above the interface are the forcing charges; those appearing below are image charges. One image charge is outside the plot window in each case. (a) $a = 0.8$, $\kappa(1) = -0.625$. (b) $a = 0.4$, $\kappa(1) = -7.5$.

5.3 Example 3 - Angled Outer Limit

The final example we consider explicitly consists of maps of the form

$$F(w) = \left(\left(\frac{1-w}{1+w}\right) + a^2\right)^{3/2} - a^3 \tag{5.3.1}$$

whose outer limits are asymptotically angled. We consider $a > 0$ The profiles produced are similar to those of §4.1.2, but are supported by an electrostatic pressure depending linearly on the nearby field.

The derivative of this map with respect to w is *not* a rational map, so Claim 5.0.4 does not apply here. However, we find that the same calculations as before still yield well-defined expressions for the required image charge locations and strengths (that is to say, the calculated $d\phi/dw$ is still a rational function of w on $\mathbb{D}$). This result suggests that the assumptions of Claim 5.0.4 may be weakened to include maps F whose derivatives are algebraic functions (functions constructed of finitely many terms, involving addition, subtraction, multiplication, division, and raising to a fractional power).

$F(1) = 0$, and $\kappa(1) = -1/3|a|^3$. Image charges of strengths $\pi/2$ and $-\pi/2$ (for any a) are located at $z = -a^3$ and $z = (2\sqrt{2} - 1)a^3$ respectively. That the sum of the forcing charge strengths above the interface is non-zero is not a surprise - this is a requirement for the interface to be asymptotically angled according to the form of (5.0.1). (Note also that the sum of the forcing charge strengths is zero in the previous two cases.) Figures 5.3(a) and 5.3(b) demonstrate the forcing configurations needed to support two sample deflection profiles.

5.4 Extensions

It is natural to consider extending this method in two ways: by including the effect of gravity (essentially, to compute full solutions of the modified system), and by squaring the electrostatic pressure term to recover the governing equation for inner solutions of the true EMS. Here we include a brief discussion of each extension.

In the first case, the normal electric field E_n is now defined by

$$E_n(e^{i\theta}) = \mathrm{Im}\left(\frac{\Xi_{\theta\theta}(\theta)}{\Xi_\theta(\theta)}\right) + \left(\frac{\Xi(\theta) + \Xi(-\theta)}{2}\right)\sqrt{-\Xi_\theta(\theta)\Xi_\theta(-\theta)} \tag{5.4.1}$$

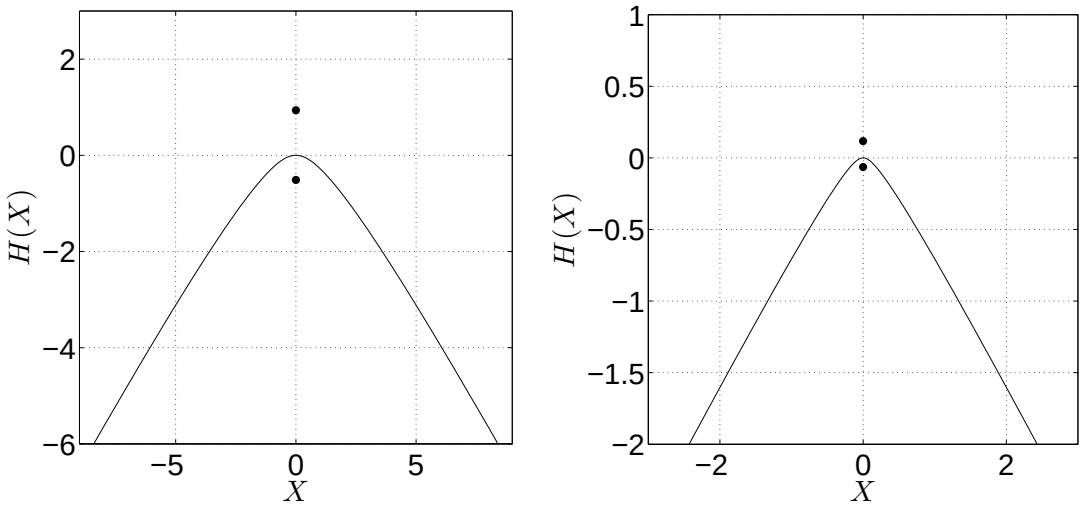

(a) (b)

FIGURE 5.3. Deflection profiles and their supporting point charges (solid dots) calculated using maps of the form (5.3.1). The profiles are both angled for large θ. The charges appearing above the interface are the forcing charges; those appearing below are image charges. (a) $a = 0.8$, $\kappa(1) = -0.65$. (b) $a = 0.4$, $\kappa(1) = -5.2$.

For this to be rational we must place restrictions on the map F itself, rather than F_w as for the previous examples. Care must also be taken in evaluating the second term of (5.4.1) as the square root term diverges as $\theta \to \pm\pi$. Unsurprisingly, this eliminates asymptotically angled deflection profiles from consideration.

In the second case, the normal electric field E_n is now defined by

$$E_n(e^{i\theta}) = \sqrt{\sqrt{-\Xi_\theta(\theta)\Xi_\theta(-\theta)}\,\mathrm{Im}\left(\frac{\Xi_{\theta\theta}(\theta)}{\Xi_\theta(\theta)}\right)}.$$

Which classes of map may produce rational expressions for E_n in this case is not clear - though it is certainly apparent that selecting F_w to be rational or even algebraic is no longer sufficient. It is this case that most directly applies to the design of real MEMS. Clarification of the limitations placed on producible interface shapes when forced by a truncated multipole expansion remains future work.

Chapter 6
Future Work

In this chapter, we give extensions of the research objectives outlined in Chapter 1 and explored in Chapters 2-5. Brief discussion is provided for each idea.

Electromechanical Systems

- While we have developed an efficient and accurate matching method for solutions of the true EMS forced by a point charge with $l < \sqrt{2}$ (Chapter 3), we have yet to extend our analysis to describe interfaces with $l > \sqrt{2}$. Such interfaces can feature long, thin columns (Fig. 6.1), can fold near the tip (Fig. 3.9(c)), and eventually tend to self-intersect. The very tips of such profiles are described by the same (inner region) balance between electrostatic and elastic terms as profiles computed with $l \leq \sqrt{2}$ (and therefore still show one-signed curvature), and the outer region balance is also still between gravity and elasticity until h is much less than one (Fig. 3.9(d)). However, the intermediate region between the inner and outer regions in which all three terms are of equal order of magnitude is more significant when $l > \sqrt{2}$.

- The principles behind the matching method fully explored in §4.1 all apply to the modified EMS forced by a dipole (§4.2). While the force-balance describing outer profiles is different in the modified system, the primary matching conditions (continuity of the deflection profile and induced charge density) remain the same. We plan to compute conformal mapping based representations of outer profiles, and then to develop a method for producing matched solutions for this configuration, exactly as we have for the true EMS.

- The inverse problems with forcing exponent $r = 2$ discussed in Chapter 5 may be related to MEMS designs. For MEMS to be used effectively, systems properties (such as the forcing strength that initiates pull-in) must be extremely well understood and controlled. Further study of this inverse problem, including classification of the stability properties of candidate deflection profiles and quantifying the effect of truncating the forcing multipole expansion at various orders, is required before the analysis can be applied to real system design.

- The matching method of Chapter 4 was applied to calculate unstable equilibrium deflection profiles for the particular systems we studied. However, this method may equally well be applied to compute deflection profiles in dynamic MEMS models. We would like to draw comparisons between our method and existing algorithms when applied to such models.

- All work presented in this thesis has dealt with two-dimensional systems. While our implementation will not translate directly to three dimensional problems (the reformulation in terms of conformal maps will not be appropriate, for example, since the Stokes streamfunction is a biharmonic function and these are not preserved by conformal transformations), large-deflection interfaces should still be separable into distinct regions governed by different force balances, and the construction of a matching algorithm should therefore be possible even if alternate representations must be used for inner and outer profiles. While the tip corners exhibited by leading order large deflection solutions in §4.1.1 might lead one to guess that large deflection solutions in three dimensional systems forced by a point charge will have near-conical tip shapes, it is not possible to satisfy the required balance between surface tension and electrostatic pressure with such a profile.

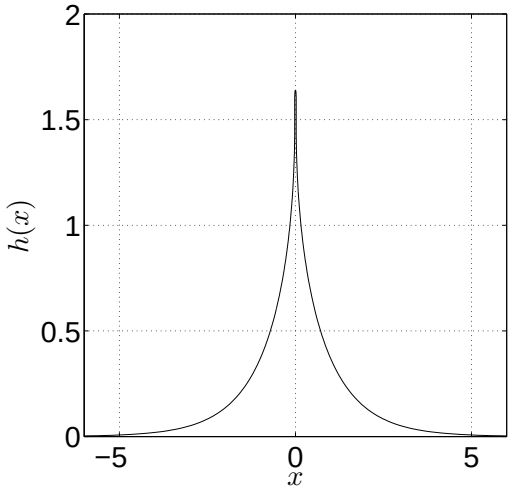

FIGURE 6.1. Computed deflection profile for $l = 2$, $M = 256$, $h(0) = 1.64$. Just before equilibrium interfaces develop folds, the deflection profile can feature a long slender column connecting a high-curvature tip to a relaxed portion of the interface similar to the outer profiles of §4.1.1.

Fluid Withdrawal

- The method applied to study the inverse problems of Chapter 5 may also be applied to two-dimensional selective withdrawal systems such as those analyzed in (Jeong & Moffatt, 1992; Jeong, 2007). The end goals remain the same: the design of withdrawal forcing that is able to produce interfaces with desired properties. This may be particularly important when related back to the use of selective withdrawal systems as particle coating methods - controlling the interface shape near transition is known to very directly influence the resulting coating properties (thickness, for example).

- The two-dimensional withdrawal flows studied in (Jeong & Moffatt, 1992) are capable of supporting 'remote' singularities - that is, the cusp that is noted to form as the capillary number of the system diverges does so at 2/3 of the height between the dipole and the undisturbed interface height. This is not a feature

observed in solutions of the inverse problem for EMS. We aim to gain a fuller understanding of the differences between the two systems that result in this dichotomy.

Appendix A
MATLAB Codes

In this appendix, we give examples of MATLAB code implementing the collocation and matching methods of §3.4 and Chapter 4.

A.1 Collocation Method of §3.4

We set $N = M$ everywhere in this code for compactness. Example call:

```
full_solutions(0.01:0.01:1,1,128);
```

```
function full_solutions(h0_vals,l,M)

% Compute initial guesses for h and q based on perturbation solutions:
C = (l^2/pi^2*quadgk(@(t)exp(-t)./(l^2+t.^2).^2,0,Inf));
q_init = sqrt(h0_vals(1)/C);
h_init = pert_solutions(q_init,l,M);

% Normalize the perturbation solution:
norm_h_init = h_init/h_init(1);

% Set the options for lsqnonlin:
options = optimset('Display','iter','TolFun',1.0e-12,'TolX',1.0e-14);

% Initialize indicator variables:
n = length(h0_vals);
j_fold = n+1;
j_cross = n+1;
j_miss = n+1;

% For each given h0 value, compute full interface deflection:
for j = 1:n
    if j == 1
        v = lsqnonlin(@(v)obj_fun(v(1),l,h0_vals(j)*[1 v(2:M)]), ...
            [q_init,norm_h_init(2:M)],[],[],options);
    else
        v = lsqnonlin(@(v)obj_fun(v(1),l,h0_vals(j)*[1 v(2:M)]), ...
```

```
            v,[],[],options);
    end
    q_vals(j) = v(1);
    h_vals(j,:) = h0_vals(j)*[1 v(2:M)];
    [resid_vals(j,:),z_vals(j,:)] = obj_fun(q_vals(j),l,h_vals(j,:));

    % Note if solution fails to be 1-1:
    if max(imag(z_vals(j,2:M)-z_vals(j,1:M-1))) > 0
        j_fold = min(j_fold,j);
    end

    % Note and break when solution first crosses vertical axis:
    if max(imag(z_vals(j,:))) > 1e-6
        j_cross = j;
        break;
    end

    % Note and break when residual is no longer small:
    if max(abs(resid_vals(j,:))) > 1e-4
        j_miss = j;
        break;
    end

    % Note and break when profile does not extend far enough to represent
    % full decay behavior:
    if abs(real(z_vals(j,M))) + abs(real(z_vals(j,M-1))) > h0_vals(j)/100
        j_miss = j;
        break;
    end
end

% Plot final physical and accurate solution:
j_final = min(j_cross,j_miss)-1;
figure(1);
plot(real(1i*z_vals(j_final,:)),imag(1i*z_vals(j_final,:)),'k-');
xlabel('$x$'); ylabel('$h(x)$');

% Plot q-h(0) bifurcation diagram:
if n > 1
    figure(2);
    plot([0,q_vals(1:j_final)],[0,h0_vals(1:j_final)],'k-');
    xlabel('$q$'); ylabel('$h(0)$');
end
```

```
function [resid,z,zp,zpp,kappa,A,Bn] = obj_fun(Q,l,h)

M = length(h);
theta = 0:pi/M:(M-1)*pi/M;

% Calculate Fourier coefficients assuming zero imaginary part at each
% image node:
Bn_temp = fft([h,0,h(end:-1:2)])./(2*M);

% Adjust Fourier coefficients to produce an analytic map:
Bn = Bn_temp.*[1,2*ones(1,M-1),1,zeros(1,M-1)];

% Set A to give the correct image charge height:
A = l-Bn(1);

% Calculate image node locations and their derivatives under the bilinear
% part of the conformal map:
z_flat = -1i.*A.*tan(theta./2);
zp_flat = -1i.*0.5.*A.*sec(theta./2).^2;
zpp_flat = -1i.*0.5.*A.*sec(theta./2).^2.*tan(theta./2);

% Calculate adjustments to image node locations and their derivatives due
% to the Fourier-like part of the conformal map:
z_fourier = (2*M).*ifft(Bn);
zp_fourier = (2*M).*ifft(1i.*[0:M,zeros(1,M-1)].*Bn);
zpp_fourier = (2*M).*ifft(-[0:M,zeros(1,M-1)].^2.*Bn);

% Calculate final image node locations and their derivatives:
z = z_flat + z_fourier(1:M);
zp = zp_flat + zp_fourier(1:M);
zpp = zpp_flat + zpp_fourier(1:M);

% Calculate and return residual pressure at each image node:
kappa = imag(zpp.*conj(zp))./(zp.*conj(zp)).^(3/2);
p_elec = Q^2./(4*pi^2*(zp.*conj(zp)));
resid = (h-kappa-p_elec);
```

```
function h = pert_solutions(q,l,M)

% Compute perturbation solution deflection at approximate image node
% locations:
theta = 0:pi/M:(M-1)*pi/M;
x = l.*tan(theta/2);
for j = 1:M
    h(j) = (q^2*l^2/(2*pi^2))*quadgk(@(xi) exp(-abs(x(j)-xi))./ ...
        (xi.^2+l^2).^2,-Inf,Inf);
end
```

A.2 Matching Method of §4.1.3

A.2.1 Outer Solution Maps

Example call:

```
outer_solutions(1,128,-0.5);
```

```
function [xi,A_out,Bn_out] = outer_solutions(l_0,M_out,t)

gamma = 0.5*pi/(pi - atan(1/(l_0*sqrt(4-l_0^2)/(2-l_0^2))));

% Set the options for lsqnonlin:
options = optimset('Display','iter','TolFun',1.0e-12,'TolX',1.0e-14);

% For the given l_0 value, compute outer deflection profile:
h_init = zeros(1,M_out);
h_vals = lsqnonlin(@(v)outer_obj_fun(l_0,v,gamma,t),h_init,[],[],options);
[~,xi,A_out,Bn_out] = outer_obj_fun(l_0,h_vals,gamma,t);

% Plot the computed profile:
figure(201);
plot(real(1i*[-fliplr(xi(2:M_out)),xi]), ...
    imag(1i*[fliplr(xi(2:M_out)),xi]),'k-');
xlabel('$x$'); ylabel('$h_0(x)$');
```

```
function [resid,xi,A_out,Bn_out] = outer_obj_fun(l_0,h,gamma,t)

M_out = length(h);
psi = 0:pi/M_out:(M_out-1)*pi/M_out;
```

```
% Calculate Fourier coefficients assuming zero imaginary part at each
% image node:
Bn_temp = fft([h,0,h(M_out:-1:2)])./(2*M_out);

% Adjust Fourier coefficients to produce an analytic map:
Bn_out = Bn_temp.*[1,2*ones(1,M_out-1),1,zeros(1,M_out-1)];

% Set A to give the correct intermediate charge height:
A_out = l_0-Bn_out(1);

% Calculate intermediate node locations under the bilinear part of the
% conformal map:
z_flat = -1i.*A_out.*tan(psi./2);

% Calculate adjustments to intermediate node locations due to the
% Fourier-like part of the conformal map:
z_fourier = (2*M_out).*ifft(Bn_out);

% Calculate final intermediate node locations:
z = z_flat + z_fourier(1:M_out);

% Apply fold map to produce final profile (tip corner):
xi = (z-h(1)).^(1/gamma)./(z-h(1)-t).^(1/gamma-1) + (h(1)-(1/gamma-1)*t);

% Calculate and return distance from exact solution at each image node:
h_exact = exact_outer(l_0,-imag(xi));
resid = real(xi) - h_exact;
```

A.2.2 Inner Solution Maps

Example call:

```
inner_solutions(-0.75,0.6,256,32);
```

```
function [Xi,Q,A_in,Bn_in,offset] = inner_solutions(T,gamma,N_in,M_in)

% Set the options for lsqnonlin:
options = optimset('Display','iter','TolFun',1.0e-12,'TolX',1.0e-14);

% initialize parameters and perform least-squares minimization:
v_init = [1,zeros(1,M_in-2),1];
```

```
v = lsqnonlin(@(v)inner_obj_fun(gamma,T,v,N_in),v_init,[],[],options);
[~,Xi,A_in,Bn_in] = inner_obj_fun(gamma,T,v,N_in);
Q = v(1);

% Compute asymptotic offset in the image plane:
offset = Bn_in(M_in+1)*A_in^(1/gamma - 1)/gamma;

% Plot the computed profile:
figure(101);
plot(real(1i*[-fliplr(Xi(2:N_in)),Xi]), ...
    imag(1i*[fliplr(Xi(2:N_in)),Xi]),'k-');
xlabel('$X$'); ylabel('$H(X)$');
```

```
function [resid,Xi,A_in,Bn_in] = inner_obj_fun(gamma,T,v,N_in)

M = length(v);
Q = v(1);

% Compute free mode amplitudes using boundary conditions:
Bn_in(3:M+1) = v(2:M);
Bn_in(1) = 0.5*(1+T)^gamma - sum(Bn_in(3:2:M-1)) - 0.5*Bn_in(M+1);
Bn_in(2) = 0.5*(1+T)^gamma - sum(Bn_in(4:2:M)) - 0.5*Bn_in(M+1);

% Set A to give the correct intermediate charge height:
l_inter = (2+T)^gamma;
A_in = l_inter - Bn_in(1) - Bn_in(M+1)/2^(1/gamma-1);

% Define node locations in the preimage plane:
theta = 2*pi*(0:N_in-1)/(2*N_in);

% Calculate intermediate node locations and their derivatives under the
% bilinear part of the conformal map:
z_flat = -1i.*A_in.*tan(theta./2);
zp_flat = -1i.*0.5.*A_in.*sec(theta./2).^2;
zpp_flat = -1i.*0.5.*A_in.*sec(theta./2).^2.*tan(theta./2);

% Calculate adjustments to intermediate node locations and their
% derivatives due to the Fourier-like part of the conformal map:
Bn_padded = [Bn_in(1:M),zeros(1,(2*N_in)-M)];
z_fourier = (2*N_in).*ifft(Bn_padded);
zp_fourier = (2*N_in).*ifft(1i.*[0:M-1,zeros(1,(2*N_in)-M)].*Bn_padded);
zpp_fourier = (2*N_in).*ifft(-[0:M-1,zeros(1,(2*N_in)-M)].^2.*Bn_padded);

% Calculate adjustments to intermediate node locations and their
```

```
% derivatives due to the singular part of the conformal map:
z_sing = Bn_in(M+1)*((1+exp(1i*theta))/2).^(1/gamma-1);
zp_sing = (1/gamma-1)*(1i - tan(theta/2)).*z_sing/2;
zpp_sing = -z_sing.*(((1/gamma-1)-(1/gamma-1)^2)*sec(theta/2).^2 + ...
    2*(1/gamma-1)^2*(1+1i*tan(theta/2)))/4;

% Calculate final intermediate node locations and their derivatives:
z = z_sing + z_fourier(1:N_in) + z_flat;
zp = zp_sing + zp_fourier(1:N_in) + zp_flat;
zpp = zpp_sing + zpp_fourier(1:N_in) + zpp_flat;

% Apply fold map to produce final profile (asymptotically angled):
Xi = z.^(1/gamma);
Xip = z.^(1/gamma-1).*zp/gamma;
Xipp = z.^(1/gamma-1).*zpp/gamma + ...
    (1-gamma)*z.^(1/gamma-2).*(zp.^2)/(gamma^2);

% Calculate and return residual pressure at each image node:
kappa = imag(Xipp.*conj(Xip))./(Xip.*conj(Xip)).^(3/2);
p_elec = Q^2./(4*pi^2*(Xip.*conj(Xip)));
resid = (-kappa -p_elec);
```

A.2.3 Matched Solutions

Example call:

```
matched_solutions(0.1,1,32,256,128,-0.5,-0.75);
```

N_{in} controls the number of points representing the final matched solution, and can be increased without significant computational expense to obtain finer resolutions of both the inner and outer profile portions. This code relies on the inner and outer solution codes of the previous subsections.

```
function [l_1,q_1] = matched_solutions(ep,l_0,M_in,N_in,M_out,T,t)

gamma = 0.5*pi/(pi - atan(1/(l_0*sqrt(4-l_0^2)/(2-l_0^2))));

% Compute normalized inner solution and charge strength Q:
[xi,Q,A_in,Bn_in] = inner_solutions(T,gamma,N_in,M_in);
```

```
% Scale inner profile by epsilon and subtract the overlap function:
theta = 2*pi*(0:N_in-1)/(2*N_in);
zeta_in_sub = ep*( xi - ...
    exp(-1i*pi/(2*gamma))*(A_in*tan(theta./2)).^(1/gamma) - ...
    Bn_in(M_in+1)*A_in^(1/gamma - 1)/gamma );

% Compute charge location l_1 for the matched solution:
dl = ep*((2+T) - Bn_in(M_in+1)*A_in^(1/gamma - 1)/gamma);
l_1 = l_0 + dl;

% Compute charge strength q_1 for the matched solution:
q_1 = sqrt(ep)*Q;

% Compute outer solution parameters:
[~,A_out,Bn_out] = outer_solutions(l_0,M_out,t);

% Compute matched solution profile at images of inner solution nodes:
zeta_out = matching(ep,l_0,N_in,M_out,t,gamma,A_in,A_out,Bn_out);
zeta_match = zeta_in_sub + zeta_out;

% Plot the computed profile:
figure(301);
plot(real(1i*[-fliplr(zeta_match(2:N_in)),zeta_match]), ...
    imag(1i*[fliplr(zeta_match(2:N_in)),zeta_match]),'k-');
xlabel('$x$'); ylabel('$h_1(x)$');
```

```
function zeta_out = matching(ep,l_0,N_in,M_out,t,gamma,A_in,A_out,Bn_out)

% Extract non-zero outer solution Fourier coefficients:
Bn_out = Bn_out(1:M_out+1);

% Compute the automorphism parameter beta:
beta = (A_in/A_out)*((-t)^(1-gamma)/ ...
    (1-(2/A_out)*real(sum((0:length(Bn_out)-1).*Bn_out))))*ep^gamma;

% Compute locations of evenly spaced inner solution nodes under the
% appropriate automorphism (locations now expressed with respect to the
% outer region angle psi):
theta = 0:pi/N_in:pi*(1-1/N_in);
psi = 2.*atan(beta*tan(theta./2));

% Compute outer profile at each mapped node:
for j = 1:N_in
    z_out(j) = A_out*((1-exp(1i*psi(j)))./(1+exp(1i*psi(j)))) + ...
```

```
        sum(Bn_out.*exp(1i*psi(j)).^(0:M_out));
    zeta_out(j) = (z_out(j)-sum(Bn_out)).^(1/gamma)./ ...
        (z_out(j)-sum(Bn_out)-t).^(1/gamma-1) + l_0;
end
```

References

Acrivos, A., & Lo, T. S. (1978). Deformation and breakup of a single slender drop in an extensional flow. *J. Fluid Mech.*, *86*(04), 641–672.

Berkenbusch, M. K., Cohen, I., & Zhang, W. W. (2008). Liquid interfaces in viscous straining flows: numerical studies of the selective withdrawal transition. *J. Fluid Mech.*, *613*, 171–203.

Bernstein, D., Guidotti, P., & Pelesko, J. A. (2000). Mathematical analysis of an electrostatically actuated mems devices. In *Proceedings of Modeling and Simulation of Microsystems (MSM)*, (pp. 489–492).

Blanchette, F., & Zhang, W. W. (2009). Force balance at the transition from selective withdrawal to viscous entrainment. *Phys. Rev. Lett.*, *102*, 144501.

Blanchette, F., & Zhang, W. W. (2010). Blanchette and zhang reply:. *Phys. Rev. Lett.*, *105*, 089402.

Brubaker, N. D., & Lindsay, A. E. (2013). The onset of multi-valued solutions of a prescribed mean curvature equation with singular non-linearity. *European Journal of Applied Mathematics*, *FirstView*, 1–26.

Brubaker, N. D., & Pelesko, J. A. (2011). Non-linear effects on canonical mems models. *European Journal of Applied Mathematics*, *22*, 455–470.

Brubaker, N. D., & Pelesko, J. A. (2012). Analysis of a one-dimensional prescribed mean curvature equation with singular nonlinearity. *Nonlinear Analysis: Theory, Methods & Applications*, *75*(13), 5086–5102.

Brubaker, N. D., Siddique, J. I., Sabo, E., Deaton, R., & Pelesko, J. A. (2013). Refinements to the study of electrostatic deflections: theory and experiment. *European Journal of Applied Mathematics*, *24*, 343–370.

Buckmaster, J. D. (1972). Pointed bubbles in slow viscous flow. *J. Fluid Mech.*, *55*(03), 385–400.

Chuang, W.-C., Lee, H.-L., Chang, P.-Z., & Hu, Y.-C. (2010). Review on the modeling of electrostatic mems. *Sensors*, *10*(6), 6149–6171.

Cohen, I., Li, H., Hougland, J. L., Mrksich, M., & Nagel, S. R. (2001). Using selective withdrawal to coat microparticles. *Science*, *292*(5515), 265–267.

du Pont, S. C., & Eggers, J. (2006). Sink flow deforms the interface between a viscous liquid and air into a tip singularity. *Phys. Rev. Lett.*, *96*, 034501.

Eggers, J. (2001). Air entrainment through free-surface cusps. *Phys. Rev. Lett.*, *86*, 4290–4293.

Eggers, J., & Courrech du Pont, S. (2010). Comment on "force balance at the transition from selective withdrawal to viscous entrainment". *Phys. Rev. Lett.*, *105*, 089401.

Eggers, J., & du Pont, S. C. (2009). Numerical analysis of tips in viscous flow. *Phys. Rev. E*, *79*, 066311.

Evans, L. C. (1998). *Partial Differential Equations*. American Mathematical Society.

Hinch, E. J. (1980). The evolution of slender inviscid drops in an axisymmetric straining flow. *Journal of Fluid Mechanics*, *101*, 545–553.

Hocking, G., & Forbes, L. (2004). The lens of freshwater in a tropical island - 2d withdrawal. *Computers and Fluids*, *33*(1), 19–30.

Jeong, J.-T. (2007). Free surface deformation due to a source or a sink in stokes flow. *European Journal of Mechanics - B/Fluids*, *26*(6), 720–728.

Jeong, J.-T., & Moffatt, H. K. (1992). Free-surface cusps associated with flow at low reynolds number. *J. Fluid Mech.*, *241*, 1–22.

Lister, J. R. (1989). Selective withdrawal from a viscous two-layer system. *Journal of Fluid Mechanics*, *198*, 231–254.

MATLAB (2012). *version 8.0.0 (R2012b)*. Natick, Massachusetts: The MathWorks Inc.

Moffatt, H. K. (1992). Fluid mechanics, topology, cusp singularities, and related matters. In *Seminaire International de LInstitut de Mécanique de Grenoble*.

Pelesko, J. A. (2001). Multiple solutions in electrostatic mems. In *Proceedings of Modeling and Simulation of Microsystems (MSM)*, (pp. 290–293).

Pelesko, J. A. (2002). Mathematical modeling of electrostatic mems with tailored dielectric properties. *SIAM J. Appl. Math.*, *62*(3), 888–908.

Pelesko, J. A., & Chen, X. Y. (2003). Electrostatic deflections of circular elastic membranes. *J. Electrostatics*, *57*(1), 1–12.

Pelesko, J. A., & Triolo, A. A. (2000). Nonlocal problems in mems device control. In *Proceedings of Modeling and Simulation of Microsystems (MSM)*, (pp. 509–512).

Porter, R. M. (2005). History and recent developments in techniques for numerical conformal mapping.

Rallison, J. M. (1984). The deformation of small viscous drops and bubbles in shear flows. *Ann. Rev. Fluid Mech.*, *16*(1), 45–66.

Richardson, S. (1968). Two-dimensional bubbles in slow viscous flows. *J. Fluid Mech.*, *33*(03), 475–493.

Richardson, S. (1973). Two-dimensional bubbles in slow viscous flows. part 2. *J. Fluid Mech.*, *58*(01), 115–127.

Siddique, J. I., Deaton, R., Sabo, E., & Pelesko, J. A. (2011). An experimental investigation of the theory of electrostatic deflections. *Journal of Electrostatics*, *69*(1), 1–6.

Stein, E. M., & Shakarchi, R. (2003). *Complex Analysis*. Princeton University Press.

Taylor, G. I. (1934). The formation of emulsions in definable fields of flow. *P. Roy. Soc. Lond. A*, *146*(858), 501–523.

Taylor, G. I. (1968). The coalescence of closely spaced drops when they are at different electric potentials. *P. Roy. Soc. Lond. A*, *306*(1487), pp. 423–434.

Wegmann, R. (2005). Methods for numerical conformal mapping. In R. Kuhnau (Ed.) *Handbook Of Complex Analysis: Geometric Function Theory*, vol. 2. North Holland.

Wilkening, J. (2011). Breakdown of self-similarity at the crests of large-amplitude standing water waves. *Phys. Rev. Lett.*, *107*, 184501.

Younes, N. A., Nothias, J. M., & Garfinkel, M. R. (2008). Islet transplantation: the quest for an ideal source. *Ann. Saudi Med.*, *28*, 325–333.

Youngren, G. K., & Acrivos, A. (1976). On the shape of a gas bubble in a viscous extensional flow. *J. Fluid Mech.*, *76*(03), 433–442.

Zhang, W. W. (2004). Viscous entrainment from a nozzle: Singular liquid spouts. *Phys. Rev. Lett.*, *93*, 184502.